

MEMS aptamer sensors for detecting plant chemicals

by

Silu Feng

A dissertation submitted to the graduate faculty

in partial fulfillment of the requirements for the degree of

DOCTOR OF PHILOSOPHY

Major: Electrical Engineering (Bioengineering)

Program of Study Committee:

Long Que, Major Professor

Liang Dong

Justin Walley

Santosh Pandey

Jiming Song

The student author, whose presentation of the scholarship herein was approved by the program of study committee, is solely responsible for the content of this dissertation. The Graduate College will ensure this dissertation is globally accessible and will not permit alterations after a degree is conferred.

Iowa State University

Ames, Iowa

2020

Copyright © Silu Feng, 2020. All rights reserved.

TABLE OF CONTENTS

	Page
LIST OF FIGURES	v
LIST OF TABLES	ix
ACKNOWLEDGEMENTS	x
ABSTRACT	xi
CHAPTER 1. INTRODUCTION TO ANODIC ALUMINUM OXIDE	1
1.1 Overview of Anodic aluminum oxide	1
1.2 Fabrication, structure and properties of nanoporous AAO	2
1.3 AAO Formation mechanisms	7
1.4 Surface chemistry and functionalization of AAO	9
1.5 Properties of AAO for optical sensing	11
1.5.1 Surface-Enhanced Raman Scattering (SERS)	11
1.5.2 Surface Plasmon Resonance (SPR)	12
1.5.3 Reflectometric Interference Spectroscopy (RIFS)	13
1.6 Simulation for sensor surface functionalization	14
1.7 Microfluidics capillary interface	15
References	17
Figures and Tables	24
CHAPTER 2. AN APTAMER NANOPORE-ENABLED MICROSENSOR FOR DETECTION OF THEOPHYLLINE	34
Abstract	34
2.1 Introduction	35
2.2 Materials and methods	37
2.2.1 Fabrication of the nanopore thin film-based sensor	37
2.2.2 Chemicals and materials	38
2.2.3 Preparation of plant extract	39
2.2.4 Surface functionalization and biodetection procedure	40
2.2.5 Instrumentation	40
2.2.6 Experimental data acquisition	41
2.2.7 Detection procedure	41
2.3. Results and discussion	42
2.3.1 Detection of theophylline in buffer solution & evaluation of the binding kinetics between aptamer and theophylline	42
2.3.2 Assessment of influence of RNase inhibitor on the assay	45
2.3.3 Determination of sensor regeneration rate/capability	46
2.3.4 Detection of theophylline in caffeine and theobromine	47
2.3.5 Detection of theophylline in plant extracts and serum samples	48

2.4. Conclusions	50
References	51
Figures	54
 CHAPTER 3. DEVELOPMENT OF A STRUCTURE-SWITCHING APTAMER- BASED NANOSENSOR FOR SALICYLIC ACID DETECTION	58
Abstract	58
3.1 Introduction	59
3.2 Materials and methods	62
3.2.1 Chemicals and materials	62
3.2.2 Structure-switching SELEX.....	62
3.2.3 Fabrication of the nanopore thin film-based sensor.....	64
3.2.4 Surface functionalization	65
3.2.5 Detection procedure	66
3.2.6 SA extraction from plants	66
3.2.7 Data acquisition and statistical analysis.....	67
3.2.8 Circular dichroism spectroscopy.....	67
3.2.9 HPLC analysis	68
3.2.10 GC-MS analysis	68
3.3 Results and discussion.....	69
3.3.1 Structure-switching SELEX.....	69
3.3.2 Determine of binding affinity of SAaptal to SA	70
3.3.3 Evaluation of binding kinetics of SAaptal	71
3.3.4 Test of binding sensitivity, specificity, and inter-day variation of SAaptal	71
3.3.5 Detection of SA in plant extracts	74
3.4 Conclusion.....	75
References	76
Figures and tables.....	81
 CHAPTER 4. OPTICAL APTAMER-BASED SENSING CHIP FOR DETECTING PLANT HORMONES.....	90
Abstract	90
4.1. Introduction	91
4.2. Materials and Methods	93
4.2.1. Chemicals and materials	93
4.2.2 Description and operational principle of the chip	94
4.2.3 Fabrication process of the chip	96
4.2.4 Surface functionalization	97
4.2.5 Instrumentation	97
4.2.6 Detection procedure	98
4.2.6 ABA and SA extraction from plant leaves	99
4.2.7 Data acquisition and statistical analysis.....	100
4.3. Results and Discussion.....	100
4.3.1 Fabricated chip and its function demonstration	100
4.3.2 Detection of hormones in buffer	101

4.3.3 Regeneration of aptamer sensors	102
4.3.4 Detection of hormones in plant extracts	104
4.4. Conclusions	105
References	106
Figures	109
CHAPTER 5. CONCLUSIONS AND FUTURE WORK	115
5.1 Conclusion.....	115
5.2 Future works.....	116
References	116

LIST OF FIGURES

Figure 1. 1 Anodic aluminum oxide (AAO) structure. Pore structure in AAO and definition of the main structural parameters	24
Figure 1. 2 Experimental equipment used to produce anodized aluminum oxide (Gerrard Eddy Jai Poinern., 2011)	24
Figure 1. 3 Schematic of the major features involved in the formation of the barrier layer.....	25
Figure 1. 4 Schematic of the pore formation mechanism in an acidic electrolyte (Poinern GEJ., 2011).....	25
Figure 1. 5 Schematic of ion movement during pore formation (Poinern GEJ., 2011)	26
Figure 1. 6 Surface functionalization process	26
Figure 1. 7 AAO-based system. (a) Fabrication process based on gold nanoparticles. (b) SEM image of the SERS systems and sensing performance.....	27
Figure 1. 8 AAO-based SPR systems. (a) Structure of a LSPR system based on AAO coated with gold and chemically functionalized with antibodies to target C-reactive protein antigens. (b) Sensing performance of that system when detecting C-reactive protein	28
Figure 1. 9 Schematic diagram of a reflectometric interference spectroscopy anodic aluminum oxide (RIFS-AAO) set-up for biosensing applications.....	28
Figure 1. 10 Sensing principle of a AAO-RIFS system and real-time monitoring of antibody-antigen interactions	29
Figure 1. 11 (a) SEM image for AAO; (b) Schematic for simulation; (c) Simulation result for AAO fringes	29
Figure 1. 12 (a) Schematic for surface functionalization; (b) Result for simulation after surface functionalization.....	30
Figure 1. 13 (a) SEM image for non-uniform nanopores; (b) Optical signals due to different concentrations; (c) Measured shift of optical signals.....	31
Figure 2. 1 (a) Sketch showing a nanopore-based aptamer sensor and its operational principle; (b) process flow to fabricate the nanopore-based sensors; (c) a photo of a chip consisting of 15 AAO nanopore-based sensors with a microfluidic interface; (d) SEM image	54

Figure 2. 2 (a) Illustration of surface functionalization process of the sensor; (b) the setup for the optical measurements; (c) representative measured optical signals for theophylline at different concentration.....	55
Figure 2. 3 (a) Measured shift of optical signals of theophylline under a series of concentrations using SENSOR1 and SENSOR2; (b) measured binding kinetics of theophylline with aptamer at a concentration of 40 μ M.....	56
Figure 2. 4 (a) Comparison of transducing signals from the sensors with applied inhibitor, after washing the inhibitor, and without applied inhibitor in the assay; (b) the difference of the transducing signals between the fresh sensors and the regenerated sensors;.....	56
Figure 3. 1 (a) Pipeline of structure-switching SELEX; (b) Design of HiSeq-compatible SELEX library. The library sequence is highlighted by the red frame. P5 and P7 sequences are compatible with HiSeq. Read SP is the primer sequence for reading the 40 random nucleotides (“X” in the diagram). Index SP is the primer sequence for reading the 6-nucleotide index (“N” in the diagram). (For interpretation of the references to color in this figure legend, the reader is referred to the Web version of this article.).....	81
Figure 3. 2 (a) Relative frequency of the top five aptamer candidates over the 6th, 13th and 15th SELEX cycles; (b) Optical signal shift of the top five aptamer candidates using 40 μ M SA or 4-HBA. Mean \pm SEM was shown (n=6).	82
Figure 3. 3 Saturation curve of SAapta1 with SA and 4-HBA; Mean \pm SEM was shown (n=9)	83
Figure 3. 4 Binding kinetics of SAapta1 with 0.2 μ M and 40 μ M SA. Mean \pm SEM was shown (n=6)	83
Figure 3. 5 (a) Optical signal shift induced by a series concentration of SA, MeSA, SAG, BA and buffer only; Mean \pm SEM was shown (n=9); (b) SA metabolites and their structures; (c) The circular dichroism spectra of 1 μ M SAapta1 in the SELEX binding buffer with buffer, 40 μ M SA, 4-HBA, MeSA, SAG and BA. Mean \pm SEM was shown (n=3). SEM was shown as light-colored area fill; (d) Optical signal shift of the same SA sample (40 μ M) measured at three different days. Mean \pm SEM was shown (n=9). No statistically significant changes were detected using one-way ANOVA.....	84
Figure 3. 6 (a) Optical signal shift of spike-in SA with and without Arabidopsis extracts. (b) Comparison between nanoFPI and HPLC using rice	

extracts. (c) Negligible detection of MeSA in rice extracts using GC-MS.	85
Figure S3. 1 Sketch of optical setup for the measurement and operational principle of the nanoFPI sensor and fabrication process flow.	86
Figure S3. 2 Surface chemical functionalization of the nanoFPI sensor.....	87
Figure 4. 1 (a) Schematic of the chip; (b) Close-up showing the SU8 microstructures of the capillary micropump in the upper stream; (c) Close-up showing the microstructures of the capillary micropump; (d) Optical sensor operational principle.....	109
Figure 4. 2 (a) Photo of a fabricated chip bonded with PDMS slabs; SEM images of (b) the SU8 microstructures for capillary microfluidics; (c) the SU8 microfluidic passive valves, and (d) the nanopores on the nanoFPI sensors fabricated from anodic aluminum oxide	110
Figure 4. 3 Demonstration of functions of the capillary microfluidics: (top) sketch of the chip; (a)-(b) food dye flows through the SU8 microstructures-enabled micropump due the capillary force from inputs 1, 2, 3; (c) food dye reaches the sensor region; (d) food dye reaches the capillary passive-stop valves; (e)-(f) water is flowed through the SU8 microstructures-enabled micropump to the passive-stop valves through input 4, the food dye is drained out of the sensor region; (g) food dye is washed out of the chip.....	111
Figure 4. 4 Measured optical signals of five plant hormones in SELEX buffer: (a) optical interference fringes of ABA-sensors with different concentrations of ABA; (b) the optical signal shift for five plant hormones measured by ABA-sensors; (c) optical interference fringes of SA-sensors with different concentrations of SA; (d) the optical signal shift for five plant hormones measured by SA-sensors;.....	112
Figure 4. 5 Measured optical signals of ABA and SA in SELEX buffer on the regenerated sensor: (a) Measured optical signals of ABA in SELEX buffer on the same regenerated ABA-sensor and of the regenerated sensor after being rinsed by PBS buffer for each ABA concentration; (b) Measured optical signals of SA in SELEX buffer on the same regenerated SA-sensors and measured optical signals of the regenerated sensor after being rinsed by PBS buffer for each SA concentration; (c) Measured optical signals of ABA in SELEX buffer on the same ABA-sensor regenerated three times for each concentration; (d) Measured	

optical signals of SA in SELEX buffer on the same SA-sensor regenerated three times for each concentration.....	113
--	-----

Figure 4. 6 Measured optical signals of five hormones spiked in plant extracts from (a) ABA-sensors and (b) SA-sensors on chip	114
---	-----

LIST OF TABLES

Table 1. 1 Major acid components of typical electrolyte types used to produce porous oxide layer on an aluminum substrate (Poinern GEJ., 2011).....	31
Table 1. 2 Voltage and times of three commonly used electrolytes for the production of porous oxide layer on an aluminum substrate	32
Table 1. 3 Summary of optical biosensors based on AAO (also called NAA) platforms	33
Table 3. 1 Library, capture probes, and primers.....	88
Table 3. 2 SA aptamer candidates	89

ACKNOWLEDGEMENTS

I would first like to express my sincere gratitude to my advisor, Dr. Long Que, for his patience, motivation, enthusiasm, and immense knowledge. Dr. Long Que not only provide financial support for me during my Ph.D program, but also offered continuous and insightful suggestions regarding both my research projects and my life. It has been my great honor to work with him. This dissertation could not have been completed without his encouragement and constant guidance.

Second, I would like to thank the other members of my advisory committee: Dr Liang Dong, Dr Santosh Pandey, Dr. Jiming Song, Dr. Walley Justin W, for their extremely helpful comments on my research. Also, thanks to Dr. Wei wang for helping with the plant chemicals.

I would also like to thank my fellow labmates: Renyuan Yang, Xiaoke Ding, Subin Mao, Chao Song, Xiangchen Che, andChangtian Chen for their valuable research experience and great support.

I also would like to thank MRC staff members Dr. Wai Y.Leung and Noack Max for their technical and experimental support.

Finally, I would like to dedicate this thesis to my parents Bangmin Feng and Lanying Wang for their unconditional love and financial support. I also would like to thank my best friends Yiyi Sun, Xiong Deng, Lin Kong, Kaijian Zhu for their love, understanding and endless encouragement throughout my life.

ABSTRACT

In this dissertation, the underlying mechanisms of AAO optical sensor simulation and application are described. AAO based optical biosensors were developed for testing theophylline, silicic acid, and a multiplexed device for detecting multiple plant chemical solutions was designed.

Chapter 1 introduces background information about anodic aluminum oxide (AAO), including a basic introduction to the history of AAO development, AAO fabrication, structures, and properties. It also explains the self-ordered nanopore formation mechanism, the optical principles of using Rsoft simulation, and surface functionalization for AAO. Finally, the chapter describes emerging applications in biosensing, bio-detection, and biocompatible interfaces.

Chapter 2 introduces AAO as an aptamer-based nanopore thin film sensor for detecting theophylline in a buffer solution and in complex fluids, including plant extracts and serum samples. Experiments revealed that an aptamer-based sensor has good specificity, selectivity, and reasonable reusability with a significantly improved dynamic-detection range. Its low cost and ease of operation make this type of sensor suitable for point-of-care application to monitoring the theophylline level of patients in real time.

Chapter 3 introduces a structure-switching aptamer-based nanopore thin-film sensor developed for cost-effective, rapid, sensitive and simple detection of SA in both buffer and plant extracts. A high-affinity SA aptamer was identified by immobilizing the SELEX library rather than SA and screening the library using a structure-switching SELEX approach. This nanosensor also exhibited good selectivity among SA and its common metabolites.

Chapter 4 introduces a chip equipped with aptamer-based sensors interfaced with a capillary microfluidic unit suitable for screening and detecting hormones in plant samples. The chip allows samples to be automatically delivered to on-chip sensors without using external pumps, making it suitable for operation in the field or in source-limited settings. Since arrayed sensors can be functionalized with different aptamers specific to different plant hormones, this chip can screen and identify the hormones in unknown samples.

CHAPTER 1. INTRODUCTION TO ANODIC ALUMINUM OXIDE

1.1 Overview of Anodic aluminum oxide

Al makes up about 8% of the Earth's crust, where it is the third most abundant element and the most abundant metal. However, because of its reactivity with naturally occurring oxygen in the atmosphere, Sir Humphrey Davy, physicist Hans Christian Oersted, and Karl Bayer were able to refine and improve the manufacturing of alumina from bauxite ore. Today, Alumina (Al_2O_3) is widely used in many applications and Al has become the most produced non-ferrous metal (US Geological Survey, 2011).

In the mid 1920s, anodization using Al in chromic acid was developed (HM Wire International Inc., 2010). There are two types of anodic Al oxide anodization processes. The first is a non-porous barrier layer, while the second, a thicker porous oxide structure, is called anodic an aluminum oxide (AAO) layer. The porous nature of anodic alumina films was discovered by S. Setch and A. Miyata in 1932 (Akira Miyata and Shoji Setoh., 1932) and further characterized by F. Keller's group in 1953 (F.Keller., 1953) and J. P. O'Sullivan's group in 1970 (J.P.O'Sullivan., 1970). In 1974, the Boeing Company used chromic acid, sulfuric acid, or phosphoric acid in producing anodic aluminum oxide (AAO) membranes (A.Smith, 1974). Because of AAO's uniform nanostructure, AAO began to attract interest in the area of nanotechnology during the late 1980s. In the mid-1990s, AAO was used for bottom-up templated

nanofabrication (Masuda, H., 1995; Masuda, H., 1996). In the years after 2000, AAO has become more popular in both research and industrial fields such as biosensing, bio-detection, drug delivery, etc. (La Flamme KE., 2007; Vlassiounk I., 2004; Takmakov p., 2006; Yang Z., 2007; Alvarez SD., 2009; Pan S., 2003; Wang M., 2011;).

1.2 Fabrication, structure and properties of nanoporous AAO

Self-ordered AAO can be described as having a nanoporous alumina (Al_2O_3) matrix with close-packed arrays of hexagonally-arranged cells, each containing a cylindrical central pore that grows perpendicular to the surface of the underlying aluminum substrate (A.Eftekhari., 2008).

The AAO pore structure can be defined by several structural parameters. First, pore density denotes how many pores exist per cm^2 , and porosity is the percentage occupancy of pores over an AAO surface, normally ranging from 5% to 50%. Pore diameter (d_p) usually lies between 10nm and 400nm. Interpore distance (d_{int}) is the distance between the middle points of two neighboring nanopore walls (50nm – 600nm). The pore length (L_p) is also the thickness of the AAO layer (τ_{obl}) that typically ranges from 10nm to 150nm. Fig.1.1 shows a typical AAO structure (top and cross-section) (Abel Santos, et al., 2013).

The advantages of using porous alumina as a template is that the AAO fabrication process is based on facile and inexpensive electrochemical anodization. The applicable equation simply describes an Al substrate used with a particular acid to achieve nanopores.

Al + acid + voltage = nanopores

The nanopore fabrication process can be performed using general laboratory equipment (Fig.1.2) (Gerrard Eddy Jai Poinern., 2011). First, a dual-wall tank is prepared as a container for the acid used in the anodization process. A cooling system is connected to the RF machine for cooling water to a temperature of 2°C - 8°C, after which an acid solution working as an electrolyte is poured into the tank. Most researchers tend to use oxalic, phosphoric and sulfuric acid, etc. Two working electrodes are needed during the anodization process: aluminum as the anode and platinum as the cathode. A rectifier is used to apply a DC voltage across the two electrodes, and AL is gradually anodized to form a nanoporous structure. As shown in the figure, a stirring bar and magnetic stirrer at the tank bottom are used to ensure uniformity of the acid concentration and result in smooth and stable anodization process.

Al substrate quality and surface treatment can have a significant impact on self-ordering of the pore structure during the anodization process. Also, alloying elements in the Al substrate would reduce the speed of formation of the oxide layer and influence the structure of the oxide layer during the anodization process. The standard pre-treatment of an Al strip is: first, using acetone or a similar solvent to degrease the strip. Then immerse Al in 3M NaOH for 5mins to perform electrochemical polishing. Finally, wash with milli-Q water. To prevent oxidation, this

process should always be performed in an inert atmosphere such as nitrogen or argon (Jenny, A., 1959; Hoar, T.P., 1959; Hoar, T.P., 1963; Houghton, P.S., 1960).

All AAO parameters can be precisely adjusted by controlling the anodization process. A variety of acids can be used in the anodization process to form different sizes of nanopore diameter, and some experiments have used a combination of acids. Table 1.1 shows the major acid components used to produce AAO. During the anodization process, most experiments have been conducted under potentiation conditions of high voltage and low currents, and various studies have described use of different acid researchers and different applied voltages. Table 1.2 shows voltage settings and times used in the manufacture of nano-porous oxide layer (Poinern GEJ., 2011).

Here is how we fabricated micropattern AAO. Glass substrates were purchased from Nanocs, Inc. The sheet resistance of the ITO on the glass is 100 X/sq. The photoresist AZ 1512 and AZ developer were purchased from AZ Electronic Materials plc. The following fluorescent dyes are purchased and used in the experiments: Rhodamine 6G (R6G) (Lightning Powder, Inc.), fluorescein sodium salt (FSS) (Sigma, Inc.), fluorescein isothiocyanate (FITC) (Sigma, Inc.) and fluorescent brightening agents (FBA) (Sigma, Inc.). The glass substrate is washed thoroughly in four steps: by DI water, followed by Acetone, IPA, and DI water in sequence. After a 5-minute baking of the cleaned glass substrate, a 2 μm thick aluminum layer is deposited by E-beam

evaporation. To achieve successful anodization the quality of the deposited Al is critical. One essential requirement is that the Al should be totally oxide-free, meaning during E-beam evaporation any oxidation of Al must be avoided or, as found in our experiments, the as-deposited Al cannot be anodized. The other important requirement is the surface smoothness of the deposited Al. Measurements have a typical roughness in the range of 6–12 nm (X.Li et al., 2012; X.Li et al., 2013; X.Li et al., 2013), smooth enough for carrying out anodization, and not requiring further surface polishing. This is a significant advantage over carrying out anodization on a commercial Al foil sheet, which usually requires several surface polishing steps to polish the surface of the Al sheet and ensure a sufficiently smooth surface (Y.He et al., 2012). Then we carry out anodization process (either one-step or two-step) in acid solution (0.3 M oxalic acid) with 45 V DC voltage at 2 C to form AAO on the glass substrate. In this step, a layer of AAO is formed over the whole substrate surface. Specifically, for the one-step anodization process to form AAO (G.Sulka et al., 2002), we only carry out one-step anodization on the samples for 25, 35, and 45 min, respectively. In contrast, the two-step anodization process to form AAO (Y.He et al., 2012) takes 10 min for step-one anodization in 0.3 M oxalic acid, followed by etching using a mixture of phosphoric acid (0.4 M) and chromic acid (0.2 M) at 65 C for 30 min, followed by a 40-minute step-two anodization in 0.3 M oxalic acid with the same experimental conditions as for step-one anodization. The wafer is then vigorously rinsed in DI water, and a 150 nm thick

aluminum layer is deposited on the AAO surface by thermal evaporation. Photolithography is then performed on the Al-coated AAO substrate. Specifically, a 1 μm photoresist (AZ 1512) layer is spin-coated at 4000 rpm on the substrate, then the coated substrate is soft baked for 50 s at 95 °C. The micropatterns are then transferred and generated on the photoresist through a photomask using a 416 nm light exposure with a dose of 70 mJ/cm², followed by a post-exposure bake for 50s at 105 °C. The exposed photoresist is developed and selectively removed by immersing in AZ developer for 25 s. The patterned AZ resist serves as a mask to protect the Al underneath. The patterns are then transferred to the Al layer by etching the unprotected Al area in an etching solution {(H₃PO₄:CH₃-COOH:HNO₃:H₂O) 80:5:5:10 by weight%} for 35s. During this step, care must be taken to avoid any over etching of the Al since the patterned Al layer serves as the mask for etching the AAO. The substrate is then immersed in a mixture of phosphoric acid (0.4 M) and chromic acid (0.2 M) at 20 C for 100 min to etch away the unprotected AAO and transfer the patterns into the AAO layer. Thereafter, the remaining photoresist is washed away by dipping the substrate in acetone, followed by removing the Al layer using the Al etching solution. As a result, AAO micropatterns on the substrate are obtained. Again, to obtain AAO micropatterns with high fidelity, the steps for etching Al and AAO are critical, and the etching time should be optimized. Otherwise, the resulting AAO micropatterns might be either over-etched or under-etched. In addition, Al is chosen as the mask for the AAO

layer instead of the photoresist as described earlier since the thickness of AAO is $12.5\ \mu\text{m}$ (E.Hourdakis et al., 2010; E.Hourdakis et al., 2012; A.Li et al., 1999; H.Zhou et al., 2011). It has been found that in most cases the photoresist cannot serve as a robust mask due to the long etching time (100 min) of the AAO layer. As a result, the micropatterns cannot be properly transferred directly from the photoresist to the AAO layer.

1.3 AAO Formation mechanisms

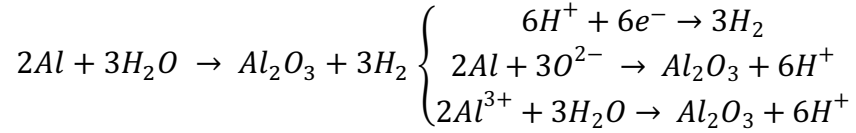
The first detailed AAO mechanisms were investigated by Keller, et al., who explained the porous oxide layer formation and pore nucleation (Keller, et al., 1953). AAO consists of two layers, the first is the barrier layer and the second is the nano-porous oxide layer.

The barrier layer, a thin and non-porous layer whose formation mechanism consists of two stages (Fig.1.3). First, after an Al substrate is placed into the fabrication equipment, the voltage is increases linearly with time while the current density is maintained to keep the electric field strength constant across the barrier layer. During this stage, the barrier layer increases until the formation voltage is reached, after which the formation mechanism moves to a second stage. In this stage, the formation voltage is maintained while the barrier layer continues to grow through migration of Al^{3+} ions from substrate to electrolyte and inward motion of O^{2-} and OH^- ions. The reaction between Al^{3+} , O^{2-} , and OH^- will form the Al_2O_3 (barrier layer). As barrier-layer thickness increases, the electrical resistance also increases, and if the voltage is maintained

constant, current flow decreases with time. At the end of this stage, the barrier layer is fully formed and remains constant (Thompson, G.E., 1997).

The nanoporous oxide layer consists of a thin nonporous oxide layer that continually regenerates at the base of the pore while the pore wall increases in height with time as it is being created. During the fabrication process, the pore size and the distance between pores are functions of the acid concentration, the anodic voltage, and the bath temperature. Usually researchers use sulfuric, phosphoric or oxalic, etc., electrolytes with pH less than 5 to produce the oxide layer. The most important electrolyte-related factor is its ability to maintain a significant flow of Al^{3+} ions from the metal substrate into the electrolyte. There are two ways to achieve this goal: electrical-field-driven direct expulsion of ions and dissolution of the forming oxide layer. At first, the Al^{3+} ions migrate from the metal substrate through the metal/oxide interface to the oxide layer, while O^{2-} ions from the water pass through the oxide/electrolyte interface into the oxide layer. In this stage, approximately 70% Al^{3+} and O^{2-} form a barrier layer, while the remaining Al^{3+} ions dissolve into the electrolyte. The barrier layer then is transformed into a semi-spherical oxide layer of constant thickness that forms the pore bottom. Fig 1.4 is a schematic diagram of pore formation mechanism in an acidic electrolyte (Poinern, GEJ., 2011).

The chemical reaction equation for the anodization of Al is:



The electric field at the base of the hemispherical shaped pores can push both Al^{3+} migration through the barrier layer and O^{2-} and OH^- migration from the metal/oxide interface into the pore base oxide layer, as shown in Fig 1.5. This process explains how the electric field can influence the size of the pore diameter. If the electric field is too small, there are not enough Al^{3+} ions to pass through the barrier layer, so there is less reaction to form the nanopores.

1.4 Surface chemistry and functionalization of AAO

AAO has unique nanostructure and properties that make it useful for biomedical sensing by surface functionalization. Surface chemistry and AAO functionalization provides an attractive and versatile strategy for use of AAO-based materials with different and improved physical and chemical properties. The surface of AAO can be coated with different materials, such as polymers (Ketul C, et al., 2004; Lee SW, et al., 2005; Simovic S, et al., 2010; Aw MS, et al., 2011; Bruening ML, et al., 2008; Nagale M, et al., 2000;), proteins (Milka P, et al., 2000; Ter Maat J, et al., 2011), nucleic acid (Matsumoto, F et al., 2004), metals (Narayan RJ, et al., 2008), oxides (Lee SB, et al., 2002; Winkler B, et al., 2003; Skoog SA, et al., 2012; Vajandar SK, et al., 2007), diamond (Aramesh M, et al, 2014; Skoog SA, et al., 2012), and diamond-like carbon (Narayan

R,J et al., 2008; Aramesh, M et al., 2014; Karan S, et al., 2012). The surface modification technique primarily utilized in this thesis is self-assembled monolayer formation.

AAO biosensors can detect small concentrations of analyte without sample contamination, although the surface chemistry is not suitable for biomedical applications, and the best approach to making the structure more biocompatible and chemically stable is to modify the surface with other materials. Fig 1.6 shows the surface functionalization process described in this thesis. First, we use sputtering to coat 10nm of gold on the top of the AAO, because gold binds thiols with high affinity, and the resulting films are stable to complex liquid media containing target biomolecules. Forming a mixed SAM of alkanethiols by adhesion reaction of the thiol group on a gold surface is a well-established method (X, Li, et al., 2012). The monolayer is well packed, and the tethered carboxylic acid is easy to functionalize for biological molecule immobilization (X, Li, et al., 2013). When EDC/NHS is present, its carboxylic groups form active O-acylisourea intermediates and readily react with primary amine groups exiting at the N-terminus of each polypeptide chain and in the side chains of lysine (Lys, K) residues. The aptamers then become tethered to the SAM via the terminal thiol group, as intended. In this way, aptamer active O-acylisourea intermediate groups are deactivated by the amino acid glycine to avoid non-specific biological attachment caused by the intermediates. At this stage, the aptamer is conjugated to the nanostructured surface and ready for analyte detection (X. Li et al., 2013).

1.5 Properties of AAO for optical sensing

AAO can be used to produce optical sensing platforms, active or passive, with capability to guide, reflect, absorb, transmit, emit, confine or enhance incident optical waves emitted by a source. Over the last decade, the use of nanomaterials as optical sensing platforms has made it possible to develop optical sensing systems with outstanding capabilities and performance in terms of sensitivity, selectivity, versatility and applicability. Some examples of optical techniques successfully combined with nanomaterials are surface-enhanced Raman spectroscopy (SERS), surface plasmon resonance spectroscopy (SPR), localized surface plasmon resonance spectroscopy (LSPR), reflectometric interference spectroscopy (RIFS) and photoluminescence (PL). Table 1.3 shows a summary of optical biosensors based on AAO platforms.

1.5.1 Surface-Enhanced Raman Scattering (SERS)

Surface-enhanced Raman scattering spectroscopy (SERS) is an ultra-sensitive optical technique based on enhancement of the Raman scattering that take place when biomolecules are absorbed on the surface of metal films featuring nanostructured roughness. AAO-based SERS substrates can be fabricated by depositing metals such as gold or silver on either top or bottom surfaces of AAO templates by thermal evaporation or sputtering. Other approaches have also been used to produce AAO-based SERS substrates, including metallic membranes, decoration of

nanopores with nanoparticles, and growth of nanowires, as shown in

Fig 1.7. The resulting AAO-based SERS substrates were used to detect trace amounts of an aromatic compound of TNT-based plastic explosive that cannot be detected using conventional Raman spectroscopy.

1.5.2 Surface Plasmon Resonance (SPR)

Surface plasmon resonance (SPR) is based on the generation of surface plasmons from an evanescent electromagnetic wave. This phenomenon occurs when a light beam is focused on the surface of a prism coated with a thin metallic film. This optical technique is typically implemented in a Kretschmann configuration. AAO structures can be used to develop unique SPR sensing systems, the most widespread method being to produce AAO-based SPR systems by growing a layer of AAO on the surface of a thin Al film deposited on the surface of the prism.

The result (Fig 1.8) shows that reflected spectra from the membrane is shifted in response to variation in CRP antigen concentration. The graph shows wavelengths from 600nm to 780nm. Increasing the CRP antigen concentration induces incremental increases in intensity, and the wavelength shifts in the reflectance spectra increase as the log of antigen concentration, offering a large dynamic range and high sensitivity of the chip for quantitative detection of CRP antigen. The λ_{max} of reflectance wavelength shifted dramatically with variations in CRP antigen concentration (from 1 fg/ml to 100 $\mu\text{g/ml}$) in CRP antigen-antibody reaction.

1.5.3 Reflectometric Interference Spectroscopy (RIFS)

For various AAO dimensions, geometry and chemical composition, AAO structures exhibit characteristic responses when they interact with light. Many studies have described applications of AAO to optical filters, waveguides, anti-reflective surfaces, resonators, or microcavities (B.Wang, et al., 2010; Y.Kanamori, et al., 2011). RIFS is a highly sensitive optical sensing technique based on the interaction of white light with thin films (G.gauglitz, et al., 1994). The RIFS spectrum of AAO produces fringes with well-resolved peaks generated by the Fabry-Perot effect (S.D.Alvarez, et al., 2009; T.Kumerial, et al., 2012). Fig 1.9 shows a RIFS set-up used to detect binding molecules in AAO nanopores. The wavelengths of peak maxima in the RIFS spectrum follow the Fabry-Perot relationship:

$$OT_{\text{eff}} = 2n_{\text{eff}}L \cos \theta = m\lambda$$

where n_{eff} is the effective refractive index of AAO, L_p is the pore length, and m is the order of the RIFS fringe whose maximum is located at wavelength λ . These peaks in the RIFS spectrum are useful for sensing because the binding molecules on the surface's inside pores will change the effective index of refraction and in turn the effective optical thickness, causing a shift in the reflected interface fringes.

Figure 10 portrays the capability for selectively monitoring binding interactions between antibodies and antigens, confirming that they produce a significant change in the effective optical thickness when for specific interactions.

1.6 Simulation for sensor surface functionalization

R-soft was used to perform simulation of sensor surface functionalization, and Fig1.11a shows an SEM image for the nanopore and the simulation figure (Fig 1.11b). In this simulation, I set up a AAO thickness of 4 μm with a 0.1 μm average nanopore diameter, with the air refractive index taken as 1 and the AAO refractive index taken as 1.67. The simulation monitored white light with a collimated beam, with the light wavelength between 400 nm and 700 nm with parallel rays. The simulation fringes are shown in Fig. 1. 11(c).

I then added layer-by-layer in the model to simulate surface functionalization, with the result shown in Fig1.12b. As can be seen, when chemical binding occurs, both on the nanopore surface and inside, the fringes shift, demonstrating the validity of our experimental process. I also simulated the fabricated sensor with non-uniform AAO nanopores of average thickness 2 μm and average diameter 0.05 μm (Fig1.13a). Comparing the results from uniform and non-uniform AAO revealed no significant difference. Using non-uniform AAO, I simulated adding different concentrations of theophylline, and as shown in Fig1.13b and Fig1.13c, as theophylline

concentration increased, fringe shifting increased. Compare simulation result with experimental result to validate my model.

1.7 Microfluidics capillary interface

Microfluidic devices are promising for applications that require precise displacement of small amounts of liquids or that can benefit from peculiar behaviors that liquids and chemical reactions exhibit at micrometer length scale (J. Durré and R. Zengerde., 2006). A microsystem is typically composed of three major components: impedance microsensors, open-channel capillary micropumps, and passive microfluidic stop-valves (F.Zang et al., 2015).

In our device, we focused on capillary micropumps and passive microfluidic stop-valves. Capillary pumps are comprised of microstructures of various shape with dimensions from 15-250 μm and positioned in the capillary pumps to encode a desired capillary pressure. The capillary pumps are designed to have a small flow resistance and are preceded by a constricted microchannel that acts as a flow resistance (M.Zimmermann et al., 2007). The passive stop-valve array prevents the liquid from getting into an undesired part of the platform because of a sharp change in the liquid-sidewall angle (F.Zang et al., 2015).

As will be shown below, a flow resistance in front of the capillary pump can also be used in capillary pumps to modulate the filling behavior of liquids. The flow rate Q of a liquid in

a CS is determined by the wettability of the CS, the viscosity of the liquid, the total flow resistance, and the capillary pressure in the capillary pump, and can be expressed as

$$Q = \frac{1}{\eta} \frac{\Delta P}{R_F} \quad (1)$$

where η is the viscosity of the liquid, the difference in pressure inside and in front of the liquid.

the total resistance to flow of the flow path, a microchannel of variable length dominates the flow resistance. The resulting pressure of a liquid-air meniscus in such a rectangular microchannel is

$$P_C = -\gamma \left(\frac{\cos \alpha_b + \cos \alpha_t}{a} + \frac{\cos \alpha_l + \cos \alpha_r}{b} \right) \quad (2)$$

where γ is the surface tension of the liquid are the contact angles of the liquid on the bottom, top, left, and right wall, respectively, and a and b are the depth and width of the microchannel, respectively (M. Zimmermann et al., 2007). The flow resistance of such microchannels is a geometric term expressed as a Fourier series and can be approximated by a linear term (J.H.Spurk et al., 2004).

$$R_F = \left[\frac{1}{12} \left(1 + \frac{5}{6} \frac{a}{b} \right) \frac{abR_H^2}{L} \right]^{-1} \quad (3)$$

satisfying the condition, a, b . Here L is the length of the microchannel and R_H is the hydraulic radius of the microchannel,

$$R_H = \frac{2A}{P} = \frac{ab}{a+b} \quad (4)$$

with P being the perimeter and A the area of the cross section of the microchannel. The flow in a

microchannel can thus be estimated using the capillary pressure divided by the flow resistance that continually increases as the channel is being filled (M.Zimmermann et al., 2007).

References

- A.G. Koutsoubas, N. Spiliopoulos, D. Anastassopoulos, A.A. Vradis, G.D. Priftis., 2008. Nanoporous alumina enhanced surface plasmon resonance sensors. *J. Appl. Phys.* 103, 094521.
- Abel Santos., Tushar Kumeria., Dusan Losic., 2014. Nanoporous anodic aluminum oxide for chemical sensing and biosensors. *Analytical Chemistry*. 7(6):4297-4320.
- Akira Miyata and Shoji Setoh., 1932. Researches on the anodic film of aluminium, II. Anodic behaviours of aluminium in aqueous solutions of oxalic acid. Science Papers of the Institute For. Physics and Chemistry Research, Tokyo. 19: 237.*
- Alvarez SD., Li CP., Chiang CE., Schuller IK., Sailor MJ., 2009. A label-free porous alumina interferometric immunosensor. *ACS Nano*. 3(10):3301–7.
- Aramesh M., Fox K., Lau DWM., Fang JH., Ostrikov K., Prawer S., Cervenka J., 2014. Multifunctional threedimensional nanodiamond-nanoporous alumina nanoarchitectures. *Carbon*. 75:452- 464.
- Aw MS., Simovic S., Addai-Mensah J., Losic D., 2011. Polymeric micelles in porous and nanotubular implants as a new system for extended delivery of poorly soluble drugs. *Journal of Materials Chemistry*. 21(20):7082.
- Bruening ML., Dotzauer DM., Jain P., Ouyang L., Baker GL., 2008. Creation of Functional Membranes Using Polyelectrolyte Multilayers and Polymer Brushes. *Langmuir: the ACS journal of surfaces and colloids*. 24:7663-73.
- D.K. Kim, K. Kerman, M. Saito, R.R. Sathuluri, T. Endo, S. Yamamura, Y.S. Kwon, E. Tamiya., 2007. Label-free DNA biosensor based on localized surface plasmon resonance coupled with interferometry. *Anal. Chem*. 79, 1855–1864.
- E. Hourdakakis and A. G. Nassiopoulou., 2010. High-Density MIM capacitors with porous anodic

alumina dielectric. IEEE Transactions on Electron Devices, vol. 57, no. 10, pp. 2679-2683.

F. Casanova, C.E. Chiang, C.P. Li, I.V. Roshchin, A.M. Ruminski, M.J. Sailor., 2008. Gas adsorption and capillary condensation in nanoporous alumina films. Nanotechnology 19, 315709.

F. Keller., M.S. Hunter., D. L. Robinson., J. Electrochem., 1953. Structural Features of Oxide Coatings on Aluminum. Journal of the Electrochemical Society. 100 (9): 411. doi:10.1149/1.2781142.

G. Gauglitz, A. Brecht, G. Kraus, W. Nahm., 1993. Chemical and biochemical sensors based on interferometry at thin (multi-) layers. Sensor. Actuat. B 11, 21–27.

G. Gauglitz, J. Ingenhoff., 1994. Design of new integrated optical substrates for immuno-analytical applications. Fresenius' J. Anal. Chem. 349, 355–359.

G. Sulka, S. Stroobants, V. Moshchalkov, G. Borghs, J.P. Celis, J., 2002. Synthesis of well-ordered nanopores by anodizing aluminum foils in sulfuric acid. Electrochemal Society, Vol.149, No.7, D97-D103.

H. Masuda., K. Fukuda., 1995. Ordered metal nanohole arrays made by a 2-step replication of honeycomb structures of anodic alumina. Science. 268 (5216): 1466
8. Bibcode:1995Sci...268.1466M. doi:10.1126/science.268.5216.1466. JSTOR 2887752. PMID 17843666.

H. Zhuo, F. Peng, L. Lin, Y. Qu, F. Lai., 2011. Optical properties of porous anodic aluminum oxide thin films on quartz substrates. Thin Solid Films, 519, 2308–2312.

Hoar, T.P., Mott, N.F., 1959. A mechanism for the formation of porous anodic oxide films on aluminium. J. Phys. Chem. Solids. 9, 97-99. 26.

Hoar, T.P., Yahaloom, J., 1963. The initiation of pores in anodic oxide films formed on aluminium in acid solutions. J. Electrochem. Soc. 110, 614-621.

Houghton, P.S., 1960. Heat Treatment of Metals. Machinery Pub.: London, UK. Volume 2, p. 89.

Hourdakakis, E. and Nassiopoulou, A.G., 2012. High performance MIM capacitor using anodic alumina dielectric. *Microelectronic Engineering* vol. 90, pp. 12-14.

Ivan Vlassiouk., Alexey Krasnoslobodtsev., Sergei Smirnov., Markus Germann., 2004. Direct detection and separation of DNA using nanoporous alumina filters. *Langmuir*. 20(23):9913–5.

J. Ducreé and R. Zengerde., 2006. *Microfluidics*. Springer MEMS, Berlin 2006, pp 667-727.

J. Homola, S.S. Yee, G. Gauglitz., 1999. Surface plasmon resonance sensors: review. *Sens. Actuators, B* 54, 3–15.

J. P. O'Sullivan., G.C. Wood., 1970. The Morphology and Mechanism of Formation of Porous Anodic Films on Aluminium. Proc. Roy. Soc. Lond. A317 (1531):511
543. Bibcode:1970RSPSA.317..511O. doi:10.1098/rspa.1970.0129.

J.H.Spurk, in *Strömungslehre*, Springer, Berlin, 2004, pp. 164-167.

Jenny, A., Lewis, W., 1959. *The Anodic Oxidation of Aluminium and Its Alloy*; Charles Griffin and Company Limited: London, UK.

K. Hotta, A. Yamaguchi, N. Teramae., 2012. Nanoporous waveguide sensor with optimized nanoarchitectures for highly sensitive label-free biosensing. *ACS Nano* 6, 1541–1547.

K.H.A. Lau, L.S. Tan, K. Tamada, M.S. Sander, W. Knoll., 2004. Highly sensitive detection of processes occurring inside nanoporous anodic alumina templates: a waveguide optical study. *J. Phys. Chem. B* 108, 10812–10818.

Karan S., Samitsu S., Peng X., Kurashima K., Ichinose I., 2012. Ultrafast viscous permeation of organic solvents through diamond-like carbon nanosheets. *Science*. 335(6067):444-7.

Keller, F., Hunter., M.S., Robinson, D.L., 1953. Structural features of oxide coatings on aluminium. *J. Electrochemical. Soc.* 100, 411-419.

Ketul C., Popat GM., Craig A., Grimes,Tejal A. Desai., 2004. Surface Modification of Nanoporous Alumina Surfaces with Poly(ethylene glycol). *Langmuir: the ACS journal of surfaces and colloids*. 20, 19, 8035-8041.

- Kovtyukhova NI., Mallouk TE., Mayer TS., 2003. Templated surface sol-gel synthesis of SiO₂ nanotubes and SiO₂-insulated metal nanowires. *Advanced materials*. 15(10):780-5.
- La Flamme KE., Popat KC., Leoni L., Markiewicz E., La Tempa TJ., Roman BB., Grimes CA., Desai TA., 2007. Biocompatibility of nanoporous alumina membranes for immune isolation. *Biomaterials*. 28(16):2638–45.
- Lee SB., Mitchell DT., Trofin L., Nevanen TK., Soderlund H., Martin CR., 2002. Antibody-based bionanotube membranes for enantiomeric drug separations. *Science*. 296(5576):2198-200.
- Lee SW., Shang H., Haasch RT., Petrova V., Lee GU., 2005. Transport and functional behaviour of poly(ethylene glycol)-modified nanoporous alumina membranes. *Nanotechnology*. 16(8):1335-40.
- Li, F. Muller, A. Birner, K. Nielsch, U. Gosele, Adv., 1999. Fabrication and microstructuring of hexagonally ordered two-dimensional nanopore arrays in anodic alumina. *Advanced Materials*. Vol. 11, Issue6, 483–487.
- M. A. Cameron IPG., J. A. Smith., S. F. Diaz., S. M. George., 2000. Atomic Layer Deposition of SiO₂ and TiO₂ in Alumina Tubular Membranes: Pore Reduction and Effect of Surface Species on Gas Transport. *Langmuir: the ACS journal of surfaces and colloids*. 16,19,7435-7444.
- Martin Zimmermann, Heinz Schmid, Patrick Hunziker and Emmanuel Delamarhe., 2007. Capillary pumps for autonomous capillary systems. *Lab Chip*, 7, 119-125.
- Masuda, H., Fukuda, K., 1995. Ordered metal nanohole arrays made by a two-step replication of honeycomb structures of anodic alumina. *Science*. Vol.268, Issue 5216, pp.1466-1468.
- Masuda, H., Satoh, M., 1996. Fabrication of gold nanodot array using anodic porous alumina as an evaporation mask. *Jpn. J. Appl. Phys.* 35, L126.
- Matsumoto F., Nishio, K., Masuda, H., 2004. Flow-through-type DNA array based on ideally ordered anodic porous alumina substrate. *Advanced materials*. 16(23-24):2105-8.
- Milka P., Krest, I., Keusgen, M., 2000. Immobilization of Alliinase on Porous Aluminum Oxide. *Biotechnology and Bioengineering*. 69(3):344-8.

- Nagale M., Kim, B.Y., Bruening, M.L., 2000. Ultrathin, Hyperbranched Poly (acrylic acid) Membranes on Porous Alumina Supports. *J Am Chem Soc.*122:11670-8.
- Narayan R.J., Aggarwal R., Wei W., Jin C., Monteiro-Riviere NA., Crombez R, et al., 2008. Mechanical and biological properties of nanoporous carbon membranes. *Biomedical materials.* 3(3):034107.
- Pacholski, M. Sartor, M.J. Sailor, F. Cunin, G.M. Miskelly., 2005. Biosensing using porous silicon double-layer interferometers: reflective interferometric Fourier transform spectroscopy. *J. Am. Chem. Soc.* 127, 11636–11645.
- Pan S., Rothberg L.J., 2003. Interferometric sensing of biomolecular binding using nanoporous aluminum oxide templates. *Nano Lett.* 3(6):811–4.
- Q. Wei., H. Qi., W. Luo., D. Tseng., S.J. Ki., Z. Wan., Z. Göröcs., L.A. Bentolila., T.T. Wu., R. Sun., A. Ozcan., 2013. Fluorescent imaging of single nanoparticles and viruses on a smart phone. *ACS Nano* 10, 9147–9155.
- Q. Wei., R. Nagi., K. Sadeghi., S. Feng., E. Yan., S.J. Ki., R. Caire, D., Tseng, A. Ozcan., 2014. Detection and spatial mapping of mercury contamination in water samples using a smart phone. *ACS Nano* 2, 1121–1129.
- R. Dronov, A. Jane, J.G. Shapter, A. Hodges, N.H. Voelcker., 2011. Nanoporous alumina-based interferometric transducers ennobled. *Nanoscale* 3, 3109–3114.
- R.J. Green, R.A. Frazier, K.M. Shakesheff, M.C. Davies, C.J. Roberts, S.J.B. Tendler., 2000. Surface plasmon resonance analysis of dynamic biological interactions with biomaterials. *Biomaterials* 21, 1823–1835.
- S. Ayas, A. Cupallari, O.O. Ekiz, Y. Kaya, A. Dana., 2014. Counting molecules with a mobile phone camera using plasmonic enhancement. *ACS Photonics* 1, 17–26.
- S. Khatua., M. Orrit., 2013. Toward single-molecule microscopy on a smart phone. *ACS Nano* 10, 8340–8343.

S. Pan, L.J. Rothberg., 2003. Interferometric sensing of biomolecular binding using nanoporous aluminum oxide templates. *Nano Lett.* 3, 811–814.

S.H. Yeom, O.G. Kim, B.H. Kang, K.J. Kim, H. Yuan, D.H. Kwon, H.R. Kim, S.W. Kang., 2011. Highly sensitive nano-porous lattice biosensor based on localized surface plasmon resonance and interference. *Opt. Express* 19, 22882–22890.

Simovic S., Losic D., Vasilev K., 2010. Controlled drug release from porous materials by plasma polymer deposition. *Chemical communications.* 46(8):1317-9.

Skoog SA., Bayati MR., Petrochenko PE., Stafslie S., Daniels J., Cilz N, et al., 2012. Antibacterial activity of zinc oxide-coated nanoporous alumina. *Materials Science and Engineering: B.* 177(12):992-8.

Skoog SA., Sumant AV., Monteiro-Riviere NA., Narayan RJ., 2012. Ultrananocrystalline Diamond-Coated Microporous Silicon Nitride Membranes for Medical Implant Applications. *Jom.* 64(4):520-5.

Smith.A., 1974. Process for producing an anodic aluminum oxide membrane. U.S. Patent 3,850,762.

T. Kumeria, D. Losic., 2011. Reflective interferometric gas sensing using nanoporous anodic aluminium oxide (AAO). *Phys. Status Solidi RRL* 5, 10–11.

T. Kumeria, M.D. Kurkuri, K.R. Diener, L. Parkinson, D. Losic., 2012. Label-free reflectometric interference microchip biosensor based on nanoporous alumina for detection of circulating tumour cells. *Biosens. Bioelectron.* 35, 167–173.

Takmakov P., Vlassiuk I., Smirnov S., 2006. Application of anodized aluminum in fluorescence detection of biological species. *Anal Bioanal Chem.* 385(5):954–8.

Ter Maat J., Regeling R., Ingham CJ., Weijers CA., Giesbers M., de Vos WM, et al., 2011. Organic modification and subsequent biofunctionalization of porous anodic alumina using terminal alkynes. *Langmuir: the ACS journal of surfaces and colloids.* 27(22):13606-17.

Thompson, G.E., 1997. Porous anodic alumina: Fabrication, characterisation and application.

Thin Solid Films. 297, 192-201.

Vajandar SK., Xu D., Markov DA., Wikswo JP., Hofmeister W., Li D., 2007. SiO₂-coated porous anodic alumina membranes for high flow rate electroosmotic pumping. *Nanotechnology*. 18(27):275705.

Wang M., Meng G., Huang Q., Li M., Li Z., Tang C., 2011. Fluorescence detection of trace PCB101 based on PITC immobilized on porous AAO membrane. *Analyst*. 136(2):278-81.

Winkler B. 2003. Modification of the surface characteristics of anodic alumina membranes using sol-gel precursor chemistry. *Journal of Membrane Science*. 226(1-2):75-84.

X. Li, Y. He and L. Que., 2013. Fluorescence detection and imaging of biomolecules using the micropatterned nanostructured aluminum oxide. *Langmuir*, 29 (7), pp 2439-2445.

X. Li, Y. He, T. Zhang and L. Que., 2012. Aluminum oxide nanostructure-based substrates for fluorescence enhancement. *Optics Express*, Vol. 20, No. 19, pp. 21272-21277.

X. Li, Y. He, T. Zhang, T. Lee and L. Que., 2012. Lithographically patterned anodic aluminum oxide (AAO) nanostructures for fluorescence enhancement. *Proceeding of IEEE NANO 2012*, pp. 1-4.

Y. He, X. Li and L. Que., 2012. Fabrication and characterization of lithographically patterned and optically transparent anodic aluminum oxide (AAO) nanostructure thin film. *Journal of Nanoscience and Nanotechnology (JNN)*, Vol. 12, No. 10, 7915-7921.

Y.D. Ivanov, T.O. Pleshakova, N.V. Krohin, A.L. Kaysheva, S.A. Usanov, A.I. Archakov., 2013. Registration of the protein with compact disk. *Biosens. Bioelectron*. 43, 384-390.

Yang Z., Si S., Dai H., Zhang C., 2007. Piezoelectric urea biosensor based on immobilization of urease onto nanoporous alumina membranes. *Biosens Bioelectron*. 22(12):3283-7.

Zang, F., Gerasopoulos, K.D., McKinzie, K.K., Culver, J.N., & Ghodssi, R., 2015. Autonomous capillary microfluidics for rapid nanoreceptor assembly and biosensing. 2015 Transducers - 2015 18th International Conference on Solid-State Sensors, Actuators and Microsystems (TRANSDUCERS), 548-551.

Figures and Tables

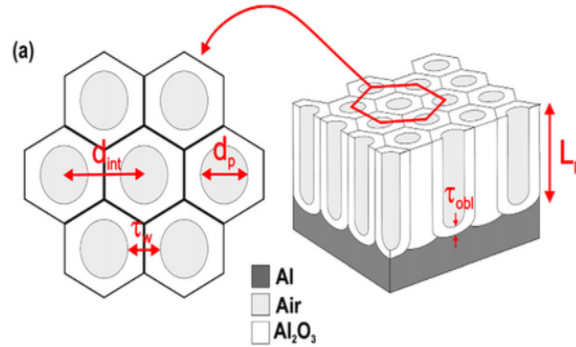


Figure 1. 1 Anodic aluminum oxide (AAO) structure. Pore structure in AAO and definition of the main structural parameters

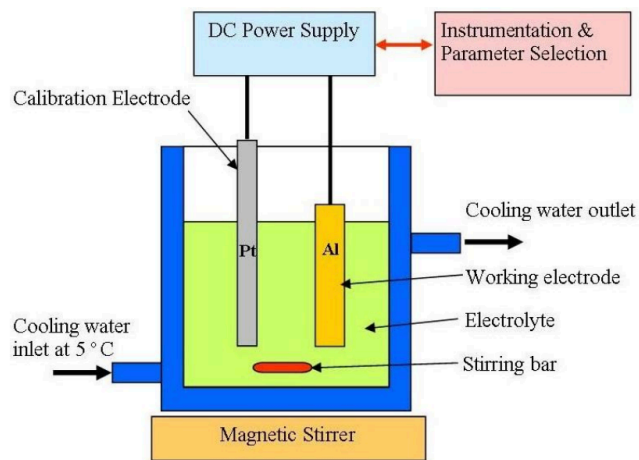


Figure 1. 2 Experimental equipment used to produce anodized aluminum oxide (Gerrard Eddy Jai Poinern., 2011)

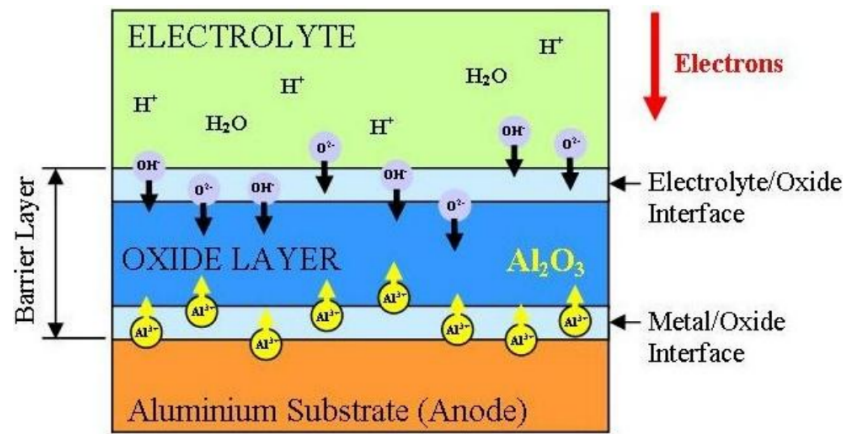


Figure 1. 3 Schematic of the major features involved in the formation of the barrier layer

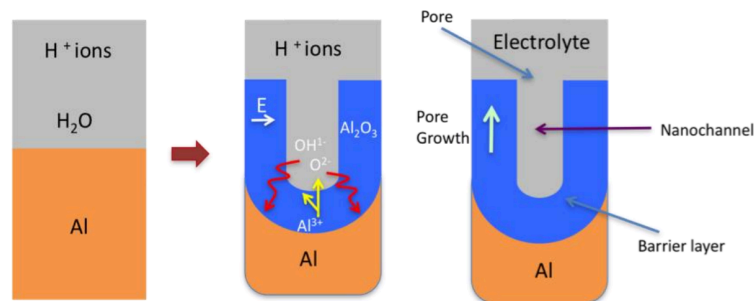


Figure 1. 4 Schematic of the pore formation mechanism in an acidic electrolyte (Poinern GEJ., 2011)

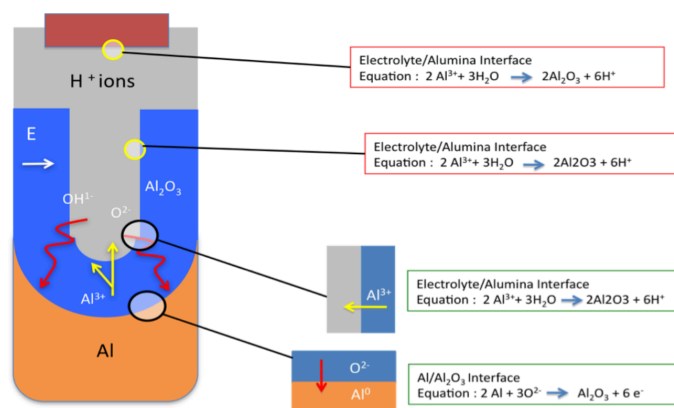


Figure 1. 5 Schematic of ion movement during pore formation (Poinern GEJ., 2011)

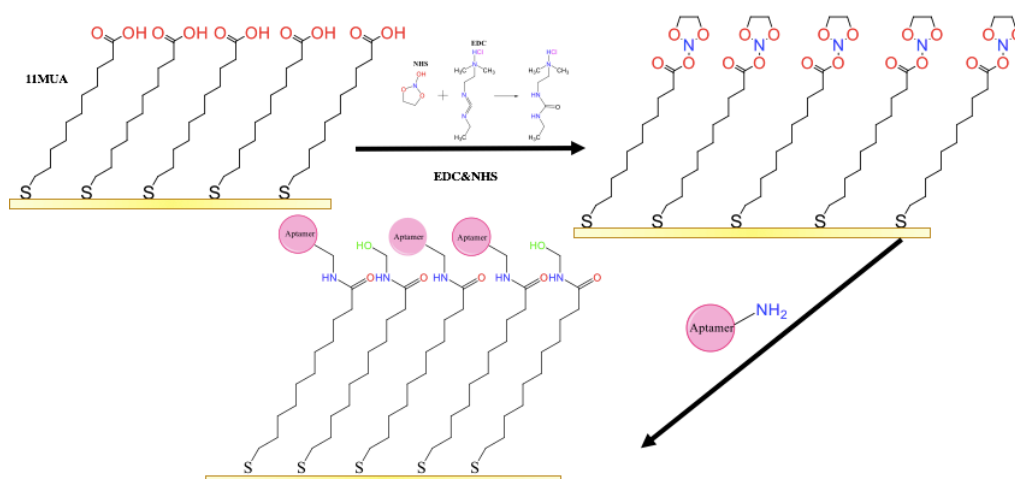


Figure 1. 6 Surface functionalization process

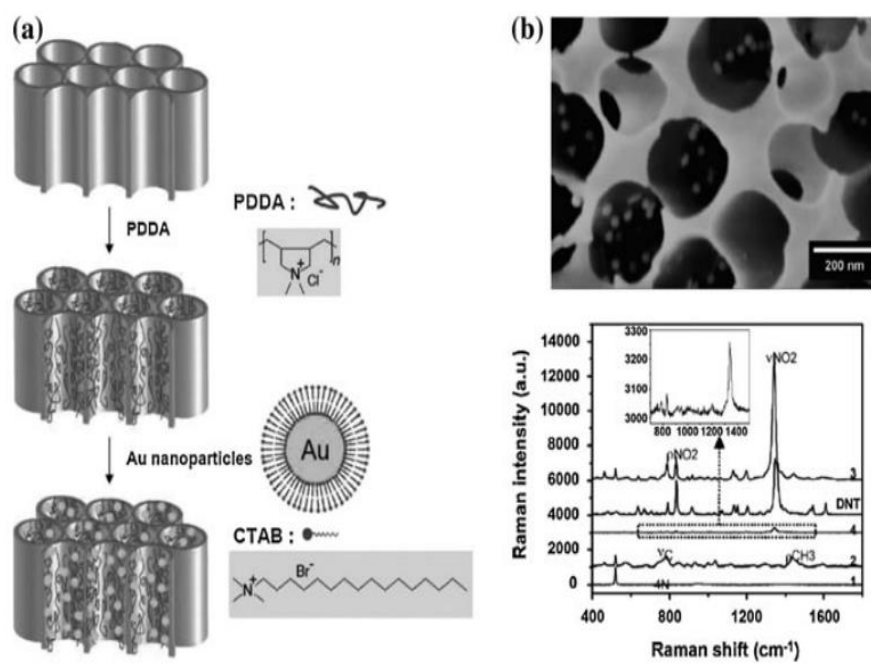


Figure 1. 7 AAO-based system. (a) Fabrication process based on gold nanoparticles. (b) SEM image of the SERS systems and sensing performance

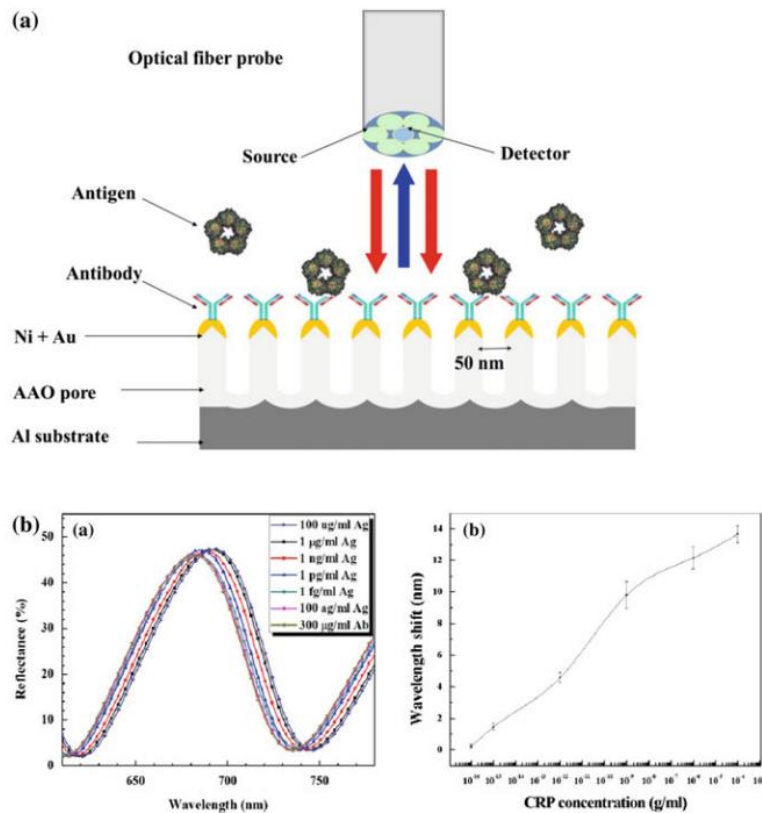


Figure 1. 8 AAO-based SPR systems. (a) Structure of a LSPR system based on AAO coated with gold and chemically functionalized with antibodies to target C-reactive protein antigens. (b) Sensing performance of that system when detecting C-reactive protein

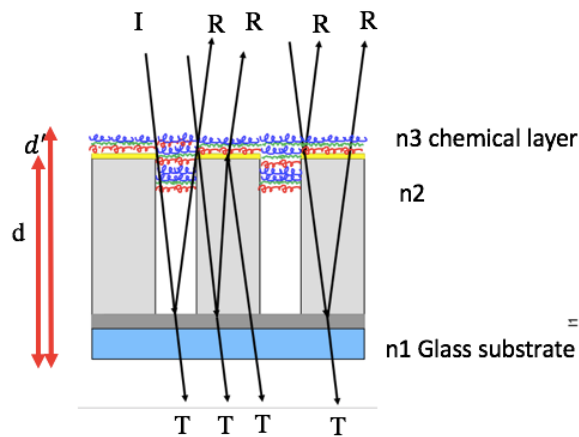


Figure 1. 9 Schematic diagram of a reflectometric interference spectroscopy anodic aluminum oxide (RIFS-AAO) set-up for biosensing applications

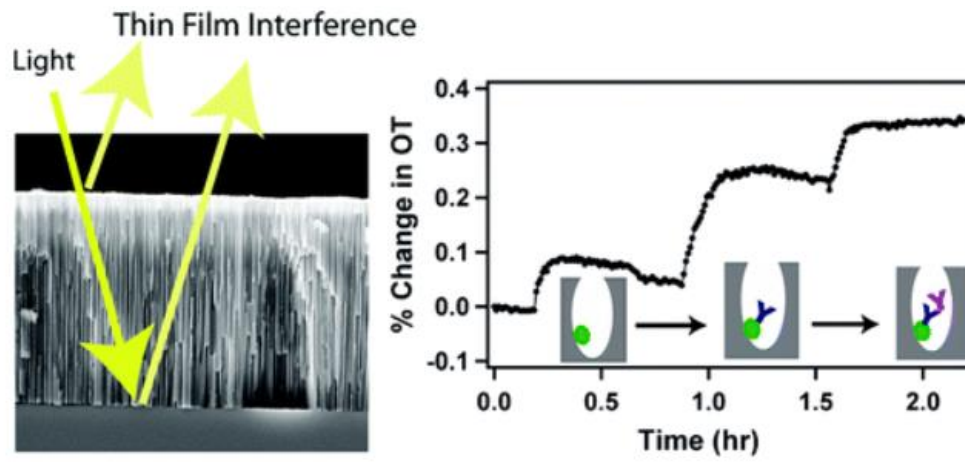


Figure 1. 10 Sensing principle of a AAO-RIFS system and real-time monitoring of antibody-antigen interactions

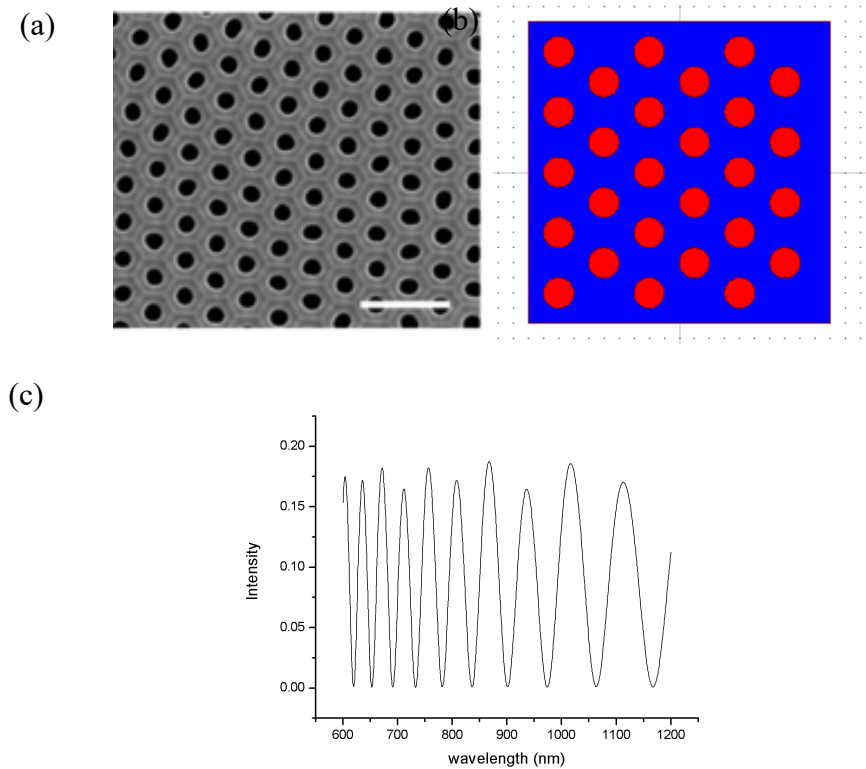


Figure 1. 11 (a) SEM image for AAO; (b) Schematic for simulation; (c) Simulation result for AAO fringes

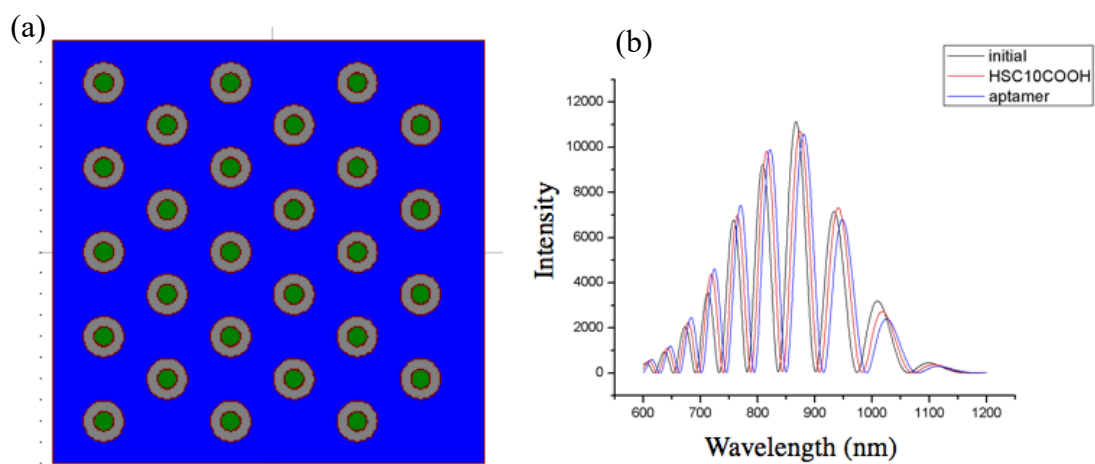
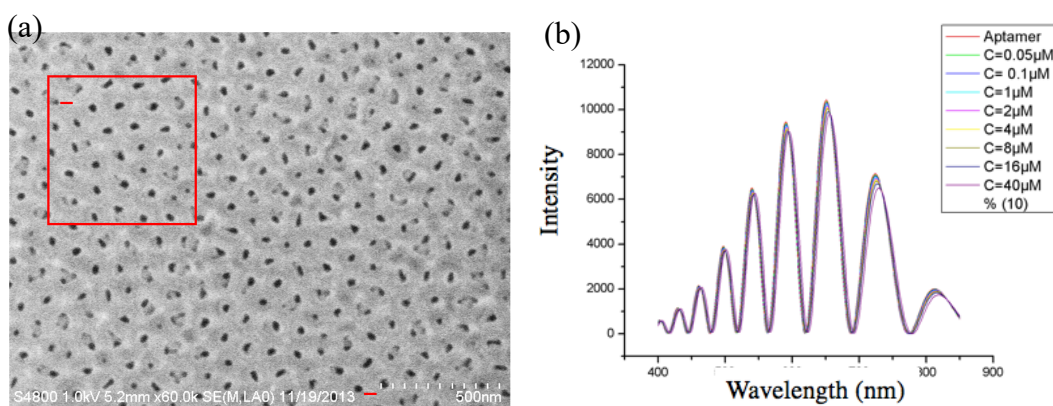


Figure 1. 12 (a) Schematic for surface functionalization; (b) Result for simulation after surface functionalization



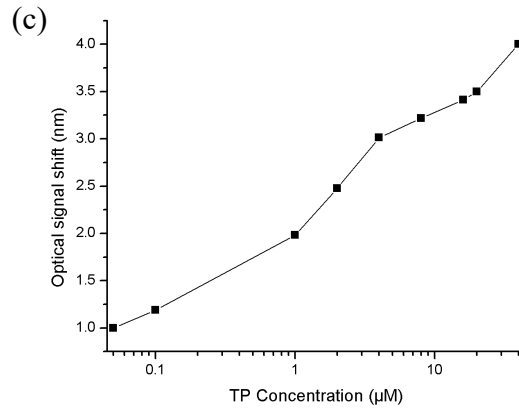


Figure 1. 13 (a) SEM image for non-uniform nanopores; (b) Optical signals due to different concentrations; (c) Measured shift of optical signals

Table 1. 1 Major acid components of typical electrolyte types used to produce porous oxide layer on an aluminum substrate (Poinern GEJ., 2011)

Main Acid used in Electrolyte	Molecular Formula	Concentration (M)	Pore Size Range (nm)
Acetic	$\text{CH}_3\text{CO}_2\text{H}$	1	Not specified
Citric	$\text{HO}_2\text{CCH}_2(\text{OH})(\text{CO}_2\text{H})\text{CH}_2\text{CO}_2\text{H}$	0.1 to 2	90 to 250
Chromic	H_2CrO_4	0.3, 0.44	17 to 100
Glycolic	$\text{CH}_2(\text{OH})\text{CO}_2\text{H}$	1.3	35
Malic	$\text{HO}_2\text{CH}_2\text{CH}(\text{OH})\text{CO}_2\text{H}$	0.15 to 0.3	Not specified
Malonic	$\text{CH}_2(\text{CO}_2\text{H})_2$	0.1 to 5	Not specified
Oxalic	$\text{C}_2\text{H}_2\text{O}_4$	0.2 to 0.5	20 to 80
Phosphoric	H_3PO_4	0.04 to 1.1	30 to 235
Sulfuric	H_2SO_4	0.18 to 2.5	12 to 100
Tartaric	$\text{HO}_2\text{CCH}(\text{OH})\text{CH}(\text{OH})\text{CO}_2\text{H}$	0.1 to 3	Not specified

Table 1. 2 Voltage and times of three commonly used electrolytes for the production of porous oxide layer on an aluminum substrate

Acid	Concentration. (M)	Voltage (volts)	Pore Size (nm)	Time (hours)
Oxalic	0.25	60	75	8,8
	0.3	40	Not specified	variable
	0.3	40	80	8, variable
	0.3	40	50	10,5 min
	0.3	60	80	3,8
	0.3	40	40–50	40 min, 2
	0.3	40, 50	20,35	variable
	0.3	30	40	8,10
	0.4	40	50	8,10
	0.5	50	80	8,10
	0.3	40	22	12,4,8,12& 16
	0.3	40	22	12,4,8,12& 16
Phosphoric	Not specified	195	200	variable
	0.4	5 to 40	20 to 75	1 step/variable
	0.4	80	80	1 step
	0.42	87 to 117	64 to 79	1 step/variable
Sulfuric	0.5	18	70	4, variable
	2.4	15 to 25	13 to 27	2 step/variable
	Not specified	12, 25, 40	25,50, 100	Not specified
	0.3	25	20	12, 4,8,12&16

Table 1. 3 Summary of optical biosensors based on AAO (also called NAA) platforms

Sensing system	Analyte	Detection limit
SERS-NAA	p-Aminothiophenol	0.5 M
	4-Mercaptopyridine	$1 \cdot 10^{-6}$ M
	3-Mercaptobenzoic	3 mM
	Benzenethiol	500 ppb
	N-Methyl-4-nitroaniline	3 ppb
SPR-NAA	Avidin	$10 \mu\text{g mL}^{-1}$
	Anti-5-fluorouracil	100 mg mL^{-1}
	Melittin	100 ng mL^{-1}
	$\text{Ru}[\text{BPhen}_3]^{2+}$	2 μM
	$\text{Fe}[\text{Phen}_3]^{2+}$	1 μM
	BSA	60 nM
	Invertase	10 nM
RIFS-NAA	H_2S	0.5 v%
	DNA	2 nmol cm^{-2}
	Circulating tumour cells	$1000 \text{ cells mL}^{-1}$
	Immunoglobulin	0.1 mg mL^{-1}
	Glucose	100 mM
	Cysteine	5 mM
	Gold(III)	0.1 μM
	BSA	1 mg mL^{-1}
	Glucose	0.01 M
	BSA	15 μM
	Human IgG	600 nM
PL-NAA	Morin	$5 \cdot 10^{-6}$ M
	Trypsin	$40 \mu\text{g mL}^{-1}$
		0.1 mg mL^{-1}
	DNA	100 mM
	Oxazine 170	$6.5 \cdot 10^{-3}$ M
	Glucose	0.1 M
	Glucose	10 mM
	Cysteine	5 mM

CHAPTER 2. AN APTAMER NANOPORE-ENABLED MICROSENSOR FOR DETECTION OF THEOPHYLLINE

Abstract

This paper reports an aptamer-based nanopore thin film sensor for detecting theophylline in a buffer solution and in complex fluids, including plant extracts and serum samples. Compared to antibody-based detection, aptamer-based detection offers many advantages such as lower cost and higher stability at elevated temperatures. Experiments showed that this type of sensor can readily detect theophylline at a concentration as low as 0.05 μM , much lower than the detection limit of current lab-based methods such as liquid chromatography (LC). Experiments also found that such an aptamer-based sensor has good specificity, selectivity, and reasonable reusability with a significantly improved dynamic detection range. Theophylline in plant extracts and serum was detected using the same nanopore thin-film sensors as the reference sensors to further mitigate the non-specific binding effect, and only a small amount ($\sim 1 \mu\text{L}$) of plant extracts or serum samples was required to measure the theophylline. Low cost and ease of operation make this type of sensor suitable for point-of-care application to monitoring the theophylline level of patients in real time.

Key words: Aptamer-based biosensing, Nano thin film sensor, Theophylline detection, Plant extract, Serum sample

2.1 Introduction

Theophylline (TP) is a drug used for its bronchodilator effect for treatment of respiratory diseases such as asthma (Barnes and Pauwels, 1994). The plasma levels of TP useful for effective bronchodilation action lie in a narrow concentration range, from 20 μ M to 100 μ M. TP becomes toxic at higher concentrations and can be lethal or permanent neurological damage (Dawson and Whyte, 1999). This narrow safety range means that TP levels within the body or in a sample should be monitored quickly and regularly. For example, blood samples from patients are usually used to monitor the TP levels in current clinical practice, and since an amount in excess of 25 mL of each blood sample is usually required, more than one sample may be needed for a test, and it can become problematic for patients to regularly provide such blood samples. Because of the great importance of monitoring theophylline levels in blood regularly because of its toxicological effects, use of a sensor capable of detecting theophylline on-site with small sample sizes (< 100 μ L or lower) becomes increasingly critical.

Current widely used clinical laboratory procedures for serum or plasma theophylline detection include radioimmunoassay (Cook, et al., 1976), high performance gas or liquid chromatography (Srdjenovic, et al., 2008), and fluorescence polarization immunoassay (Jolley, 1981). However, these methods usually require skilled personnel for operation, sample pre-treatment, and extended analysis time. These detection approaches also can suffer from

interference, primarily from chemicals such as caffeine and theobromine with similar structures. As a result, serum/plasma theophylline concentrations can be over-estimated. While it has been demonstrated that specificity of theophylline detection can be enhanced using theophylline oxidizing enzyme assays (Ferapontova, et al., 2007), this type of assay cannot be routinely used in clinical application because of restricted availability and stability of the enzyme. To address these issues, different types of sensors have been developed. Examples include studying electrochemical oxidation of theophylline using a variety of electrode substrates (Ferapontova, et al., 2008; Ulyanova, et al., 2006; Wang, et al., 2014). All these reported technologies have some advantages and disadvantages. For example, the dynamic range for detecting theophylline using these sensors is typically quite small (from 0.2 μM to 10 μM), and it is relatively difficult to extend this range (Ferapontova, et al., 2008; Rankin, et al., 2006). Ideally, a new type of sensor with large dynamic range that can detect theophylline rapidly in a simple and inexpensive manner, will be developed.

Antibody-based sensing, available for more than three decades, has been widely applied to biodetection (Alzghoul, et al., 2016; Zhang, et al., 2012). In recent years, aptamers, because they can overcome the weaknesses of antibodies, have increasingly become favorable as a substitute for antibodies (Song, et al., 2012). Specifically, aptamers have the following favorable properties: very good heat stability, ease of synthesis, cost-effectiveness, and a wide tolerance

range of pH and salt concentrations. Aptamers also offer similar, if not better, specificity and affinity to antibodies. Finally, aptamers can be reversibly denatured for the release of target molecules, making aptamer-based sensors can potentially reusable (Song, et al., 2012). All these features make them better receptors than antibodies for biosensing applications. In this paper, detection of theophylline by an aptamer-based label-free sensor is reported and demonstrated. The aptamer-based label-free sensor (Fig. 2.1a) is adapted from a nanostructured Fabry-Perot interference (nanoFPI) sensor developed in our lab (Zhang, et al., 2010, 2012). In this type of sensor, a layer of nanopores in anodic aluminium oxide (AAO) embedded in the Fabry-Perot cavity, serves as the sensing element. The reflected white light from the nanoFPI sensor forms interference fringes that can be used as transducing signals.

2. 2 Materials and methods

2.2.1 Fabrication of the nanopore thin film-based sensor

The sensor is fabricated using the process flow developed in our lab (Yin, et al., 2014) and illustrated in Fig. 2.1b. Briefly, after a 5-min baking of a rigorously cleaned cover-slip glass substrate, 10 nm Cr is deposited, followed by depositing a 2–3 μm thick aluminium (99.999%) layer using E-beam evaporation. Then a two-step anodization process in an acid solution (0.3 M oxalic acid) with 30 V DC voltage at 5.8 $^{\circ}\text{C}$ is used to form the anodic aluminium oxide (AAO), forming an AAO layer on the entire glass substrate surface. A layer (150 nm) of Al is then

coated on AAO, followed by photolithography of patterns that are then transferred to the Al layer by etching the unprotected Al area in an etching solution $\{(H_3PO_4:CH_3COOH:HNO_3:H_2O) 80:5:5:10 \text{ by weight } \%\}$ for 35 s. The patterned Al is subsequently used as a mask. The substrate is immersed in a mixture of phosphoric acid (0.4 M) and chromic acid (0.2 M) at 20 °C for 100 min to etch away the unprotected AAO and transfer the Al patterns into the AAO layer, and the Al is finally etched away. An AAO-glass chip is then fabricated by depositing a layer of 10 nm Au on the AAO surface, using a layer of Cr (5 Å) as an adhesion layer. A poly-dimethylsiloxane (PDMS) microfluidic chip, separately fabricated using a soft lithography process, is then bonded with the AAO-glass chip after a 2-min oxygen plasma treatment of the AAO glass chip and the PDMS microfluidic chip, followed by assembly of input and output plastic tubes. Fig. 2.1c is a photo of the sensor chip comprised of arrayed nanopore-based sensors, and Fig. 2.1d shows a representative SEM image of the fabricated AAO.

2.2.2 Chemicals and materials

11-Mercaptoundecanoic acid ($HSC_{10}COOH$, 99%), 8-Mercapto-1- Octanol (HSC_8OH , 98%), N-(3-Dimethylaminopropyl)-N'-ethylcarbo-diimide hydrochloride (EDC), N-Hydroxysuccinimide (NHS), and ethanolamine (EA), Phosphoric acid (PPA) and PBS buffer were purchased from Sigma-Aldrich (Milwaukee, WI) and used without further purification. Deionized (DI) water was obtained from a DI water purification system (Millipore, FRANCE).

A series of concentrations (0, 0.05, 0.1, 0.2, 1, 2, 4, 8, 16, 32, 48 μM) of theophylline were dissolved in 10mM pH7.2 PBS with 5mM KCl and 1mM MgCl_2 . 0, 4, 20, 40 μM theophylline were dissolved in plant extract using 10 mM pH7.2 PBS with 5 mM KCl and 1 mM MgCl_2 . 0, 4, 20, 40 μM theophylline was dissolved in Newborn Calf Serum from Thermo Fisher Scientific (Waltham, MA, USA) diluted 20 times with PBS. SUPERase in RNase Inhibitor was purchased from Thermo Fisher Scientific (Waltham, MA, USA).

The aptamer (Integrated DNA Technologies, Inc) for theophylline, purchased from VWR International (Radnor, PA, USA), is:

5'-NH₂-(CH₂)₆ArGrUrGrArUrArCrCrArGrCrArUrCrGrUrCrUrUrGr
ArUrGrCrCrCrUrUrGrGrCrArGrCrArCrU(/5AmMC6/rArGrUrGrArUrArCrCrArGrCrArUrCrG
rUrCrUrUrGrArUrGrCrCrCrUrUrGrGrCrArGrCArCr rU from IDT).

2.2.3 Preparation of plant extract

Arabidopsis leaves were ground into fine powder in liquid nitrogen using a mortar and pestle. One gram of the sample was then transferred into a 15-mL tube, mixed with 10 mL cold extraction buffer (methanol : water : acetic acid, 80 : 19 : 1, v/v/v), kept on ice for 1 h with occasional shaking, then centrifuged at 4000 rpm (Sorvall ST 40R, Thermo Fisher Scientific) for 15 min at 4 °C. The supernatant was filtered using a syringe-facilitated filter with a pore size of

0.2 μm . This plant extract was then supplemented with theophylline to the required concentration.

2.2.4 Surface functionalization and biodetection procedure

The Au-coated sensor surface was functionalized with theophylline aptamer using 1-ethyl-3-(3-dimethylaminopropyl) carbodiimide (EDC)/N-hydroxysulfosuccinimide (NHS) chemistry, as shown in Fig. 2.2a. More specifically, the Au-coated sensor surface was immersed in the 0.1 mM HSC10COOH/HSC8OH solution for 30 min then washed with ethanol. After the surface had dried, the surface was immersed in a solution of NHS and EDC (NHS 0.2 M, EDC 0.05 M) for 30 min, then washed with PBS buffer and immersed in the 1 μM aptamer solution overnight. This was followed by loading of 100 μL 1 M ethanolamine (EA) to block the non-occupied MPA sites activated by the EDC/NHS, then followed by an injection of 100 μL of 100 mM phosphoric acid (PPA) to remove the non-specific binding. Finally, the sensor surface was rinsed with PBS buffer to flush off non-specifically adsorbed proteins. At this stage, the sensor was ready for the measurement.

2.2.5 Instrumentation

Fig. 2.2b shows that the detection setup of the nanopore-based sensors was the same as those previously reported (He et al., 2014; Zhang et al., 2011). Specifically, a broadband light source from a tungsten halogen lamp was coupled to a specifically-designed optical fiber probe

(Ocean Optics, Inc., Dunedin, FL, USA) that illuminates the sensor surface perpendicularly. The reflected signals (transducing signals) are collected using the same optical fiber probe that leads to an optical spectrometer (Ocean Optics, Inc.) that detects optical spectra from 350 nm to 1050 nm. The spectrometer was connected to a laptop computer for data acquisition and processing. The biochemical samples are transported to the chip through the assembled plastic tubes (Upchurch Scientific, Inc.) by a pump-controlled syringe (Harvard Apparatus, MA, USA).

2.2.6 Experimental data acquisition

The average fringe shifts for the measured transducing signals were obtained by (i) first obtaining the shift of each fringe peak relative to that of the blank Au-coated AAO surface or the shift after the aptamer has been immobilized on the AAO surface, and (ii) averaging the shift of all the peaks to obtain error bars for the measurements. The reference for each average shift is specified in context in the following sections. The transducing signal of the same sample was measured on at least four sensors to obtain an average value.

2.2.7 Detection procedure

Theophylline in PBS buffer, caffeine solution, theobromine solution, plant extracts and Newborn Calf Serum, respectively, has been detected. As previously mentioned, prior to the introduction of a sample into a sensor, 100 μ L 1 M ethanolamine (EA) is loaded to block the non-occupied MPA sites activated by the EDC/NHS, followed by an injection of 100 μ L of 100

mM phosphoric acid (PPA) to remove the non-specific binding. The sensor surface is finally rinsed with the PBS buffer to flush off non-specifically adsorbed proteins, after which theophylline (in the buffer, caffeine solution, theobromine solution, plant extracts, or serum) will be applied to the sensors, and after final sequential washes, readings will be taken. All assay parameters, including theophylline concentrations and incubation times, are optimized to obtain high sensitivity and high signal-to-noise ratio. Experiments for negative controls were carried out to again employ the full assay procedure but without the theophylline.

2.3. Results and discussion

2.3.1 Detection of theophylline in buffer solution & evaluation of the binding kinetics between aptamer and theophylline

Fig. 2c shows typical optical transducing signals (interference fringe shifts) from two sensors (SENSOR1: nanopore size is ~10 nm; SENSOR2: nanopore size is ~50 nm) before and after applying theophylline (TP) at different concentrations (Song, et al., 2017). In this case, the theophylline is in the PBS buffer. The optical interference fringes exhibit a clear shift and, as expected, the higher the concentration of the theophylline, the larger the fringe shift. Note that no further shift can be observed once the binding sites of the aptamer have been totally occupied by theophylline, similar to the behavior of an antibody-based sensor (Zhang, et al., 2012). To test reproducibility of the sensors, assays were performed on four sensors and run under the same conditions on different days. It was found that the concentrations of the theophylline of 0.05 μ M

and 0.2 μM could be easily detected by SENSOR2 and SENSOR1 (Fig. 2.3a), respectively, indicating that the limit of detection (LOD) of the nanopore sensors could be optimized, for example, by varying nanopore size. The concentration of 0.05 μM detected by SENSOR2 is comparable to the LOD recently reported by other research labs (Jiang, et al., 2015; Ng, et al., 2017), and much improved over the LOD from equipment such as liquid chromatography (Ellington and Szostak, 1990; Rankin, et al., 2006; Srdjenovic, et al., 2008). Note that the LOD of the sensor can be further improved by systematically modifying nanopore size and density (Lee, et al., 2015). While it is anticipated that as low as pM or even fM concentrations of theophylline can be detected based on our previous work for detecting disease biomarkers (Alzghoul, et al., 2016; Zhang, et al., 2012), it should be noted that since the clinical relevant concentration range of theophylline ranges from 20 μM to 100 μM , and only at higher concentrations does TP becomes toxic, lethal, or leads to permanent neurological damage (Dawson and Whyte, 1999), it is not critically important to push the LOD of the sensor much lower than this range. In the following experiments, unless otherwise specifically mentioned, all measurements have been carried out by SENSOR1 only.

As shown, the detection dynamic range of theophylline has been demonstrated from 0.05 to 48 μM (Fig. 2.3a) for SENSOR2, significantly larger than the 0.3–2 μM dynamic range of fluorescent assays (Rankin, et al., 2006) and the 0.2–10 μM dynamic range of electrochemical

sensors (Ferapontova, et al., 2008). It is anticipated that the dynamic range can be further improved by optimizing the surface functionalization process to increase the available binding sites provided by the aptamer, making them similar to those binding sites provided by the antibody (Zhang, et al., 2012).

To determine the rate of binding reaction between the aptamer and theophylline, the binding kinetics were evaluated using SENSOR1, and it was found that, similar to previous reports (Ferapontova, et al., 2008), the final signal (meaning the shift of the optical transducing signal remained unchanged either because all available sites from aptamer were occupied by the added theophylline or because the establishment of binding equilibrium between aptamer and theophylline) is reached faster for theophylline added at a lower concentration than at a higher concentration. This is because a longer time is required for higher concentrations of theophylline to be diffused to the binding sites, thereby establishing binding equilibrium. On the other hand, the diffusion time of theophylline to the binding sites can also be reduced by stirring the theophylline (Zubtsov, et al., 2006). Two representative results are shown in Fig. 2.3b, showing that when the concentration of theophylline is 40 μM , it takes ~ 60 min to obtain the final signal if the sensor is kept stationar, while it takes only 15 min to reach the final signal if the sensor is put on a lab shaker (Magnetic stirrer, Thermo Fisher Scientific, Inc.) because the diffusion speed of the theophylline to the aptamer is significantly enhanced.

2.3.2 Assessment of influence of RNase inhibitor on the assay

Since theophylline aptamer is RNA-based, stability can be an issue due to widespread RNase in the environment. RNase inhibitors can be used to inactivate RNase, thereby prolonging the shelf life of RNA-based aptamers. The effect of SUPERase In RNase Inhibitor on the assay and consequently on the transducing signals was evaluated. In those experiments, theophylline was dissolved in 0.1 M pH7.2 PBS with 5 mM KCl and 1 mM MgCl₂ with SUPERase•In RNase Inhibitor (a concentration of 120 U/mL). In this way, a series of theophylline samples with respective concentrations of 0 μ M, 4 μ M, 20 μ M and 40 μ M are prepared. As shown in Fig. 2.4a, compared to the samples without adding the SUPERase•In RNase Inhibitor, the transducing signals of the samples with SUPERase•In RNase Inhibitor did exhibit some changes, and differences in transducing signals (samples with and without adding the inhibitor) also change with the theophylline concentrations. In another series of experiments, aptamer-functionalized chips were preserved in solutions containing RNase inhibitor for up to 7 days then washed using abuffer before the theophylline measurements, and it was found that the transducing signal differences between sensors preserved in the solutions with RNase inhibitor for 7 days (the inhibitor has been washed before the measurements) and sensors without adding RNase inhibitor were much smaller (Fig. 2.4a), confirming that SUPERase•In RNase Inhibitor can be potentially used for extending the lifetime of aptamer-based sensors.

2.3.3 Determination of sensor regeneration rate/capability

The regeneration capability of the aptamer sensors was evaluated by carrying out two types of experiments. (1) Type I Experiment: After detecting four different concentrations (0 μM , 4 μM , 20 μM and 40 μM) of theophylline using 4 groups of sensors (each group had four sensors: Group 1 for detecting 0 μM only, Group 2 for detecting 4 μM only, group 3 for detecting 20 μM only, group 4 for detecting 40 μM only), respectively. A vigorous wash of the sensors in 4 groups with buffer (0.1 M pH7.2 PBS with 5 mM KCl and 1 mM MgCl_2) was carried out to release the theophylline from the aptamer, after which the sensors were stored in the fresh buffer at 4 $^{\circ}\text{C}$ in an incubator overnight. 24 h later, the same concentrations of theophylline were applied on these recovered sensors in 4 groups (again Group 1 for detecting 0 μM only, Group 2 for detecting 4 μM only, group 3 for detecting 20 μM only, group 4 for detecting 40 μM only), respectively, and resulting transducing signals were measured. Fig. 2.4b is a plot of signal changes before and after regeneration in 4 groups. The typical change in transducing signals was small ($\sim 15\%$), indicating reasonably good regeneration capability of the aptamer sensor. (2) Type II Experiment: To further evaluate whether the regenerated sensors could be reused for monitoring theophylline, the following experiments were designed. First, 4 groups of sensors were used to detect theophylline at concentrations of 0 μM , 4 μM , 20 μM and 40 μM (each group has four sensors: Group 1 for detecting 0 μM only, Group 2 for detecting 4

μM only, group 3 for detecting 20 μM only, group 4 for detecting 40 μM only), respectively.

Second, all the sensors were then regenerated, i.e., they were rinsed vigorously in the buffer to allow theophylline to be released from aptamer, then stored overnight in fresh buffer.

Third, all sensors from Group 1 to Group 4 were used to detect theophylline at a series of concentrations, 0 μM , 4 μM , 20 μM and 40 μM , respectively, with results plotted in Fig. 2.4c. As shown, the optical responses of all sensors from the 4 groups increased with the increased concentrations of theophylline, and the measured responses exhibited changes of 15–20% compared to those before sensor regeneration, consistent with those reported by another research group (Ferapontova, et al., 2008).

2.3.4 Detection of theophylline in caffeine and theobromine

The structure of theophylline is closely related to caffeine and theobromine (TB), that have been routinely used to test specificity of theophylline sensors. In our experiments, the specificity of the sensor was evaluated by measuring theophylline in caffeine and theobromine samples (Fig. 2.5a). The shift of the optical signal was ~ 0.25 nm when only theobromine was applied, but the shift increases when theophylline is spiked into a theobromine solution, and becomes much more pronounced, about ~ 3.07 nm, when 40 μM theophylline is added to TB solution. Similar results were obtained for caffeine, with the shift a little larger (~ 0.40 nm) when only caffeine is applied, indicating that the non-specific binding/affinity with theophylline-

aptamer increases for caffeine compared to that with TB. Again, the shift increases when theophylline is added to caffeine and becomes ~ 2.7 nm when 40 μ M theophylline is added. Both experiments suggest the good specificity of an aptamer-based assay. Even though there is a small shift for pure TB samples and pure caffeine samples, small non-specific binding for both samples do exist. To mitigate non-specific binding effects on the measurements, a reference sensor was used to obtain the shift of the optical signal when only TB or only caffeine is applied, with the shift due to theophylline then obtained by subtracting the shift of the reference sensor from the measurements of the theophylline in these two solutions, respectively. The optical signals for theophylline after calibration (subtracting the optical signals from the reference sensor) in caffeine and theobromine are given in Fig. 2.5b. Statistically, the measured signals for theophylline at the same concentration as TB is a little larger than those of theophylline in caffeine, again suggesting that TB has larger specific binding/affinity with aptamer than caffeine. All these experiments indicate that the aptamer sensors of this type have good specificity, and that theophylline spiked in chemicals with structures similar to theophylline can be distinctly monitored.

2.3.5 Detection of theophylline in plant extracts and serum samples

To evaluate the feasibility of sensor detection of theophylline in plant and clinical samples, measurements of theophylline dissolved in plant extract and in serum were carried out.

As shown in Fig. 2.6a, while some level of non-specific binding between aptamer and plant extract exists, the transducing signals show a clearly increased shift with increased concentrations of theophylline spiked in the plant extract, and calibrated measurement indicates that the sensor can successfully detect theophylline in plant extract. Furthermore, for the same concentration of theophylline spiked in caffeine, theobromine, and plant extract, the shifts in optical signals are similar. For example, the optical signal shift was ~ 2.3 nm for 40 μM theophylline in caffeine, ~ 2.8 nm for 40 μM theophylline in theobromine, and ~ 2.5 nm for 40 μM theophylline in plant extracts, respectively. While the different media (caffeine, theobromine, and plant extract) do produce different levels of non-specific binding, the measured signals for theophylline at the same concentration in different media are statistically reasonably consistent. These results indicate the good specificity of the aptamer-based sensor.

Finally, measurements of theophylline dissolved in Newborn Calf Serum were carried out, and it was found that biofouling of the serum on the sensor's surface was significant if the serum was not diluted. As a result, the non-specific binding on the sensing surface was very large. To mitigate this issue, the serum was diluted by $20 \times$ before it was spiked with theophylline. As shown in Fig. 2.6b, some levels of non-specific binding between aptamer with serum clearly exists, and even after calibration the optical signals at the same concentration of

theophylline in serum are consistently larger than those of theophylline in TB, caffeine, and plant extracts, given the increased biofouling of the serum on the sensor surfaces. Nevertheless, the calibrated measurement indicates the sensor can successfully detect theophylline in diluted serum.

2.4. Conclusions

An aptamer-based nanopore thin film sensor for detecting theophylline in buffer and complex fluids has been reported. Aptamer-based detection offers many advantages over antibody-based detection, such as low cost and high stability at elevated temperatures. It was found that theophylline in the buffer at a concentration as low as 0.05 μM , significantly lower than the limit of detection of current lab-based equipment such as liquid chromatography (LC), can be readily detected by this type of sensor. The kinetic dynamics of the binding between the aptamer and theophylline was also evaluated, and it was found that final transducing signals can be obtained within 15 min for a theophylline concentration of up to 40 μM . Considering regenerated sensors, they show reasonable consistency with fresh sensors for measuring theophylline at different concentrations. It was also found that the aptamer-based sensor exhibited good specificity and selectivity by detecting theophylline in caffeine and theobromine that are structurally similar to theophylline. If reference sensors are used, the non-specific binding effect can be further mitigated. This type of sensor also shows good repeatability. In

summary, theophylline in plant extract and serum has been successfully detected, strongly suggesting the feasibility that an aptamer sensor of this type can detect theophylline in both plant samples and clinical samples.

References

- Alzghoul, S., Hailat, M., Zivanovic, S., Que, L., Shah, G.V., 2016. Measurement of serum prostate cancer markers using a nanopore thin film based optofluidic chip. *Biosens. Bioelectron.* 77, 491–498.
- Barnes, P., Pauwels, R., 1994. Theophylline in the management of asthma: time for re-appraisal? *Eur. Respir. J.* 7, 579–591.
- Cook, C., Twine, M., Myers, M., Amerson, E., Kepler, J., Taylor, G., 1976. Theophylline radioimmunoassay: synthesis of antigen and characterization of antiserum. *Res. Commun. Chem. Pathol. Pharmacol.* 13, 497–505.
- Dawson, A.H., Whyte, I.M., 1999. Therapeutic drug monitoring in drug overdose. *Br. J. Clin. Pharmacol.* 48, 278–283.
- Ellington, A.D., Szostak, J.W., 1990. In vitro selection of RNA molecules that bind specific ligands. *Nature* 346, 818–822.
- Ferapontova, E.E., Olsen, E.M., Gothelf, K.V., 2008. An RNA aptamer-based electro- chemical biosensor for detection of theophylline in serum. *J. Am. Chem. Soc.* 130, 4256–4258.
- Ferapontova, E.E., Shipovskov, S., Gorton, L., 2007. Bioelectrocatalytic detection of theophylline at theophylline oxidase electrodes. *Biosens. Bioelectron.* 22, 2508–2515.
- He, Y., Li, X., Que, L., 2014. A transparent nanostructured optical biosensor. *J. Biomed. Nanotechnol.* 10, 767–774.

- Jiang, H., Ling, K., Tao, X., Zhang, Q., 2015. Theophylline detection in serum using a self-assembling RNA aptamer-based gold nanoparticle sensor. *Biosens. Bioelectron.* 70, 299–303.
- Jolley, M., 1981. Fluorescence polarization immunoassay for the determination of therapeutic drug levels in human plasma. *J. Anal. Toxicol.* 5, 236–240.
- Lee, J.-S., Kim, S.-W., Jang, E.-Y., Kang, B.-H., Lee, S.-W., Sai-Anand, G., Lee, S.-H., Kwon, D.-H., Kang, S.-W., 2015. Rapid and sensitive detection of lung cancer biomarker using nanoporous biosensor based on localized surface plasmon resonance coupled with interferometry. *J. Nanomater.* 2015, 1.
- Ng, S.P., Qiu, G., Ding, N., Lu, X., Wu, C.-M.L., 2017. Label-free detection of 3-nitro-L-tyrosine with nickel-doped graphene localized surface plasmon resonance biosensor. *Biosens. Bioelectron.* 89, 468–476.
- Rankin, C., Fuller, E., Hamor, K., Gabarra, S., Shields, T., 2006. A simple fluorescent biosensor for theophylline based on its RNA aptamer. *Nucleosides Nucleotides Nucleic Acids* 25, 1407–1424.
- Song, C., Che, X., Que, L., 2017. Nanopore thin film enabled optical platform for drug loading and release. *Opt. Express* 25, 19391–19397.
- Song, K.-M., Lee, S., Ban, C., 2012. Aptamers and their biological applications. *Sensors* 12, 612–631.
- Srdjenovic, B., Djordjevic-Milic, V., Grujic, N., Injac, R., Lepojevic, Z., 2008. Simultaneous HPLC determination of caffeine, theobromine, and theophylline in food, drinks, and herbal products. *J. Chromatogr. Sci.* 46, 144–149.
- Ulyanova, Y.V., Blackwell, A.E., Minter, S.D., 2006. Poly (methylene green) employed as molecularly imprinted polymer matrix for electrochemical sensing. *Analyst* 131, 257–261.
- Wang, T., Randviir, E.P., Banks, C.E., 2014. Detection of theophylline utilising portable electrochemical sensors. *Analyst* 139, 2000–2003.
- Yin, H., Li, X., Que, L., 2014. Fabrication and characterization of aluminum oxide thin film micropatterns on the glass substrate. *Microelectron. Eng.* 128, 66–70.

Zhang, T., Gong, Z., Giorno, R., Que, L., 2010. A nanostructured Fabry-Perot interferometer. *Opt. Express* 18, 20282–20288.

Zhang, T., He, Y., Wei, J., Que, L., 2012. Nanostructured optical microchips for cancer biomarker detection. *Biosens. Bioelectron.* 38, 382–388.

Zhang, T., Pathak, P., Karandikar, S., Giorno, R., Que, L., 2011. A polymer nanostructured Fabry-Perot interferometer based biosensor. *Biosens. Bioelectron.* 30, 128–132.

Zubtsov, D., Ivanov, S., Rubina, A.Y., Dementieva, E., Chechetkin, V., Zasedatelev, A., 2006. Effect of mixing on reaction-diffusion kinetics for protein hydrogel-based microchips. *J. Biotechnol.* 122, 16–27.

Figures

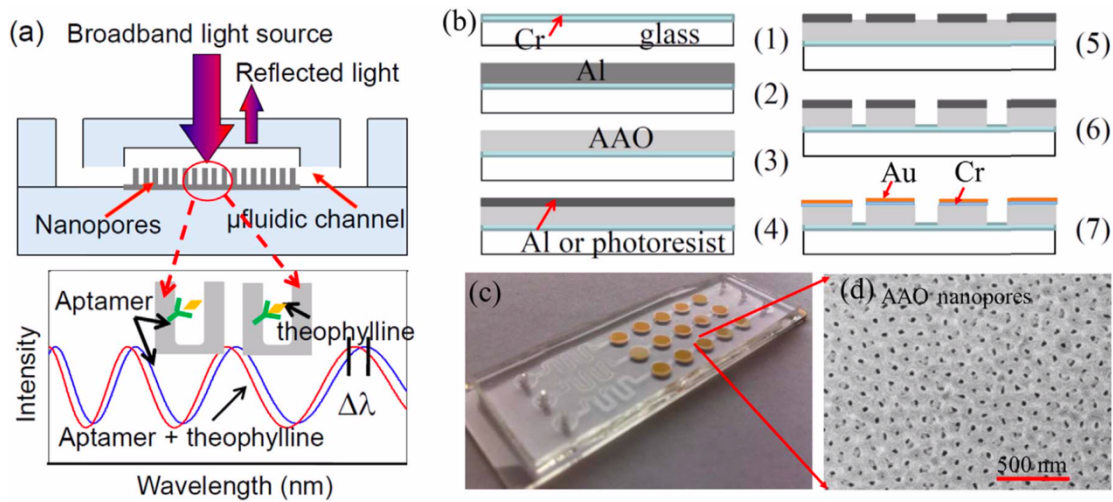


Figure 2. 1 (a) Sketch showing a nanopore-based aptamer sensor and its operational principle; (b) process flow to fabricate the nanopore-based sensors; (c) a photo of a chip consisting of 15 AAO nanopore-based sensors with a microfluidic interface; (d) SEM image

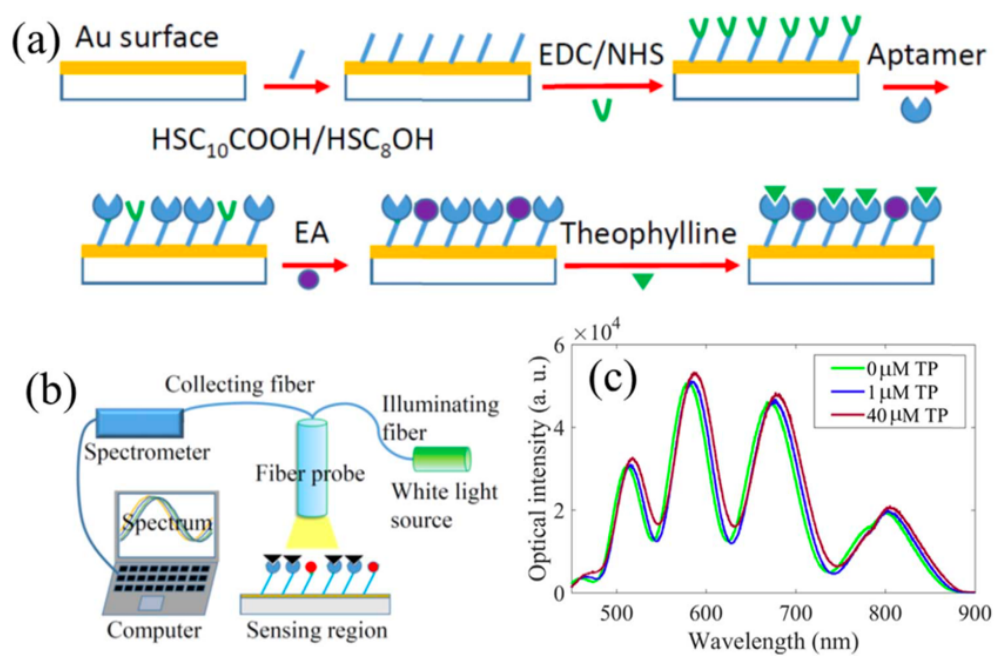


Figure 2. 2 (a) Illustration of surface functionalization process of the sensor; (b) the setup for the optical measurements; (c) representative measured optical signals for theophylline at different concentration

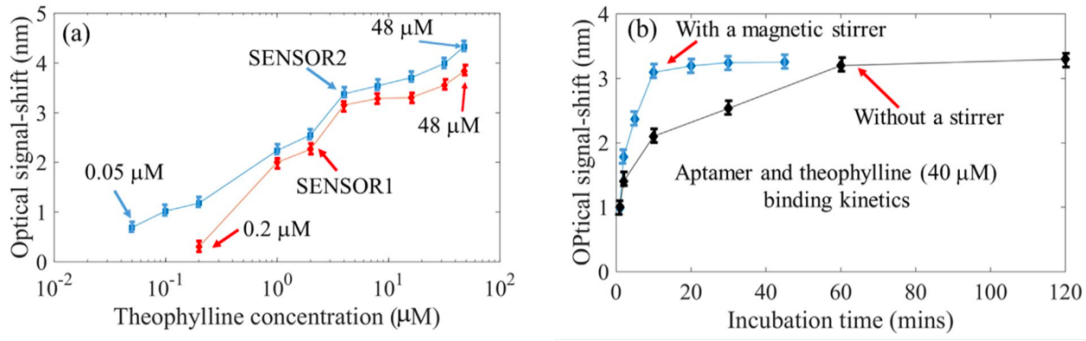


Figure 2. 3 (a) Measured shift of optical signals of theophylline under a series of concentrations using SENSOR1 and SENSOR2; (b) measured binding kinetics of theophylline with aptamer at a concentration of 40 μM

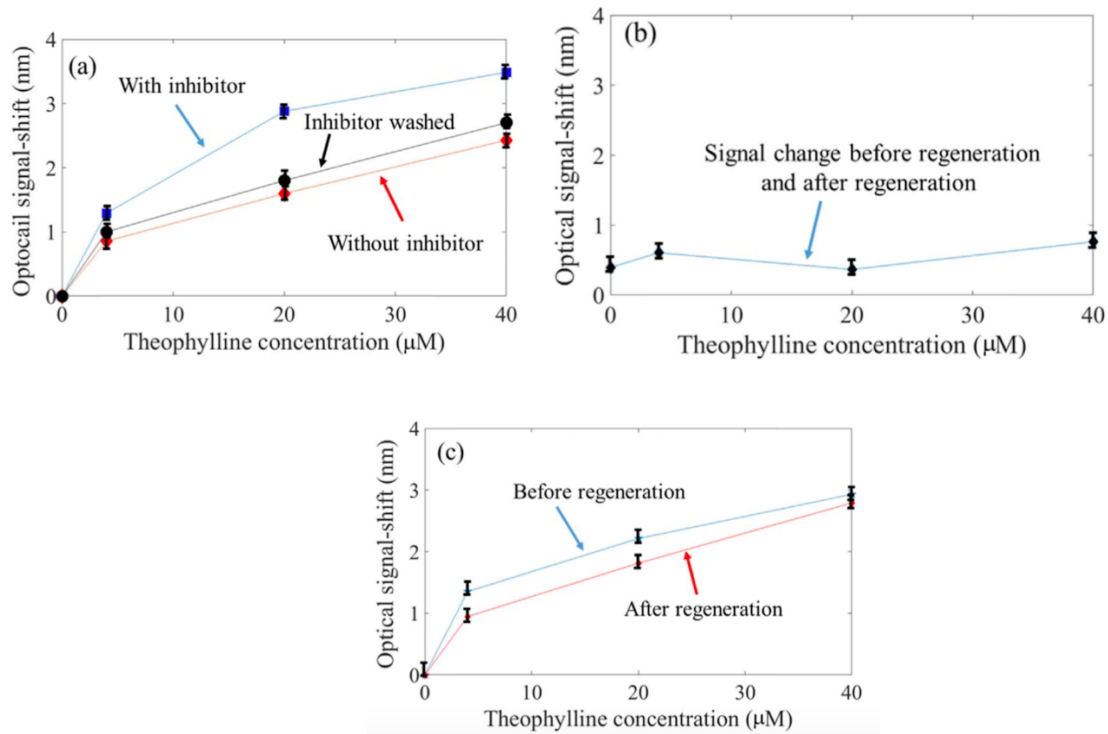


Figure 2. 4 (a) Comparison of transducing signals from the sensors with applied inhibitor, after washing the inhibitor, and without applied inhibitor in the assay; (b) the difference of the transducing signals between the fresh sensors and the regenerated sensors;

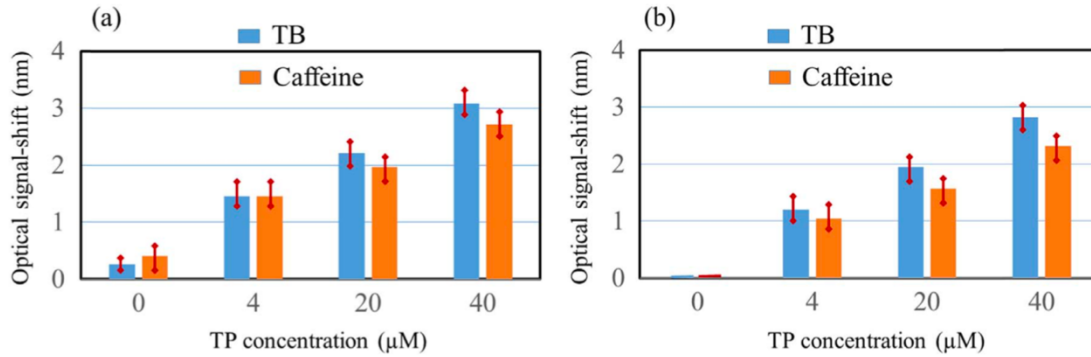


Figure 2. 5 (a) Measured transducing signals of theophylline spiked in TB and caffeine; (b) the transducing signals after subtracting the signals from the reference's sensors.

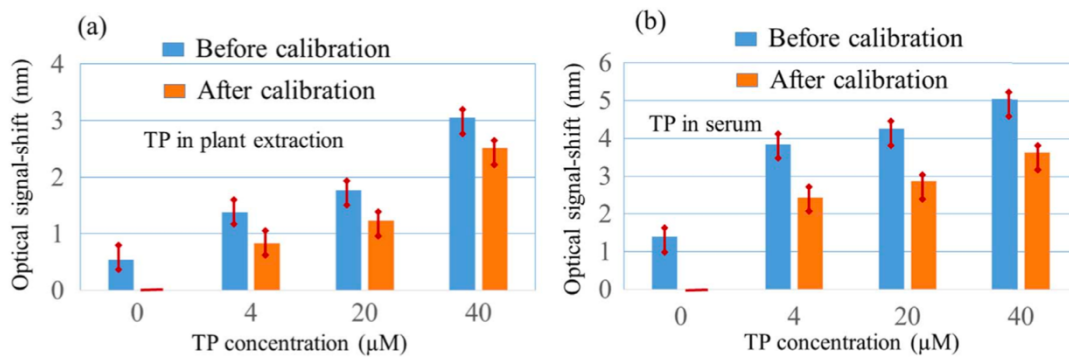


Figure 2. 6 (a) Measured transducing signals of theophylline spiked in plant extracts; (b) measured transducing signals of theophylline spiked in serum.

CHAPTER 3. DEVELOPMENT OF A STRUCTURE-SWITCHING APTAMER-BASED NANOSENSOR FOR SALICYLIC ACID DETECTION

Abstract

Salicylic acid (SA) is a phytohormone for regulating immune responses against pathogens, and SA and its derivatives can be found in diverse food products, medicines, cosmetics, and preservatives. While salicylates have potential disease-preventative activity, they can also cause health problems for hypersensitive people. Because current SA detection methods are costly, labor-intensive and require bulky instruments, this study developed a structure-switching aptamer-based nanopore thin film sensor for cost-effective, rapid, sensitive, and simple detection of SA in both buffer and plant extracts. SA is a challenging target for aptamer selection using conventional systemic evolution of ligands by exponential enrichment (SELEX) because of its small size and scarcity of reactive groups for immobilization. By immobilizing the SELEX library rather SA and screening the library using a structure-switching SELEX approach, a high-affinity SA aptamer was identified. The nanopore thin film sensor platform can detect SA levels as low as 0.1 μM , much better than the sensitivity of antibody-based detection methods. This nanosensor also exhibited good selectivity among SA and its common metabolites and could detect SA in *Arabidopsis* and rice using only about 1 μl of plant extracts within less than 30 min.

Detection of SA with a nanopore thin-film sensor provides a promising solution for low-cost, rapid, sensitive on-site detection of SA.

Key words: Aptamer-based biosensing; structure-switching SELEX; nanopore thin film sensor; salicylic acid detection; plant extract.

3.1 Introduction

The plant hormone salicylic acid (SA) regulates diverse physiological processes, including thermogenesis, flowering, germination, pathogen resistance, and circadian clock function (Cleland and Ajami, 1974; Raskin, et al., 1987; Rhoads and McIntosh, 1992; Shakirova, et al., 2003; White, 1979; Zhou, et al., 2015). As a major defense hormone, exogenous SA treatment enhances resistance to biotrophic pathogens (White, 1979) and mutants with elevated endogenous SA levels are usually more resistant to biotrophic pathogens (Bowling, et al., 1994; Clarke, et al., 1998; Zhang, et al., 2003), so quantification of SA is a routine in plant immunity research.

In addition to its effect on plant health, SA and its derivative, aspirin (acetylsalicylic acid) also have had a profound impact on human health. Aspirin can lower the risk of death from oesophagus, colorectal, and lung cancer, protect against cardiovascular disease, and may prevent pre-eclampsia (Kim, et al., 2014; Oyola and Kirley, 2015; Rothwell, et al., 2011; Voelker, 2014).

However, use of aspirin can also result in urticaria, angioedema, rhinitis, and asthma in hypersensitive people (Kowalski, et al., 2013). In addition to medicinal sources, dietary intake of SA is also considerable because SA occurs naturally in various fruits, vegetables, beverages, herbs and spices (Szkop, et al., 2017). Indeed, SA has been detected in serum and urine of people who do not take aspirin (Shaukat, et al., 2011) and the SA urine level of vegetarians not taking aspirin is comparable to patients taking 75 mg aspirins (Lawrence, et al., 2003). Since it is very likely that SA from dietary sources may provide humans with similar beneficial and adverse effects as aspirin, the amount of SA from medicinal, dietary and cosmetic sources should frequently be determined to ensure health of people with different SA sensitivities. There is therefore an increasing need for a low-cost, fast, sensitive, and simple method for routine and on-site SA detection, and this critical need for SA quantification has resulted in the development of various SA detection methods. SA is routinely quantified by chromatography-based methods like high-performance liquid chromatography (HPLC) (Venema, et al., 1996). While mass spectrometry (MS) or tandem MS-coupled chromatography-based methods have also been developed for simultaneous quantification of multiple plant hormones, including SA (Balcke, et al., 2012; Du, et al., 2012; Engelberth, et al., 2003; Li, et al., 2011; Pan, et al., 2010; Segarra, et al., 2006), these methods are labor-intensive, consume considerable amounts of solvent, and require bulky instruments for chromatographic separation and UV or fluorescence detection.

Capillary electrophoresis (CE) has been tested as an alternative to HPLC-based methods because of its faster speed, simpler sample preparation and lower cost (Chang, et al., 2017; Chen, et al., 2014), but CE uses extremely high voltage (well over 10 kV) for electrophoresis and this may raise operator safety concerns. An *Acinetobacter* sp. ADPWH_ *lux* strain containing a SA-inducible operon was developed as an SA biosensor (Huang, et al. 2005, 2006), but its use was time-consuming and labor-intensive. *In situ* detection of SA has been accomplished using reverse iontophoresis (Gonzalez-Sanchez, et al., 2015) and TiO₂ nanoparticles (Tseng, et al., 2014), but the low sensitivity of those methods makes them unreliable for quantification. Using SA antibodies, enzyme-linked immunosorbent assays (ELISAs) have been used to quantify SA (Wang, et al. 2001, 2002), but the cross-reactivity of the antibody causes these assays to suffer from limited specificity and accuracy.

Aptamers have emerged as an attractive replacement for antibodies. Compared to antibodies that are expensive and notorious for their lack of reproducibility between lots, aptamers have several advantages such as low cost and higher uniformity because of their synthetic nature (Bradbury and Pluckthun, 2015). Aptamers tolerate a wide range of pH and salt concentrations and can be easily modified for compatibility with diverse detection platforms. Importantly, aptamers are more stable at elevated temperature, and thermal denaturation is reversible, making them ideal for on-site or even field application.

In this study, we developed an aptamer-based label-free SA nanosensor using a structure-switching SELEX strategy. The identified SA aptamer was incorporated into a nanostructured Fabry-Perot interference (nanoFPI) sensor previously developed by our team (Feng, et al., 2018; Song, et al., 2017). Interference fringes of white light reflected from the nanoFPI sensor are used as transducing signals for SA quantification.

3.2 Materials and methods

3.2.1 Chemicals and materials

11-Mercaptoundecanoic acid (HSC₁₀COOH, 99%), 8-Mercapto-1-Octanol (HSC₈OH, 98%), N-(3-Dimethylaminopropyl)-N'-ethylcarbodiimide hydrochloride (EDC), N-Hydroxysuccinimide (NHS), ethanolamine (EA), salicylic acid, and 4-hydroxybenzoic acid (4-HBA) were purchased from Sigma. Phosphoric acid (PPA), ethyl acetate, cyclopentane, methyl salicylate, and streptavidin magnetic beads were purchased from Fisher. Benzoic acid was purchased from VWR. Salicylic acid 2-O- β -D-glucoside was purchased from Toronto Research Chemicals. Lambda enzyme was purchased from Lucigen. The initial SELEX library, probes, primers, and SA aptamer candidates were purchased from IDT and Bio Basic.

3.2.2 Structure-switching SELEX

200 μ l of magnetic beads were resuspended with capture probes (50 μ M) dissolved in 200 μ l binding buffer (50 mM Tris, 137 mM NaCl, 5 mM MgCl₂, pH 7.4) to immobilize the probes

onto the beads. 100 μ l of snap-cooled DNA was incubated with beads for 30 min with gentle agitation using the thermomixer at 25 °C. The beads were then washed three times using binding buffer, re-suspended in binding buffer containing 200 μ l SA, and agitated on the thermomixer for 30 min. The supernatant was amplified using PCR with 5'-phosphorylated reverse primer according to the following program.

95°C	2 min	
95°C	30 s	} n Cycles
55°C	30 s	
72°C	30 s	
72°C	5 min	

The optimal cycle number of the PCR was first determined through a small-scale trial based on the criteria that the optimal PCR cycle produces the most abundant products with the correct size and without unwanted by-products. Asymmetric PCR was then performed to further enrich the target sequences using the following program.

95°C	2 min	
95°C	30 s	} M cycles
55°C	30 s	
72°C	1 min	
72°C	5 min	

Similarly, the optimal PCR cycle number was first determined through a small-scale trial based on the criteria that the optimal PCR cycle produces the most abundant products

with the correct size and without unwanted by-products. The PCR products were treated with lambda enzyme, then cleaned and concentrated with ssDNA/RNA Clean and Concentrator (Zymo Research), and the concentrated ssDNA was used for the next round of SELEX. Beginning with the fourth round, a negative selection was performed before a positive selection using 200 μ l 4- HBA. The enrichment of the screening process was confirmed and candidate aptamers were revealed by HiSeq. The sequences of the initial SELEX library, probes, and primers used for SELEX and subsequent HiSeq library generation and sequencing are listed below.

3.2.3 Fabrication of the nanopore thin film-based sensor

The sketch and operational principles of the nanoFPI sensor are depicted in Fig. S3.1a. The nanoFPI sensor is comprised of a layer of Au-coated nanopore thin film embedded in its FPI cavity (Zhang, et al., 2010), and reflected optical signals (interference fringes) from the nanoFPI sensor were used as transducing signals. When the effective refractive index and the effective thickness of the nanopore thin film inside the FPI cavity change due to the aptamer and SA coating, the reflected interference fringes shift. The sensor was fabricated using the process flow illustrated in Fig. S3.1b (Yin, et al., 2014). A 10 nm Cr was briefly deposited on a rigorously-cleaned cover-slip glass substrate, followed by depositing 2–3 μ m thick Al (99.999%) by E-beam evaporation. A two-step anodization process was then carried out, resulting in a layer of anodic

aluminium oxide (AAO) nanopore thin film on the glass substrate. A 150 nm Al layer was then deposited on the AAO nanopore thin film, followed by a photolithography and wet etching process to fabricate AAO nanopore thin-film patterns using the Al layer as a mask, after which the Al was etched away. An AAO-glass chip was then fabricated after depositing a layer of 10 nm Au on the surface of the AAO nanopore thin film along with a layer of Cr (5 Å) as an adhesion layer. A polydimethylsiloxane (PDMS) microfluidic chip was then separately fabricated using a soft lithography process, after which it was bonded with the AAO- glass chip after 2-min oxygen plasma treatment of the combined AAO-glass chip and PDMS microfluidic chip, followed by assembling input and output plastic tubes. A photo of the sensor chip comprised of arrayed nanoFPI sensors is shown in Fig. S3.1c, and representative SEM image of the fabricated AAO nanopore thin film is shown in Fig. S3.1d.

3.2.4 Surface functionalization

The Au-coated sensor surface was functionalized with SA aptamers through 1-ethyl-3-(3-dimethylaminopropyl) carbodiimide (EDC)/N- hydroxysulfosuccinimide (NHS) chemistry as shown in Fig. S2. Specifically, the sensor surface was immersed in a 0.1mM (1:9) HSC10COOH/HSC8OH solution for 30min then washed with ethanol. After the surface dried, it was immersed in a solution of NHS and EDC (NHS 0.2M, EDC 0.05M) for 30 min, after which it was washed with PBS buffer then immersed in a 5μM aptamer solution overnight. This was

followed by loading of 100 μ l 1 M ethanolamine (EA) to block non-occupied sites activated by the EDC/NHS. Finally, the sensor surface was rinsed with SELEX binding buffer to flush off non-specifically adsorbed proteins, after which the sensor is ready for measurement. Sequences of SA aptamer candidates used for functionalization are listed below.

3.2.5 Detection procedure

After the sensor surfaces were functionalized with SA aptamers, a series of SA concentrations in the SELEX binding buffer and plant extracts and a series of concentrations of 4-HBA, MeSA, SAG, and BA were applied to the sensors, followed by a 30-min incubation. Readings were then taken after several sequential washes. All assay parameters, including concentrations of the SA and incubation times, were optimized to achieve high sensitivity and high signal-to-noise ratio. Experiments for negative controls were carried out by going through the full assay procedure but without SA, 4-HBA, MeSA, SAG, or BA.

3.2.6 SA extraction from plants

Arabidopsis leaves or rice aerial parts were ground to fine powder in liquid nitrogen using a mortar and pestle, and 8 g of this powder was transferred to a 50-ml falcon tube, mixed with 28 ml 90% methanol, vortexed, and sonicated for 16 min. The supernatant was collected after centrifugation at 20,800 g for 5 min, with 2 ml of 0.2 M NaOH added to the supernatant. The combined supernatant was then dried overnight in a speed-vac at room temperature (RT),

after which the residue was re-suspended in 20 ml of 5% trichloroacetic acid and sonicated for another 16 min. The sample was next centrifuged at 20,800 g for 5 min and the supernatant was collected. This sample was extracted twice by adding 20 ml of ethyl acetate-cyclopentane (1:1), vortexed, sonicated for 16 min, and centrifuged at 20,800 g for 1 min. The organic phase was combined and dried in a speed-vac RT, and the dried extract was dissolved in 16 ml of SELEX binding buffer. The supernatant was then filtered using a syringe-facilitated filter of pore size 0.2 μm , and the resulting plant extract was supplemented both with and without SA to the concentrations needed.

3.2.7 Data acquisition and statistical analysis

The average fringe shift for the measured transducing signals from the nanoFPI sensors was obtained by (i) first obtaining the shift of each fringe peak relative to that of the blank Au-coated AAO surface or the shift after the SA aptamer had been immobilized on the AAO surface, then (ii) averaging all the peak shifts. The transducing signal of a particular sample was measured on at least five sensors to obtain the average value. Nonlinear regression was performed to derive a dissociation constant using GraphPad.

3.2.8 Circular dichroism spectroscopy

Circular dichroism spectra of 1 μM SAapt1 in the SELEX binding buffer mixed with buffer control, 40 μM SA, 4-HBA, MeSA, SAG, or BA, were recorded on a Jasco J-710

spectropolarimeter using a Peltier- controlled cell holder designed for standard 1 cm × 1 cm quartz cuvettes. The temperature of the sample holder was set to 25 °C, and the scan was taken from 225 nm to 350 nm at a scanning speed of 100 nm/min with a 1 nm bandwidth.

3.2.9 HPLC analysis

Detection of SA in plant extracts by HPLC was performed according to Halder, et al., (Dhiman, et al., 2015).

3.2.10 GC-MS analysis

C19 was added to the dried samples as an internal standard, and samples and SA standards were resuspended in 90% methanol and dried overnight in GC vial in a speed-vac at room temperature. Silylation of dried samples was performed with BSTFA +1% TCMS (Sigma) at 60 °C for 30 min, and they were then subjected to GC-MS on a 7890C gas chromatograph in tandem with a 5975C MSD under standard conditions using EI ionization. The separation column was an HP5MSI (30 m long, 0.250 mm ID, 0.25 µm film thickness). The oven program was: Initial temperature of 80 °C, followed by, 5 °C/min ramp to 115 °C, then a ramp at 12.5 °C/min to 320 °C, and a final hold for 7 min. The GC was controlled by the Agilent ChemStation software, and identification was performed by comparing the mass spectra to the NIST17 Library using Retention Indices.

3.3 Results and discussion

3.3.1 Structure-switching SELEX

Aptamers can be identified through an *in vitro* evolution technique called *systematic evolution of ligands by exponential enrichment* (SELEX). While the legacy SELEX method can identify aptamers for high-molecular-weight targets with relative ease, small molecules like SA can present great challenges to conventional SELEX because the small molecular size of SA makes size-based partition inefficient and the lack of chemical groups for immobilization makes wash-based separation challenging. To overcome these difficulties, we adopted a structure-switching SELEX strategy (Fig. 3.1a). The ssDNA library was hybridized to a short piece of captured complementary DNA (cDNA) immobilized on magnetic beads. SA binding induces conformational changes of binding sequences and subsequent de-hybridization from the capture cDNA, and the nonbinders remain on the magnetic beads and can be removed. The SA binding sequences were further amplified through asymmetric PCR, during which the complementary strand was phosphorylated at the end of 5'. The complementary strand was then removed using lambda exonuclease, specific to the 5'-phosphorylated strand, while the other strand was used as a library for the next SELEX round. After three rounds of positive selection against SA, and negative selection with increasing concentrations of 4-hydroxybenzoic acid (4- HBA), a structure

analog of SA was incorporated to enhance specificity. The length of the capture probe was increased to 8 and 9 during the round 14 and 15 respectively to increase selection stringency.

Adapter sequences compatible with Illumina HiSeq platform were included in the design of the SELEX library (Fig. 3.1b). The libraries from rounds 6, 13, and 15 were amplified, pooled, and sequenced. The evolution of the relative frequency of the top five aptamer candidates is shown in Fig. 3.2a. The top candidate, SAapta1, has been enriched by more than 5,000-fold between round 6 and round 15, reflecting the effectiveness of such structure-switching SELEX strategy. To identify the best aptamer candidate for further characterization, the top five candidates were functionalized onto the nanoFPI sensor and their binding affinity with SA and 4-HBA was screened (Figs. 3.2b, S3.1, S3.2). Among the five candidates, SAapta1 exhibited the highest affinity and good specificity, so it was selected for further characterization.

3.3.2 Determine of binding affinity of SAapta1 to SA

The dissociation constant (K_d) of SAapta1 was measured using a series of concentrations of SA (Fig. 3.3). Through nonlinear regression and statistical test of different binding models, it was found that the “two sites specific binding” model fit the saturation curve best, with an adjusted R^2 greater than 0.95. The K_d of the low affinity binding site was 4.703 μ M while the K_d of the high-affinity binding site was 34.57 nM, suggesting higher affinity than NPR4, the SA receptor in *Arabidopsis* (Fu et al., 2012).

The same concentration series of 4-HBA were also tested (Fig. 3.3). SAapta1 has limited affinity to 4-HBA, and the optical fringe did not increase with increasing concentration of 4-HBA, so the observed optical fringe induced by 4-HBA represents simply a background signal. This demonstrates the effectiveness of negative selection in the structure-switching SELEX.

3.3.3 Evaluation of binding kinetics of SAapta1

The binding kinetics of SAapta1 were investigated to determine the time taken for the binding reaction to achieve equilibrium (Fig. 3.4). When 40 μM SA was applied, about 30 min was taken for the reaction to reach steady state, while this took only 5 min when 0.2 μM SA was used. The steady state can therefore be achieved faster when a low concentration of SA is applied, a result consistent with previous studies (Feng, et al., 2018; Ferapontova, et al., 2008). It takes more time for a higher concentration of SA to diffuse into the aptamers and reach final equilibrium, so methods like stirring that can accelerate diffusion can shorten the reaction duration (Zubtsov, et al., 2006).

3.3.4 Test of binding sensitivity, specificity, and inter-day variation of SAapta1

To test binding sensitivity, we recorded the non-specific binding using the buffer alone. SA was associated with statistically a more significant optical signal shift than the buffer, even at the lowest concentration assayed (0.1 μM) (Fig. 3.5a). This shows that use of the nanoFPI sensor is significantly more sensitive than an antibody-based method (Wang, et al., 2002) and

comparable to or even better than a bacteria-based biosensor (Huang, et al., 2005, 2006). While the detection limit of this aptamer-based nanosensor can be further and easily enhanced by varying the nanopore size, as we have previously demonstrated for this type of nanoFPI sensor (Feng, et al., 2018), it should be noted that the current detection limit, more than 1 μM , is already sufficient for detection of SA in plants (Defraia, et al., 2008) as well as in human serum (Shaukat, et al., 2011), so improvement of the detection limit is not critical.

In plants, in addition to free SA, most SA is glycosylated to form SA 2- *O*- β -glucoside (SAG) that serves as an inert reservoir of SA (Vlot, et al., 2009). SA can also be methylated to form methyl salicylate (MeSA) that is also biologically inactive (Vlot, et al., 2009). Since both these SA metabolites still contain the SA moiety and were not included in negative selection in the structure-switching SELEX, we tested whether SAapta1 can distinguish them from SA (Fig. 3.5a). While 0.1 μM SAG caused only a 0.31nm optical fringe, 0.1 μM SA led to a much more pronounced optical fringe (1.30nm). Even 100 μM SAG resulted in only a 0.42nm optical fringe while 100 μM SA generated a 9.43nm signal shift. In fact, SA induced significantly more optical signal shift than SAG at all concentrations tested, and the optical shift induced by SAG was not statistically different from that induced by buffer alone. It should be noted that optical fringing did not increase with increasing concentrations of SAG, meaning that the signals generated by SAG are due to the non-specific binding with SAapta1. While similar results have been obtained

for MeSA, the optical fringe induced by MeSA is higher than SAG though still much lower than SA. Since the methyl group of MeSA is much smaller than the glucose group of SAG and thus causes less steric hindrance, it is more likely for MeSA to partially occupy the binding pocket of SA on SAapta1, explaining its stronger non-specific binding. In addition to SAG and MeSA, SA can also be converted to salicyloyl glucose ester (SGE) or methyl salicylate *O*- β -glucoside (MeSAG) in plants (Fig. 3.5b). Since both SGE and MeSAG have chemical groups with more steric hindrance than the methyl group of MeSA, it is anticipated that SAapta1 may easily distinguish SGE and MeSAG from SA. In addition to these SA conjugates that are larger than SA in molecular size, benzoic acid (BA), structurally similar to SA but smaller in molecular size, may bind SA aptamer without causing potential steric hindrance, so we also tested binding affinity between BA and SAapta1 (Fig. 3.5a). The signals induced by BA were not statistically different from those induced by buffer at all concentrations surveyed, so both the hydroxyl and the carboxyl groups are important to the binding specificity and affinity between SA and SAapta1.

To further verify the structural changes of SAapta1 induced by SA and to confirm its binding specificity using a different detection method, we obtained the circular dichroism spectra of SAapta1 mixed with SA, 4-HBA, MeSA, SAG, or BA (Fig. 3.5c). While SA caused dramatic structural changes, other SA metabolites and structural analogs produced negligible effects on

the structure of SAapta1. Taken together, these results confirm SA-induced structure-switching of SAapta1 and suggest that SAapta1 has good specificity and can discriminate SA metabolites not included in the negative selection step.

We also tested inter-day variation by measuring the sample SA sample on three different days (Fig. 3.5d). No statistically significant changes were detected by a one-way ANOVA, suggesting that measurements of the same sample recorded on different days do not statistically differ from one another, so we conclude that the nanoFPI sensor has good reproducibility along with its high sensitivity and specificity.

3.3.5 Detection of SA in plant extracts

To assess the feasibility of this aptamer-based nanoFPI sensor for SA detection in plant samples, the measurements of SA spiked in *Arabidopsis* extracts were obtained (Fig. 3.6a). The optical signal shift increased with increasing concentrations of SA spiked in, and the samples with plant extracts exhibited significantly higher signal shifts than those without plant extracts at all the concentrations of spike-in SA. These results suggest that this type of sensor is capable of detecting the basal SA levels in *Arabidopsis*. In addition to *Arabidopsis*, we further compared the performance of the nanoFPI sensor with HPLC using rice extracts (Fig. 3.6b). The nanoFPI sensor had statistically indistinguishable performance from that of HPLC. Binding specificity assay using pure MeSA solution showed that MeSA had low level non-specific binding to the

sensor (Fig. 3.5a). We performed GC-MS analysis (Fig. 3.6c) to test whether the endogenous MeSA might interfere with the detection of SA in plant extracts and found that our extraction method effectively excluded MeSA, making it barely detectable in the final extracts even by GC-MS. This shows that the non-specific binding of MeSA to the SAapta1 will not interfere with SA detection in plant extracts.

3.4 Conclusion

A structure-switching SELEX method was developed and an SA aptamer with high affinity and good specificity was successfully identified using the proposed method. A nanopore thin film sensor based on this SA aptamer was developed for detection of SA in buffer and plant extracts from *Arabidopsis* and rice. This type of nanosensor enabled detection of SA as low as 0.1 μM in buffer, significantly better than the sensitivity of an antibody-based method. The kinetics of the binding between SAapta1 and SA was studied, demonstrating signals that can reach steady state within 5 min when a low SA concentration is used. This type of sensor also has good specificity and can distinguish SA from its natural metabolites that also harbor SA moiety. The SA in plant extracts has also been successfully detected, suggesting the practical feasibility of this aptamer-based nanosensor, strongly suggesting that a nanoFPI sensor provides a promising sensing platform for aptamer-based small molecule detection.

References

- Balcke, G.U., Handrick, V., Bergau, N., Fichtner, M., Henning, A., Stellmach, H., Tissier, A., Hause, B., Frolov, A., 2012. An UPLC-MS/MS method for highly sensitive high-throughput analysis of phytohormones in plant tissues. *Plant Methods* 8 (1), 47.
- Bowling, S.A., Guo, A., Cao, H., Gordon, A.S., Klessig, D.F., Dong, X.I., 1994. A mutation in *Arabidopsis* that leads to constitutive expression of systemic acquired-resistance. *Plant Cell* 6 (12), 1845–1857.
- Bradbury, A., Pluckthun, A., 2015. Standardize antibodies used in research: to save millions of dollars and dramatically improve reproducibility, protein-binding reagents must be defined by their sequences and produced as recombinant proteins, say Andrew Bradbury, Andreas Pluckthun and 110 co-signatories. *Nature* 518 (7537), 27–30.
- Chang, Y.-H., Huang, C.-W., Fu, S.-F., Wu, M.-Y., Wu, T., Lin, Y.-W., 2017. Determination of salicylic acid using a magnetic iron oxide nanoparticle-based solid-phase extraction procedure followed by an online concentration technique through micellar electrokinetic capillary chromatography. *J. Chromatogr. A* 1479, 62–70.
- Chen, W.-T., Wang, C.-I., Fu, S.-F., Lin, Y.-W., 2014. Analysis of salicylic acid in tobacco leaves using capillary zone electrophoresis with UV detection. *GSTF J. Chem. Sci.* 1 (2).
- Clarke, J.D., Liu, Y.D., Klessig, D.F., Dong, X.N., 1998. Uncoupling PR gene expression from NPR1 and bacterial resistance: characterization of the dominant *Arabidopsis* cpr6-1 mutant. *Plant Cell* 10 (4), 557–569.
- Cleland, C.F., Ajami, A., 1974. Identification of the flower-inducing factor isolated from aphid honeydew as being salicylic acid. *Plant Physiol.* 54 (6), 904–906.
- Defraia, C.T., Schmelz, E.A., Mou, Z., 2008. A rapid biosensor-based method for quantification of free and glucose-conjugated salicylic acid. *Plant Methods* 4, 28.
- Dhiman, H., Shubhasis, D., Easha, B., Pradipta, S., Umesh, C.H., Tapan, K.P., 2015. A rapid LC-ESI-MS/MS method for the quantitation of salicylic acid, an active metabolite of

acetylsalicylic acid: application to in vivo pharmacokinetic and bioequivalence study in Indian healthy male volunteers. *Appl. Clin. Res. Clin. Trial. Regulat. Affairs* 2 (2), 90–102.

Du, F.Y., Ruan, G.H., Liu, H.W., 2012. Analytical methods for tracing plant hormones. *Anal. Bioanal. Chem.* 403 (1), 55–74.

Engelberth, J., Schmelz, E.A., Alborn, H.T., Cardoza, Y.J., Huang, J., Tumlinson, J.H., 2003. Simultaneous quantification of jasmonic acid and salicylic acid in plants by vapor-phase extraction and gas chromatography-chemical ionization-mass spectrometry. *Anal. Biochem.* 312 (2), 242–250.

Feng, S., Chen, C., Wang, W., Que, L., 2018. An aptamer nanopore-enabled microsensor for detection of theophylline. *Biosens. Bioelectron.* 105, 36–41.

Ferapontova, E.E., Olsen, E.M., Gothelf, K.V., 2008. An RNA aptamer-based electrochemical biosensor for detection of theophylline in serum. *J. Am. Chem. Soc.* 130 (13), 4256–4258.

Fu, Z.Q., Yan, S., Saleh, A., Wang, W., Ruble, J., Oka, N., Mohan, R., Spoel, S.H., Tada, Y., Zheng, N., Dong, X., 2012. NPR3 and NPR4 are receptors for the immune signal salicylic acid in plants. *Nature* 486 (7402), 228–232.

Gonzalez-Sanchez, M.I., Lee, P.T., Guy, R.H., Compton, R.G., 2015. In situ detection of salicylate in *Ocimum basilicum* plant leaves via reverse iontophoresis. *Chem. Commun.* 51 (92), 16534–16536.

Huang, W.E., Huang, L., Preston, G.M., Naylor, M., Carr, J.P., Li, Y., Singer, A.C., Whiteley, A.S., Wang, H., 2006. Quantitative in situ assay of salicylic acid in tobacco leaves using a genetically modified biosensor strain of *Acinetobacter* sp. ADP1. *Plant J.* 46 (6), 1073–1083.

Huang, W.E., Wang, H., Zheng, H., Huang, L., Singer, A.C., Thompson, I., Whiteley, A.S., 2005. Chromosomally located gene fusions constructed in *Acinetobacter* sp. ADP1 for the detection of salicylate. *Environ. Microbiol.* 7 (9), 1339–1348.

Kim, A.J., Lim, H.J., Ro, H., Ko, K.P., Han, S.Y., Chang, J.H., Lee, H.H., Chung, W., Jung, J.Y., 2014. Low-dose aspirin for prevention of cardiovascular disease in patients with chronic kidney disease. *PLoS One* 9 (8), e104179.

Kowalski, M.L., Asero, R., Bavbek, S., Blanca, M., Blanca-Lopez, N., Bochenek, G., Brockow, K., Campo, P., Celik, G., Cernadas, J., Cortellini, G., Gomes, E., Nizankowska-Mogilnicka, E., Romano, A., Szczeklik, A., Testi, S., Torres, M.J., Wohrl, S., Makowska, J., 2013. Classification and practical approach to the diagnosis and management of hypersensitivity to nonsteroidal anti-inflammatory drugs. *Allergy* 68 (10), 1219–1232.

Lawrence, J.R., Peter, R., Baxter, G.J., Robson, J., Graham, A.B., Paterson, J.R., 2003. Urinary excretion of salicyluric and salicylic acids by non-vegetarians, vegetarians, and patients taking low dose aspirin. *J. Clin. Pathol.* 56 (9), 651–653.

Li, Y.h., Wei, F., Dong, X.y., Peng, J.h., Liu, S.y., Chen, H., 2011. Simultaneous analysis of multiple endogenous plant hormones in leaf tissue of oilseed rape by solid-phase extraction coupled with high-performance liquid chromatography–electrospray ionisation tandem mass spectrometry. *Phytochem. Anal.* 22 (5), 442–449.

Oyola, S., Kirley, K., 2015. Another good reason to recommend low-dose aspirin. *J. Fam. Pract.* 64 (5), 301–303.

Pan, X., Welti, R., Wang, X., 2010. Quantitative analysis of major plant hormones in crude plant extracts by high-performance liquid chromatography–mass spectrometry. *Nat. Protoc.* 5 (6), 986.

Raskin, I., Ehmann, A., Melander, W.R., Meeuse, B.J., 1987. Salicylic Acid: a natural inducer of heat production in arum lilies. *Science* 237 (4822), 1601–1602.

Rhoads, D.M., McIntosh, L., 1992. Salicylic-acid regulation of respiration in higher-plants - alternative oxidase expression. *Plant Cell* 4 (9), 1131–1139.

Rothwell, P.M., Fowkes, F.G.R., Belch, J.F.F., Ogawa, H., Warlow, C.P., Meade, T.W., 2011. Effect of daily aspirin on long-term risk of death due to cancer: analysis of individual patient data from randomised trials. *Lancet* 377 (9759), 31–41.

Segarra, G., Jauregui, O., Casanova, E., Trillas, I., 2006. Simultaneous quantitative LC-ESI-MS/MS analyses of salicylic acid and jasmonic acid in crude extracts of *Cucumis sativus* under biotic stress. *Phytochemistry* 67 (4), 395–401.

Shakirova, F.M., Sakhabutdinova, A.R., Bezrukova, M.V., Fatkhutdinova, R.A., Fatkhutdinova, D.R., 2003. Changes in the hormonal status of wheat seedlings induced by salicylic acid and salinity. *Plant Sci.* 164 (3), 317–322.

Shaukat, A., Grau, M.V., Church, T.R., Baxter, G., Barry, E.L., Summers, R., Sandler, R.S., Baron, J.A., 2011. Serum salicylate levels and risk of recurrent colorectal adenomas. *Cancer Epidemiol. Biomarkers* 20 (4), 679–682.

Song, C., Chen, C., Che, X., Wang, W., Que, L., 2017. Detection of plant hormone abscisic acid (aba) using an optical aptamer-based sensor with a microfluidics capillary interface. In: *Micro Electro Mechanical Systems (MEMS), 2017 IEEE 30th International Conference on*. IEEE, pp. 370–373.

Szkop, M., Szkop, U., Kęszycka, P., Gajewska, D., 2017. A simple and robust protocol for fast RP-HPLC determination of salicylates in foods. *Food Anal. Methods* 10 (3), 618–625.

Tseng, P.-J., Wang, C.-Y., Huang, T.-Y., Chuang, Y.-Y., Fu, S.-F., Lin, Y.-W., 2014. A facile colorimetric assay for determination of salicylic acid in tobacco leaves using titanium dioxide nanoparticles. *Anal. Methods* 6 (6), 1759–1765.

Venema, D.P., Hollman, P.C.H., Janssen, K.P.L.T.M., Katan, M.B., 1996. Determination of acetylsalicylic acid and salicylic acid in foods, using HPLC with fluorescence detection. *J. Agric. Food Chem.* 44 (7), 1762–1767.

Vlot, A.C., Dempsey, D.A., Klessig, D.F., 2009. Salicylic Acid, a multifaceted hormone to combat disease. *Annu. Rev. Phytopathol.* 47, 177–206.

Voelker, R., 2014. USPSTF: low-dose aspirin may help reduce risk of preeclampsia. *Jama* 311 (20) 2055–2055.

Wang, S., Li, G., Xia, K., Xu, L., Chen, P., Zhou, X., 2001. Preparation and application of monoclonal antibodies specific for salicylic acid. *Acta Bot. Sin.* 43 (11), 1207–1210. Wang, S., Xu, L., Li, G., Chen, P., Xia, K., Zhou, X., 2002. An ELISA for the determination of salicylic acid in plants using a monoclonal antibody. *Plant Sci.* 162 (4), 529–535.

White, R.F., 1979. Acetylsalicylic-acid (aspirin) induces resistance to tobacco mosaic- virus in tobacco. *Virology* 99 (2), 410–412.

Yin, H., Li, X., Que, L., 2014. Fabrication and characterization of aluminum oxide thin film micropatterns on the glass substrate. *Microelectron. Eng.* 128, 66–70.

Zhang, T., Gong, Z., Giorno, R., Que, L., 2010. A nanostructured Fabry-Perot inter- ferometer. *Optic Express* 18 (19), 20282–20288.

Zhang, Y.L., Goritschnig, S., Dong, X.N., Li, X., 2003. A gain-of-function mutation in a plant disease resistance gene leads to constitutive activation of downstream signal transduction pathways in suppressor of npr1-1, constitutive 1. *Plant Cell* 15 (11), 2636–2646.

Zhou, M., Wang, W., Karapetyan, S., Mwimba, M., Marques, J., Buchler, N.E., Dong, X., 2015. Redox rhythm reinforces the circadian clock to gate immune response. *Nature* 523 (7561), 472–476.

Zubtsov, D.A., Ivanov, S.M., Rubina, A.Y., Dementieva, E.I., Chechetkin, V.R., Zasedatelev, A.S., 2006. Effect of mixing on reaction-diffusion kinetics for protein hydrogel-based microchips. *J. Biotechnol.* 122 (1), 16–27

Figures and tables

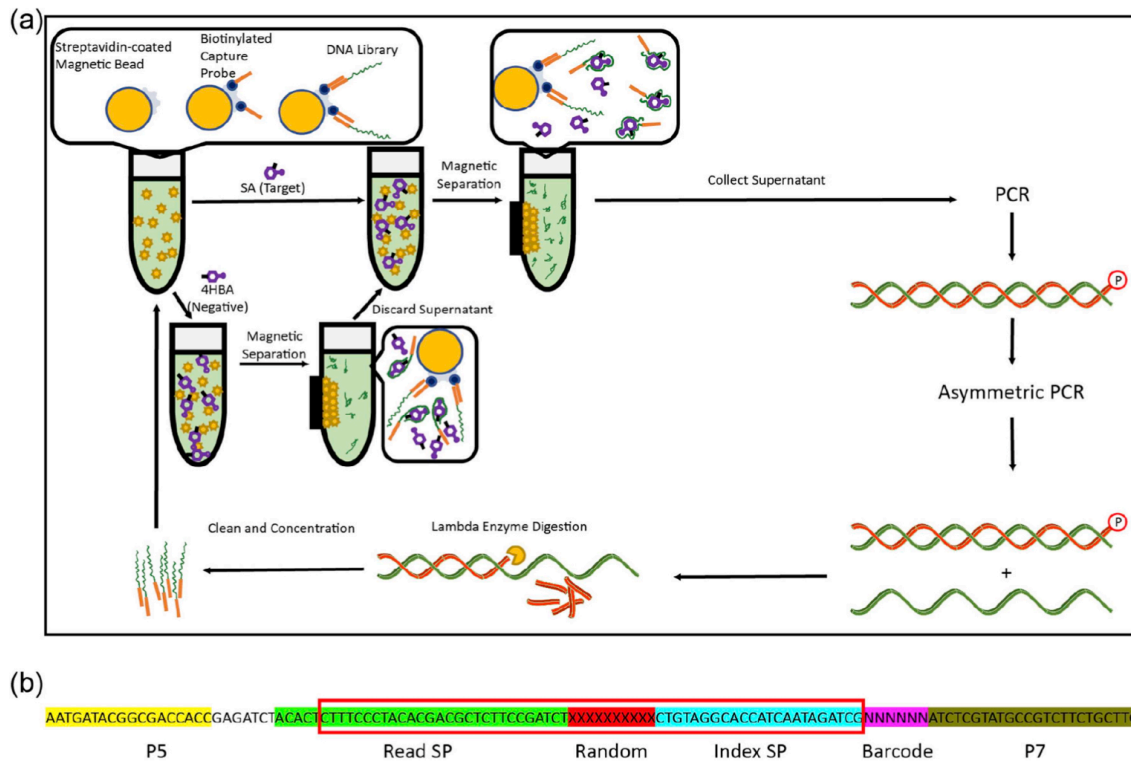


Figure 3. 1 (a) Pipeline of structure-switching SELEX; (b) Design of HiSeq-compatible SELEX library. The library sequence is highlighted by the red frame. P5 and P7 sequences are compatible with HiSeq. Read SP is the primer sequence for reading the 40 random nucleotides (“X” in the diagram). Index SP is the primer sequence for reading the 6-nucleotide index (“N” in the diagram). (For interpretation of the references to color in this figure legend, the reader is referred to the Web version of this article.)

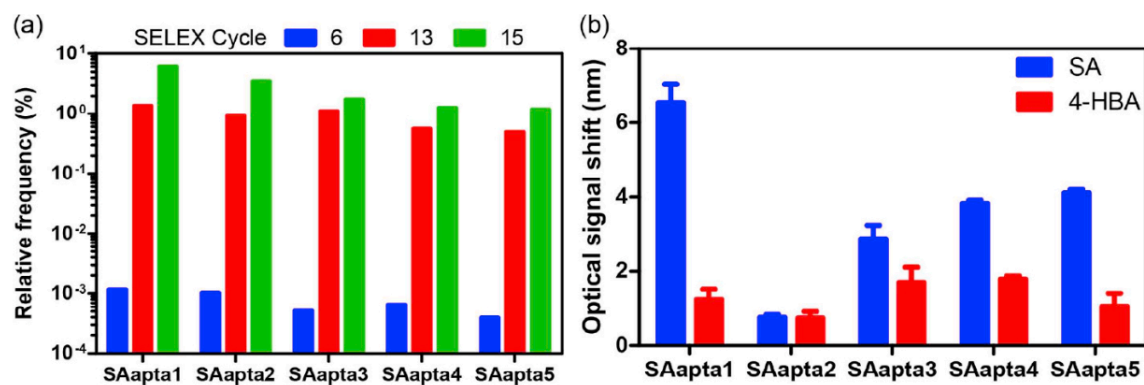


Figure 3. 2 (a) Relative frequency of the top five aptamer candidates over the 6th, 13th and 15th SELEX cycles; (b) Optical signal shift of the top five aptamer candidates using 40 μ M SA or 4-HBA. Mean \pm SEM was shown (n=6).

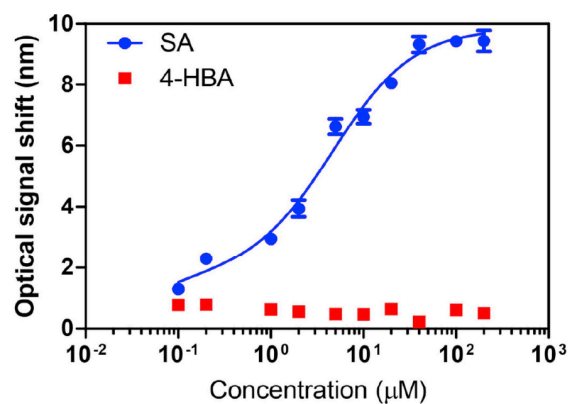


Figure 3. 3 Saturation curve of SAapt1 with SA and 4-HBA; Mean \pm SEM was shown (n=9)

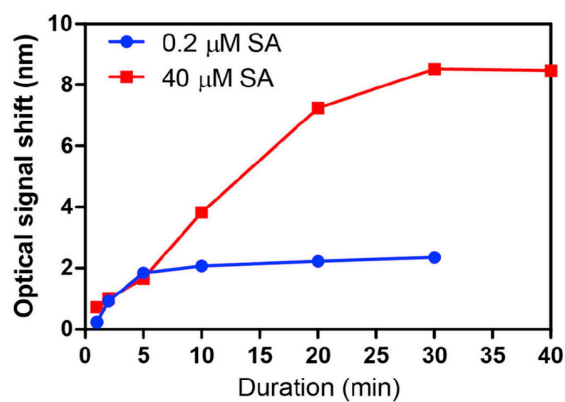


Figure 3. 4 Binding kinetics of SAapt1 with 0.2μM and 40 μM SA. Mean \pm SEM was shown (n=6)

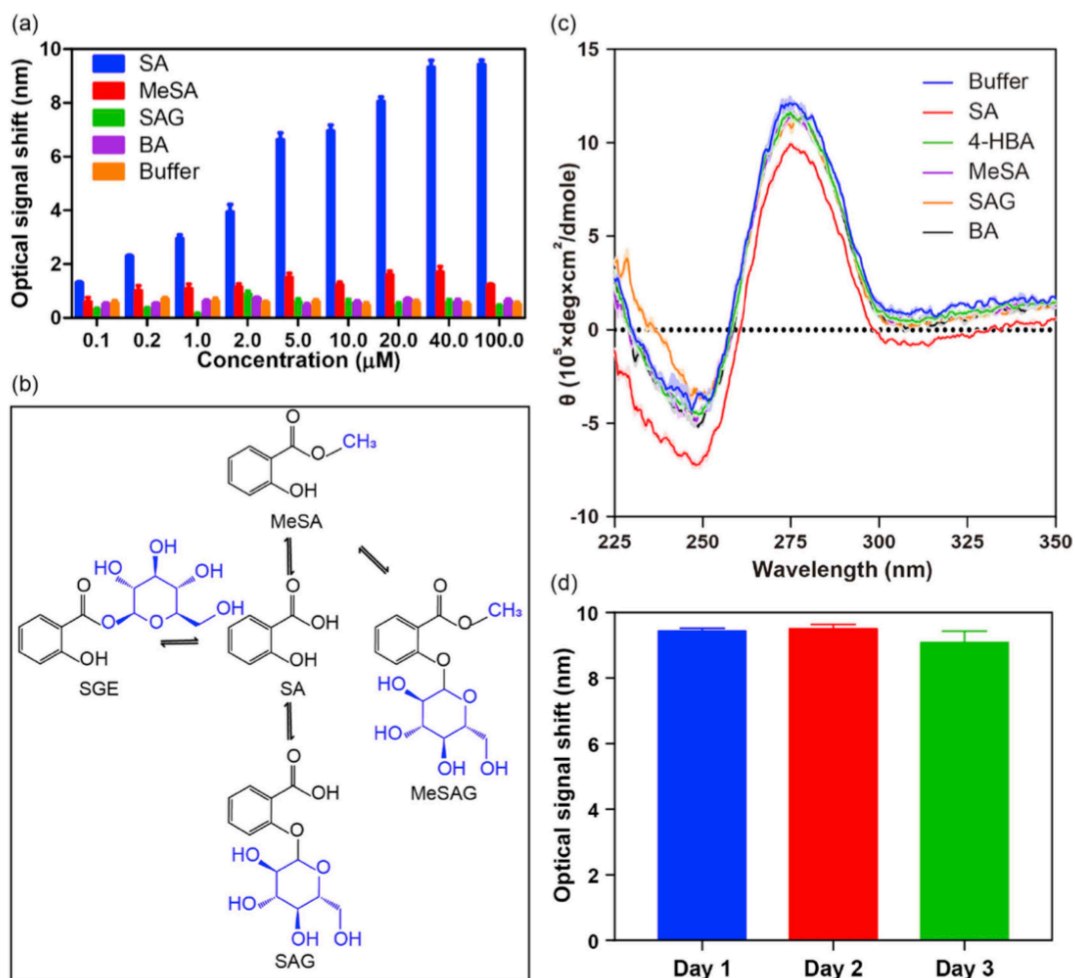


Figure 3. 5 (a) Optical signal shift induced by a series concentration of SA, MeSA, SAG, BA and buffer only; Mean \pm SEM was shown (n=9); (b) SA metabolites and their structures; (c) The circular dichroism spectra of 1 μM SAapt1 in the SELEX binding buffer with buffer, 40 μM SA, 4-HBA, MeSA, SAG and BA. Mean \pm SEM was shown (n=3). SEM was shown as light-colored area fill; (d) Optical signal shift of the same SA sample (40 μM) measured at three different days. Mean \pm SEM was shown (n=9). No statistically significant changes were detected using one-way ANOVA.

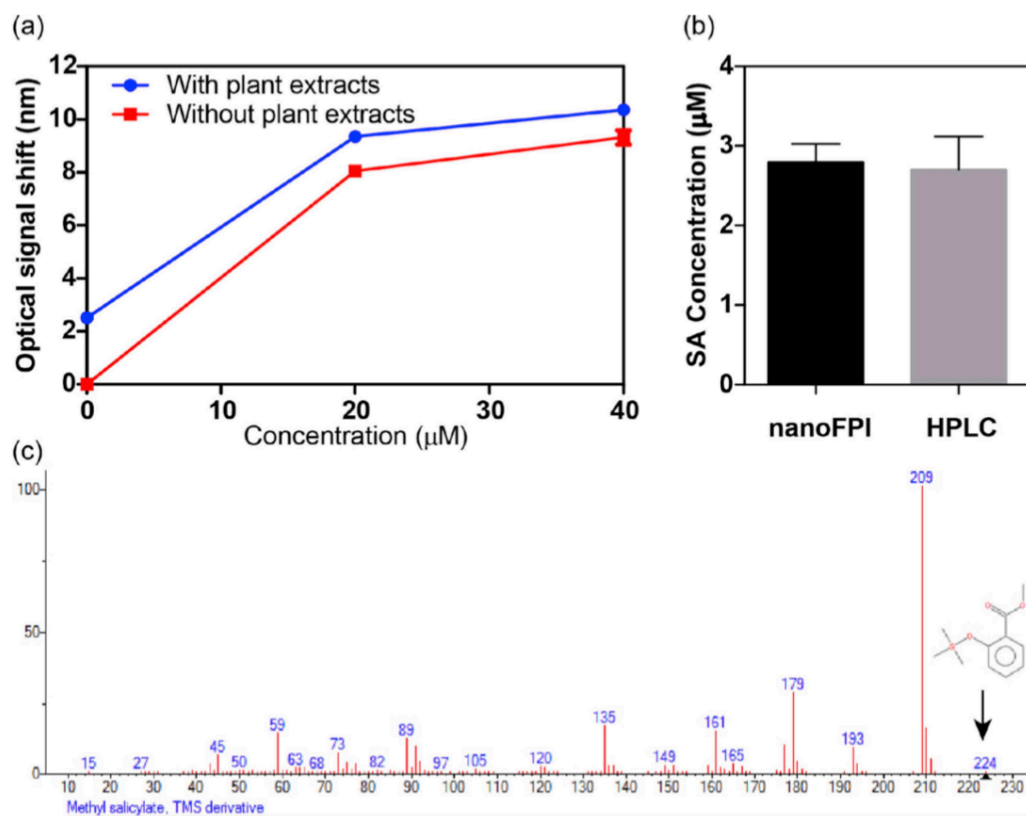


Figure 3. 6 (a) Optical signal shift of spike-in SA with and without Arabidopsis extracts. (b) Comparison between nanoFPI and HPLC using rice extracts. (c) Negligible detection of MeSA in rice extracts using GC-MS.

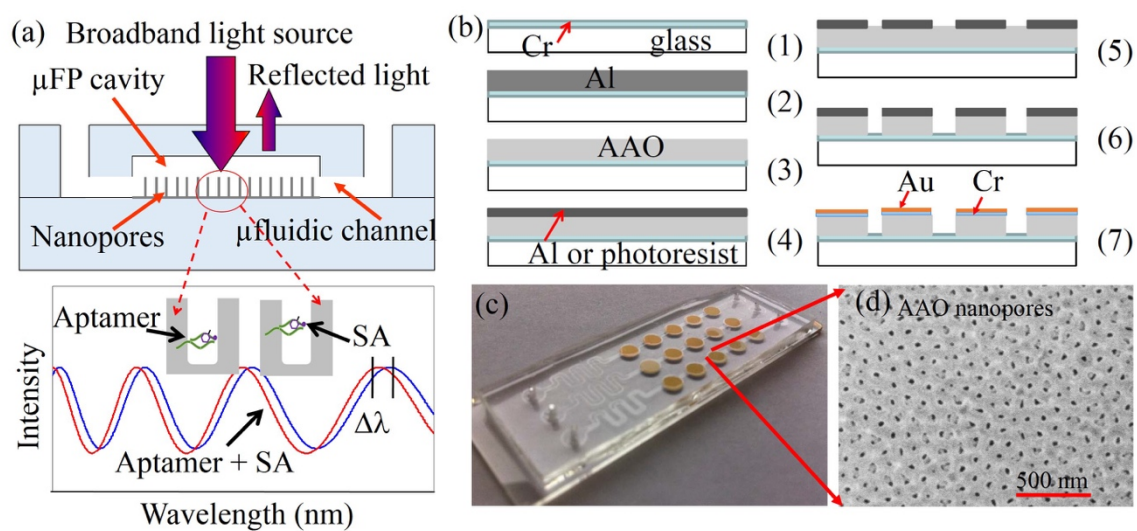


Figure S3. 1 Sketch of optical setup for the measurement and operational principle of the nanoFPI sensor and fabrication process flow.

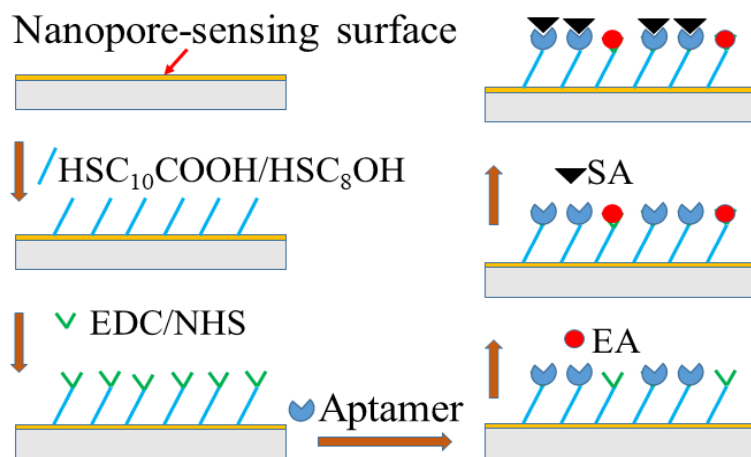


Figure S3. 2 Surface chemical functionalization of the nanoFPI sensor

Table 3. 1 Library, capture probes, and primers.

Oligo name	Sequence
Library	CTTTCCCTACACGACGCTCTTCCGATCT-N ₄₀ - CTGTAGGCACCATCAATAGATCG
7-mer Probe	GGGAAAG-Biotin
8-mer Probe	AGGGAAAG-Biotin
9-mer Probe	TAGGGAAAG-Biotin
Amplification-F	CTTTCCCTACACGACGCTCTTC
Amplification-R	Phos-CGATCTATTGATGGTGCCTACAG
SP-F	AATGATACGGCGACCACCGAGATCTACACTCTTCCCTACACGACG CTCTT
SP-R-6	CAAGCAGAAGACGGCATACGAGATCGTGATCGATCTATTGATGGT GCCTACAG
SP-R-13	CAAGCAGAAGACGGCATACGAGATGATCTGCGATCTATTGATGGT GCCTACAG
SP-R-15	CAAGCAGAAGACGGCATACGAGATTTGACTCGATCTATTGATGGT GCCTACAG

Table 3. 2 SA aptamer candidates

Oligo name	Sequence
SAapta1	/5AmMC12/CTTTCCCTACACGACGCTCTTCCGATCTTTCC CGTTACCCTTATCTCATGCCTGCACTTGATCATGGTCTGT AGGCACCATCAATAGATCG
SAapta2	/5AmMC12/CTTTCCCTACACGACGCTCTTCCGATCTTTCC CGTTACCTTTATCTCATGCCTGCACTTGATCATGGTCTGT AGGCACCATCAATAGATCG
SAapta3	/5AmMC12/CTTTCCCTACACGACGCTCTTCCGATCTGGAG CGTTTTTAATCTTTCCCTCTTTTCCCAACTTGCCTCTGTA GGCACCATCAATAGATCG
SAapta4	/5AmMC12/CTTTCCCTACACGACGCTCTTCCGATCTCGTC GTTGACTTTCCCACTTACCACGGATTGATTGTATGACTGT AGGCACCATCAATAGATCG
SAapta5	/5AmMC12/CTTTCCCTACACGACGCTCTTCCGATCTTTCC CACTATTTTGAAATAGTCATTCCCCTAAGTGATGGTCTG TAGGCACCATCAATAGATCG

CHAPTER 4. OPTICAL APTAMER-BASED SENSING CHIP FOR DETECTING PLANT HORMONES

Abstract

This paper reports a new chip equipped with aptamer-based sensors interfaced with a capillary microfluidics suitable for screening and detecting hormones in plant samples. The microfluidic capillary interface of the chip allows the samples to be automatically delivered to the sensors on the chip even without any external pumps, making it suitable for operation in the field or source-limited settings. The arrayed sensors can be functionalized with aptamers specific to different plant hormones, hence this chip can screen and identify the hormones from unknown samples. Since currently only an abscisic acid (ABA) aptamer and a salicylic acid (SA) aptamer are identified and available, as a technical demonstration, in this research, the sensors are only functionalized with ABA aptamer and SA aptamer to evaluate the performance of this chip. Using this chip, the detection of five plant hormones (ABA, SA, auxins, cytokinins, gibberellins) in buffer and plant extracts has been demonstrated with very good specificity and high sensitivity. And the sensors can detect both ABA and SA as low as 0.1 μM . All these measurements require only 1 μl samples and could be carried out within less than 30 min. Given its minimal external equipment operational requirement, this chip offers a promising platform for low-cost, rapid, sensitive screening and identification of plant hormones from raw plant samples in the field.

Key words: Multiplexed biodetection; aptamer-based biosensing; nanopore thin film sensor; plant hormone detection; plant extract.

4.1. Introduction

Most physiological and development processes in plants are regulated by plant hormones. Plant hormones are small molecular natural products, including auxins, cytokinins, gibberellins (GA), abscisic acid (ABA), ethylene, salicylic acid (SA), etc. (Fu et al. 2011). It is important to quantitatively analyze plant hormones for in-depth study of their biosynthesis, transport, metabolism and molecular regulatory mechanisms. Currently radioimmunoassay, enzyme linked immunosorbent assay (ELISA) (Weiler 1984; Davis et al. 1985), and high-performance liquid chromatography (HPLC), and chromatography/mass spectrometry are widely-used laboratory procedures for detecting plant hormones (Müller, Düchting, and Weiler 2002). But these methods usually require skilled personnel and long-time analysis with high cost, hence are not suitable for point-of-care (POC) testing in the field. Capillary electrophoresis (CE) was tested as an alternative to HPLC-based methods because of its faster speed, simpler sample preparation and lower cost. However, CE uses extremely high voltage for electrophoresis possibly raising safety concerns to operators (Chang et al. 2017; Chen et al. 2014). Because of their simplicity, convenience and low-cost, electrochemical techniques have been used for developing microdevices as an alternative approach (Fu et al. 2011). However, due to their poor stability and reproducibility, in practice electrochemical techniques are not widely used. Nowadays, electrochemical biosensors represent only an early stage of methodology probes for detecting plant hormones.

For the goal of detecting plant hormones in a cost-effective manner and for on-site field applications, the following three aspects should be considered in chip design.

First, to achieve the cost-effectiveness, reliability, and reusability of the sensors, the

aptamer-based sensing has been selected because it offers a cost-effective platform with very good temperature stability, a wide tolerance range of pH and salt concentration, and similar if not better, specificity and affinity with respect to antibody-based sensing (Conrad et al. 1996). Aptamers can also be reversibly denatured for the release of target molecules, making an aptamer-based sensor capable of reuse. **Second**, for on-site field applications, capillary microfluidics has been selected as the sensor interface because liquid samples can autonomously, and with no requirement for peripheral equipment such as syringe pumps, be delivered to on-chip sensors through the capillary microfluidics for detection in a pre-programmed manner. **Third**, for the determination of the types of hormones inside the unknown samples, the chip should be able to simultaneously screen a panel of hormones from the samples, so arrayed sensors must be integrated on a single chip for distinguishing different hormones.

This paper reports a new type of chip consisting of arrayed optical aptamer-based sensors with a microfluidics capillary interface that allows the plant samples to be automatically flowed into the chip for detection, making it possible to identify different hormones in the samples. The aptamer-based arrayed sensors combined with the microfluidics capillary interface make the chip particularly suitable for low-cost POC application in the field or in other source-limited settings. The capillary interface on the chip is adapted from previous work (Olanrewaju et al. 2018). It consists of a series of specifically designed SU8 microstructures, resulting in open-channel capillary micropumps and passive stop-valves (Zimmermann et al. 2007). With them, the solution samples can be automatically delivered to the sensors on chip by the capillary force and can be contained in the region of the sensors as well by the passive stop-valves

(Zimmermann, Hunziker, and Delamarche 2008). The aptamer sensors on the chip are adapted from the AAO nanopore thin film sensors (NanoFPI sensors) developed in our lab. Its dynamic detection range is at least between 0.1 μM to 100 μM as demonstrated (Chen et al. 2019). It should be noted that the goal of this effort is to develop an integrated chip suitable for field application for monitoring the plant hormones, which is a new and has been not reported before. It should be noted that currently only an abscisic acid (ABA) aptamer and a salicylic acid (SA) aptamer are identified and available. In this paper, the sensors on chip are only functionalized with ABA aptamer and SA aptamer to evaluate their performance. In addition, different from the work we reported before (Song et al. 2017), the regeneration of these sensors have been systematically evaluated for the reusability of the lab.

4.2. Materials and Methods

4.2.1. Chemicals and materials

11-Mercaptoundecanoic acid ($\text{HSC}_{10}\text{COOH}$, 99%), 8-mercapto-1-Octanol (HSC_8OH , 98%), N-(3-Dimethylaminopropyl)-N'-ethylcarbodiimide hydrochloride (EDC), N-hydroxysuccinimide (NHS), ethanolamine (EA), and salicylic acid were purchased from Sigma, and pH8 phosphate buffer, phosphoric acid (PPA), methanol, Ethyl Acetate, Cyclopentane were purchased from Sigma-Aldrich (Milwaukee, WI) and used without further purification. Deionized (DI) water was obtained from a DI water purification system (Millipore, FRANCE).

The aptamer (Integrated DNA Technologies, Inc) for ABA, purchased from Biobasic (CA), is:

GCGGATGAAGACTGGTGTCCCTTATGGTGGGTGCGCTGGGGCTGCAATCTTTT

GGCTGGCCCTAAATACGAGCAAC. The binding buffer for ABA was 20 mM Tris-HCl, pH 7.4, 2 mM MgCl₂, 100 mM NaCl, 5 mM KCl, 1 mM CaCl₂, 0.02% Tween20.

The aptamer for SA, recently identified by our team using SELEX (Chen et al. 2019), and purchased from Biobasic (CA), is:

5AmMC12/CTTTCCTACACGACGCTCTTCCGATCTTTCCCGTTACCCTTATCTCATGCCTGCACTTGATCATGGTCTGTAGGCACCATCAATAGATCG. The binding buffer for SA is 50Mm Tris, 137Mm, NaCl, 5 Mm MgCl₂, Ph 7.4.

4.2.2 Description and operational principle of the chip

The sketch of the chip is given in **Fig. 4.1a**. It consists of arrayed nanostructured Fabry-Perot interference (nanoFPI) sensors (Zhang et al. 2010; Zhang et al. 2012), the SU8 microstructures enabled capillary pumps at both upstream and downstream, the SU8 microstructures enabled capillary stop-valves. The SU8 microstructures of rectangle shapes with dimensions from 15-250 μm serves as the capillary pumps. The capillary pumps are designed to have a small flow resistance and are preceded by a constricted microchannel that acts as a flow resistance (Martin et al., 2007). The arrayed passive stop-valves prevent the liquid from flowing out of the NanoFPI sensor region due to a sharp change in the liquid-sidewall angle (Zimmermann, Hunziker, and Delamarche 2008). To facilitate the application of different aptamers to the arrayed NanoFPI sensors and the detection of samples, a removable PDMS microfluidic layer (**Fig. 4.1a**) is used.

The procedure for surface functionalization of the sensors with aptamers can be summarized as the follows: **First**, through the inputs 1, 2, 3 of the capillary pump enabled by the SU8 micro-structures (Abgrall and Gue 2007; Olanrewaju et al. 2018) (**Fig. 4.1b**), the sensor surfaces are functionalized by EDC/NHS chemistry, as detailed in **Section 4.2.4** and another publication (Feng et al. 2018). At the downstream of the chip closest to

the sensors (**Fig. 4.1c**), some capillary passive valves are integrated to prevent the chemicals from flowing out of the sensor region and ensure the incubation of the chemicals in the sensor region. When the sensors require rinsing, a buffer solution will be flowed into two capillary pumps through inputs 1, 2, 3 and 4, which are integrated with the upstream and the downstream of the passive valves (**Fig.4.1a-c**), respectively. In this way, the chemicals can be delivered to the sensors and the chip can be automatically cleaned with no need of external pumps. **Second**, the aptamers for SA and ABA are then applied to the sensors through the removable PDMS microfluidics layer. After overnight incubation, the chip is ready to detect plant hormones. To allow the solution samples to be screened and detected by the arrayed NanoFPI sensors, the PDMS microfluidics layer is removed so that the samples can be flowed to all the sensors by the capillary pump. In this study, we can *only* demonstrate the detection and screening of five plant hormones using ABA and SA aptamer sensors on chip, since the aptamers for other plant hormones (auxins, cytokinins, gibberellins) are either unavailable or unidentified. **Third**, the samples are delivered to the chip through the inputs 1, 2, 3, and again the samples will be automatically transported to the NanoFPI sensors for detection by the capillary force of the SU8 micro-structures for detection. The NanoFPI sensors are fabricated from an anodic aluminum oxide (AAO) thin film that provides periodically distributed nanopores. The operational principle of the NanoFPI sensor is illustrated in **Fig. 4.1d**. When the aptamer binds to the specific plant hormones, the shift of the optical signal (interference fringes) reflected from the sensors occurs, which is used as the transducing signal (Alvarez et al. 2009).

4.2.3 Fabrication process of the chip

The chip was fabricated using the process flow shown in **Fig. S1 (in supplementary document)** (He, Li, and Que 2014). **First**, 1.5×4.5 -inch glass wafer was cleaned using ultrasonication for 15 mins in acetone, IPA, and DI water in sequence. 10nm Cr was then deposited on a cleaned coverslip glass substrate, followed by depositing 2-3 μm Al (99.999%) layer using E-beam evaporation. Anodization was then performed in a 0.3M chromic acid (H_2CrO_4) solution for 20 mins at 30V and 5.8°C. The anodically grown aluminum oxide films were then etched in a 6 wt% phosphoric acid (H_3PO_4) solution at room temperature for 10 mins. The second anodization was performed under the same conditions as the first, so a layer of AAO was formed on the entire glass substrate, followed by a 150 nm Al coating on the AAO. A photoresist (AZ 5214-E IR) layer was then spun on top of the Al surface, and square patterns were exposed to ultraviolet light. The photoresist was then developed and the unprotected Al area were etched using aluminum etchant type A (Transene INC, Danvers, MA) and the patterned Al was thus used as the mask. The substrate was immersed in a mixture of phosphoric acid (0.4M) and chromic acid (0.2M) at 65°C for 10 mins to etch away the unprotected AAO and transfer the Al patterns onto the AAO layer after which the Al was etched away. To complete sensor fabrication, 10 nm Au layer was then deposited on the patterned AAO surface with the other part covered by a shadow mask. **Second**, the microfluidics capillary interface on the chip was fabricated from SU8, followed by bonding three PDMS slabs with inputs and outputs to the chip. **Third**, the removable microfluidic layer for flowing the aptamers was fabricated using a soft lithography process. Briefly, a SU-8 mold was formed on a silicon substrate. Polydimethylsiloxane

(PDMS) was then casted on the mold, followed by 1.5 hours of curing at a temperature of 65°C. The PDMS microfluidic layer was then peeled from the mold, and applied to the sensor region on the chip to be used to apply the aptamers to the sensors. As aforementioned, once the aptamers are immobilized on the NanoFPI sensors after incubation overnight on chip, this PDMS microfluidic layer is removed, and the NanoFPI sensors on chip can be used for screening and detecting the plant hormones.

4.2.4 Surface functionalization

The Au-coated sensor surface was functionalized with SA/ABA aptamers using 1-ethyl-3-(3-dimethylaminopropyl) carbodiimide (EDC)/N-hydroxysulfosuccinimide (NHS) chemistry as shown in **Fig. S2a (in supplementary document)**. Specifically, the sensor surface was immersed in the 0.1 mM HSC₁₀COOH/HSC₈OH solution for 30 minutes and then washed with ethanol. After the surface had been dried, it was immersed in a solution of NHS and EDC (NHS 0.2M, EDC 0.05M) for 30 minutes, after which the sensor surface was washed with PBS buffer and then immersed in the 5 µM ABA aptamer or SA aptamer solution overnight. This was followed by loading of 100 µl 1 M ethanolamine (EA) to block the non-occupied sites activated by the EDC/NHS. Finally, the sensor surface was rinsed with the binding buffer to flush off non-specifically adsorbed proteins. At this stage, the sensor was ready for measurement of the hormones in the samples.

4.2.5 Instrumentation

The detection setup is shown in **Fig. S2b (in supplementary document)**. A broadband light source from a tungsten halogen lamp is coupled to a specifically-designed optical fiber probe (Ocean Optics, Inc., Dunedin, FL, USA), perpendicularly illuminating the sensor surface. The reflected signals (transducing signals) are collected

by the same optical fiber probe, leading to an optical spectrometer (Ocean Optics, Inc.), that can detect an optical spectrum from 350 nm to 1050 nm. The spectrometer is connected to a laptop computer for data acquisition and processing. The biochemical samples are transported to the chip through the assembled plastic tubes (Upchurch Scientific, Inc.) by pump-controlled syringe (Harvard Apparatus, MA, USA). The chip can be placed on a lab shaker (Magnetic stirrer, Thermo Fisher Scientific, Inc) to enhance the diffusion speed of the plant hormone to the aptamer.

4.2.6 Detection procedure

For all the measurements, after the surface of the sensors had been functionalized with SA aptamer or ABA aptamer, a series of concentrations of SA or ABA in the buffer and plant extracts as well as a series of concentrations of three other plant hormones (auxins, cytokinins, gibberellins) are applied through inputs 1, 2, 3 to the sensors and followed by 30-minute incubation. Readings were taken after triple rigorous rinsing. The assay parameters including the concentrations of the aptamers (i.e. 5 μ M SA aptamer and 5 μ M ABA aptamer) and the incubation times (i.e. 30 min) were optimized to achieve high sensitivity and high signal to noise ratios based on our previous work (Chen et al. 2019). In these experiments, as technical demonstrations, four concentrations (0 μ M, 4 μ M, 20 μ M and 40 μ M) of all plant hormones have been detected. As aforementioned, the dynamic detection range of the NanoFPI sensors is at least from 0 to 100 μ M as demonstrated (Chen et al. 2019). Experiments for negative controls were carried out to employing the full assay procedure but without these plant hormones.

4.2.6 ABA and SA extraction from plant leaves

Arabidopsis leaves were ground into a fine powder in liquid nitrogen using a mortar and pestle. One gram of the resulting sample was then transferred into a 15-mL tube, mixed with 10 mL of cold extraction buffer (methanol: water: acetic acid, 80: 19: 1, v/v/v), and kept on ice for 1 hour with occasionally shaking, and then centrifuged at $3700\times g$ for 15 min at 4°C. The supernatant was filtered using a syringe-facilitated filter of pore size 0.4 μm . This plant extract was supplemented with ABA to achieve the required concentration.

Arabidopsis leaves or rice aerial parts were ground to a fine powder in liquid nitrogen using a mortar and pestle, and 8 g of the fine powder was transferred to a 50-ml falcon tube, mixed with 28 ml 90% methanol, then vortexed and sonicated for 16 min. The supernatant was collected after centrifugation at 20,800g for 5 min and 2 ml 0.2 M NaOH was added to the supernatant. The combined supernatant was then dried overnight at room temperature (RT) by speed-vac. The resulting residue was then resuspended in 20 ml of 5% trichloroacetic acid and sonicated for another 16 min, then centrifuged at 20,800g for 5 min and the supernatant was collected. This sample was extracted twice by adding 20 ml of ethyl acetate-cyclopentane (1:1), vortexed, sonicated for 16 min and centrifuged at 20,800g for 1 min. The organic phase was then combined and dried at room temperature by a speed-vac. The dried extract was then dissolved in 16 ml of SELEX binding buffer. The supernatant was filtered using a syringe-facilitated filter of pore size 0.2 μm . This plant extract was then supplemented with or without SA to the required concentrations.

4.2.7 Data acquisition and statistical analysis

The average shift of the fringes for the measured transducing signals of the NanoFPI sensors was obtained by (i) first obtaining the shift of the optical signal after ABA or SA was bound to the aptamer, then (ii) averaging the shift of all the peaks of fringes in the optical signal. The transducing signal of the same sample was measured by least on three sensors to obtain the average value.

4.3. Results and Discussion

4.3.1 Fabricated chip and its function demonstration

A photo of the fabricated chip is shown in **Fig. 4.2a**, and SEM images of the SU8-based microfluidics capillary structures and the passive valves are given in **Fig. 4.2b-c**. The SEM image of the nanopore-sensor, fabricated by anodizing the Al thin film, is shown in **Fig. 4.2d**. The thickness of the SU8 microstructures is $\sim 30\ \mu\text{m}$.

Because of its clear visibility, the blue food dye was used to demonstrate the functions of the capillary microfluidics (**Fig. 4.3**). The food dye was continuously conveyed into the *inputs 1, 2, 3* using pipettes. As a result, it is automatically flowed through the SU8 microstructures-enabled capillary microfluidics (**Fig. 4.3a-b**), arrived at the sensor region (**Fig. 4.3c**), and finally reached the passive valves and then stops flowing (**Fig. 4.3d**). It takes $\sim 1\ \text{min}$ for the whole process. In order to make the blue food dye flow out of the passive valves, water was continuously introduced into the *input 4* of the capillary microfluidics at the downstream of the passive valves, draining the food dye from sensor region (**Fig. 4.3e-g**). Eventually all the food dye from the sensor region was cleaned up from the chip (**Fig. 4.3h**). It takes $\sim 1\ \text{min}$ to complete the cleaning process. Using these two processes, the surface functionalization process of the sensors described in **Section 4.2.4** was achieved.

4.3.2 Detection of hormones in buffer

Figure 4.4 shows the sensing responses (shift of optical interference fringes) of the sensors for different concentrations of plant hormones in buffer. One representative measured optical interference fringe for detecting ABA at different concentrations is shown in **Fig. 4.4a**. The measured responses of five plant hormones from ABA-sensors, sensors functionalized with ABA aptamer, are given in **Fig. 4.4b**. The concentrations of these plant hormones (ABA, SA, auxins, cytokinins, gibberellins) in the buffer increase from 0 μM to 40 μM . As shown, for the ABA samples, the shift of the optical interference fringes increases from 0.7 nm to 3.7 nm, resulting from the increased change of effective refractive index due to the increased binding of ABA with ABA aptamer. In contrast, for other plant hormones (SA, auxins, cytokinins, gibberellins), the optical signal shift is in the range of 0.2 nm to 0.7 nm, much lower than that of ABA samples. These results indicate the non-specific binding exists between these plant hormones and ABA aptamer. But it is clear that ABA-sensors is much specific to ABA samples, suggesting that the specificity of the ABA-sensors is very high. In addition, using this sensor, it has been demonstrated that ABA sample at a concentration of 0.1 μM can be readily detected (**Fig. S3 in supplementary document**), offering better detection limit and sensitivity than the ELISA based ABA detection kit from Sigma (Song et al. 2017).

Similarly, one representative measured optical interference fringes for detecting SA at different concentrations is shown in **Fig. 4.4c**. The measured responses of five plant hormones from SA-sensors, sensors functionalized with SA aptamer, are given in **Fig. 4.4d**. The concentrations of these plant hormones (ABA, SA, auxins, cytokinins, gibberellins) in the buffer increase from 0 μM to 40 μM . As shown, for the SA samples, the shift of the optical interference fringes increases from 0.5 nm to 3.5 nm, resulting

from the increased change of effective refractive index due to the increased binding between SA with SA aptamer. In contrast, for other plant hormones (ABA, auxins, cytokinins, gibberellins), the optical signal shift is in a range of 0.5 nm to 1 nm. These indicate the non-specific binding exists between these plant hormones and SA aptamer. But it is clear that SA-sensors is much specific to SA samples, suggesting that the specificity of the SA-sensors is very high. In addition, it has been demonstrated that SA can be readily detected at levels as low as 0.1 μM (**Fig. S4 in supplementary document**) (Chen et al. 2019), which is significantly more sensitive than the antibody-based method (Wang et al. 2002) and comparable to or even better than the bacteria-based biosensor (Huang et al. 2006; Huang et al. 2005).

4.3.3 Regeneration of aptamer sensors

Binding of small molecules to an aptamer is highly reversible, making it possible to regenerate the sensor. The theophylline sensor can be regenerated to a degree of 99% by simply washing a used sensor with buffer (0.1 M pH7.2 PBS with 5 mM KCl and 1 mM MgCl_2) (Feng et al. 2018). Regeneration of an aptamer sensor is usually accomplished by denaturing the aptamer. The procedure of regeneration of the aptamer sensor is illustrated in **Fig. S5**. In simple terms, ABA or SA aptamer is capable of specifically binding to ABA or SA, respectively. After the aptamer has been conjugated to the sensor surface, ABA or SA migrates by capillary action, passes the conjugate pad, then interacts and binds with aptamer. To regenerate the sensor, the sensor is heated to 95 $^{\circ}\text{C}$ for 3 min and continuously rinsed by flowing buffer. The aptamer is denatured and thereby lose its native conformation, leading to the release of ABA or SA. After the

temperature has been lowered to room temperature, the aptamer will restore its tertiary structure and be ready again to bind its target, ABA or SA.

Experiments were carried out to demonstrate the regeneration and reusability of the sensors. **First**, an ABA-sensor was used to detect ABA in SELEX buffer of concentrations of 0, 4, 20, and 40 μM in sequence. After each measurement, the sensor was regenerated and rinsed using a PBS buffer. As shown in **Fig. 4.5a**, the optical signal shift is 0.9 nm for the SELEX buffer (0 μM ABA), after regeneration in PBS buffer, the optical signal becomes 0.4 nm. Clearly, for both buffers, the optical signal shift occurs because of the non-specific binding between ABA aptamer and chemicals in these buffers. The decrease of the optical signal shift in PBS buffer is that using PBS buffer with a higher salt concentration than SELEX buffer can reduce non-specific binding due to charge interaction by producing a shielding effect (Nicoya. 2015). The regenerated sensor is then used to detect ABA at the concentration of 4 μM , followed by regeneration. A similar procedure is applied to detect ABA at concentrations of 20 and 40 μM and regenerating in sequence. As shown in **Fig. 4.5a**, the optical signal shift increases from 0.9 nm to 3.5 nm, respectively. After each regeneration, the optical signal shift decreases clearly to 0.4, 0.6, 0.5, and 0.8 nm, respectively, indicating that the ABA sensor can be reset. **Second**, a SA-sensor can similarly be used to detect SA in buffer of concentrations of 0, 4, 20, and 40 μM . As shown in **Fig. 4.5b**, the optical signal shift increases from 0.8 nm to 3.3 nm, respectively. After each regeneration of the sensor, the optical signal shift decreases to 0.2, 0.6, 0.5, and 0.7 nm, respectively, again indicating that an SA-sensor can be reset. This shows that, both ABA-sensors and SA-sensors have reasonably good regeneration capability without significant loss of activity.

To examine the effect of the regeneration process on sensor repeatability, the following experiments were carried out. **First**, a specific concentration of ABA was measured by the same ABA-sensor three times. Between each measurement, the ABA-sensor was regenerated. The results are shown in **Fig. 4.5c**, demonstrating that as ABA concentration increases, the optical signal shift increases. For the same concentration, the measured three responses show a change of 5% after regeneration of the sensors, consistent with results reported by another research group (Ferafontova, Olsen, and Gothelf 2008). **Second**, the same measurements were performed on the SA-sensor, and the results shown in **Fig. 5d** reflect a trend similar to that of ABA-sensor. However, the three measured responses show a change of 3% for SA-sensor, indicating that a SA-sensor has higher reversibility than an ABA-sensor.

4.3.4 Detection of hormones in plant extracts

Figure 4.6 shows sensor responses when detecting hormones of different concentrations in plant extracts. Specifically, the measured results from ABA-sensors for five hormones in plant extracts are given in **Fig. 4.6a**, showing that the concentrations of these hormones in the plant extracts increase from 0 μM to 40 μM . For the ABA samples, the shift of the optical interference fringes increased from 1.2 nm to 4.5 nm, resulting from an increased change of effective refractive index due to the increased binding of ABA with ABA aptamer. In contrast, for other plant hormones (SA, auxins, cytokinins, gibberellins), the optical signal shift was in a range of 0.3 nm to 1 nm, indicating that while non-specific binding exists between these plant hormones and the ABA aptamer, compared to the signals from ABA samples, it is clear that the specificity of the ABA-sensors is very high. These results suggested that this type of sensor can detect the ABA in plant extracts.

Similarly, measured results from SA-sensors of five plant hormones in plant extracts are given in **Fig. 4.6b**, with the concentrations of these hormones in the plant extracts increasing from 0 μM to 40 μM . As shown, for the SA samples, the shift of the optical interference fringes increased from 0.7 nm to 5.2 nm, resulting from the increased change of effective refractive index due to the increased binding of SA to the SA aptamer. In contrast, for other plant hormones (ABA, auxins, cytokinins, gibberellins), the optical signal shift was in the 0.4 nm-0.8 nm, indicating that the non-specific binding exists between these plant hormones and the SA aptamer. Comparing the signals from the SA samples, it is clear that the specificity of the SA-sensors is very high, suggesting that this type of sensor can satisfactorily detect the SA in plant extracts.

It should be noted that, even though the non-specific binding for ABA-sensors and SA-sensors with other hormones and other contents in plant extractions is small, an optical fringe shift still exists (**Fig. 4.6**). Non-specific binding occurs because other chemicals can be adsorbed on to the sensor surface via simple non-covalent forces, including electrostatic or ionic bonds, hydrophobic interactions and van der Waals forces. To further cancel out the non-specific binding effect when detecting plant hormones in complex fluids, some reference sensors can be used to calibrate the shift due to the non-specific binding.

4.4. Conclusions

A chip containing arrayed optical aptamer-based sensors for detecting plant hormones with a microfluidics capillary interface has been developed. The arrayed sensors on the chip facilitate the screening and detection of a panel of hormones in samples, while a microfluidics capillary interface allows the samples to be automatically

delivered to the sensors without any external pumps, paving a way for its potential point-of-care application in the field. Experiments have determined that the detection limit is 0.1 μM of both the ABA-sensor and the SA-sensor, lower than that of the commercially available ELISA based ABA detection kit from Sigma. Both sensors have very good specificity. The detection of ABA and SA in plant extracts has been also demonstrated with very good specificity. Given its high sensitivity, specificity and reusability, this chip offers a new cost-effective platform that can potentially distinguish and screen different plant hormones in raw plant samples.

References

- Abgrall, P, and AM Gue. 2007. 'Lab-on-chip technologies: making a microfluidic network and coupling it into a complete microsystem—a review', *Journal of Micromechanics and Microengineering*, 17: R15.
- Alvarez, Sara D, Chang-Peng Li, Casey E Chiang, Ivan K Schuller, and Michael J Sailor. 2009. 'A label-free porous alumina interferometric immunosensor', *Acs Nano*, 3: 3301-07.
- Chang, Yu-Hsuan, Chang-Wei Huang, Shih-Feng Fu, Mei-Yao Wu, Tsunghsueh Wu, and Yang-Wei Lin. 2017. 'Determination of salicylic acid using a magnetic iron oxide nanoparticle-based solid-phase extraction procedure followed by an online concentration technique through micellar electrokinetic capillary chromatography', *Journal of Chromatography A*, 1479: 62-70.
- Chen, Changtian, Silu Feng, Mian Zhou, Chonghui Ji, Long Que, and Wei Wang. 2019. 'Development of a structure-switching aptamer-based nanosensor for salicylic acid detection', *Biosensors and Bioelectronics*, 140: 111342.
- Chen, Wei-Ting, Chiung-I Wang, Shih-Feng Fu, and Yang-Wei Lin. 2014. 'Analysis of salicylic acid in tobacco leaves using capillary zone electrophoresis with UV detection', *GSTF J. Chem. Sci*, 1.
- Conrad, Richard C, Lori Giver, Yu Tian, and Andrew D Ellington. 1996. '[20] In vitro selection of nucleic acid aptamers that bind proteins.' in, *Methods in enzymology* (Elsevier).

Davis, Gregory C, Mich B Hein, Brian C Neely, C Ray Sharp, and Michael G Carnes. 1985. 'Strategies for the determination of plant hormones', *Analytical Chemistry*, 57: 638A-48A.

Feng, Silu, Changtian Chen, Wei Wang, and Long Que. 2018. 'An aptamer nanopore-enabled microsensor for detection of theophylline', *Biosensors and Bioelectronics*, 105: 36-41.

Ferapontova, Elena E, Eva M Olsen, and Kurt V Gothelf. 2008. 'An RNA aptamer-based electrochemical biosensor for detection of theophylline in serum', *Journal of the American Chemical Society*, 130: 4256-58.

Fu, JiHong, XiaoHong Sun, JiDe Wang, JinFang Chu, and CunYu Yan. 2011. 'Progress in quantitative analysis of plant hormones', *Chinese Science Bulletin*, 56: 355-66.

He, Yuan, Xiang Li, and Long Que. 2014. 'A transparent nanostructured optical biosensor', *Journal of biomedical nanotechnology*, 10: 767-74.

Huang, Wei E, Linfeng Huang, Gail M Preston, Martin Naylor, John P Carr, Yanhong Li, Andrew C Singer, Andrew S Whiteley, and Hui Wang. 2006. 'Quantitative in situ assay of salicylic acid in tobacco leaves using a genetically modified biosensor strain of *Acinetobacter* sp. ADP1', *The Plant Journal*, 46: 1073-83.

Huang, Wei E, Hui Wang, Hongjun Zheng, Linfeng Huang, Andrew C Singer, Ian Thompson, and Andrew S Whiteley. 2005. 'Chromosomally located gene fusions constructed in *Acinetobacter* sp. ADP1 for the detection of salicylate', *Environmental Microbiology*, 7: 1339-48.

Müller, Axel, Petra Düchting, and Elmar W Weiler. 2002. 'A multiplex GC-MS/MS technique for the sensitive and quantitative single-run analysis of acidic phytohormones and related compounds, and its application to *Arabidopsis thaliana*', *Planta*, 216: 44-56.

Nicoya. 2015. "<https://www.nicoyalife.com/wp-content/uploads/2015/11/Reducing-Non-Specific-Binding-in-Surface-Plasmon-Resonance-Experiments.pdf>". Reducing Non-specific binding in surface plasmon resonance experiments.

Olanrewaju, Ayokunle, Maiwenn Beaugrand, Mohamed Yafia, and David Juncker. 2018. 'Capillary microfluidics in microchannels: from microfluidic networks to capillary circuits', *Lab on a Chip*, 18: 2323-47.

Song, Chao, Changtian Chen, Xiangchen Che, Wei Wang, and Long Que. 2017. "Detection of plant hormone abscisic acid (ABA) using an optical aptamer-based sensor with a microfluidics capillary interface." In *2017 IEEE 30th International Conference on Micro Electro Mechanical Systems (MEMS)*, 370-73. IEEE.

Wang, Shucui, Langlai Xu, Guojing Li, Puyan Chen, Kai Xia, and Xie Zhou. 2002. 'An ELISA for the determination of salicylic acid in plants using a monoclonal antibody', *Plant Science*, 162: 529-35.

Weiler, EW. 1984. 'Immunoassay of plant growth regulators', *Annual review of plant physiology*, 35: 85-95.

Zhang, Tianhua, Zhongcheng Gong, Rebecca Giorno, and Long Que. 2010. 'A nanostructured Fabry-Perot interferometer', *Optics express*, 18: 20282-88.

Zhang, Tianhua, Yuan He, Jianjun Wei, and Long Que. 2012. 'Nanostructured optical microchips for cancer biomarker detection', *Biosensors and Bioelectronics*, 38: 382-88.

Zimmermann, M, P Hunziker, and E Delamarche. 2008. 'Valves for autonomous capillary systems', *Microfluidics and Nanofluidics*, 5: 395-402.

Zimmermann, Martin, Heinz Schmid, Patrick Hunziker, and Emmanuel Delamarche. 2007. 'Capillary pumps for autonomous capillary systems', *Lab on a Chip*, 7: 119-25

Figures

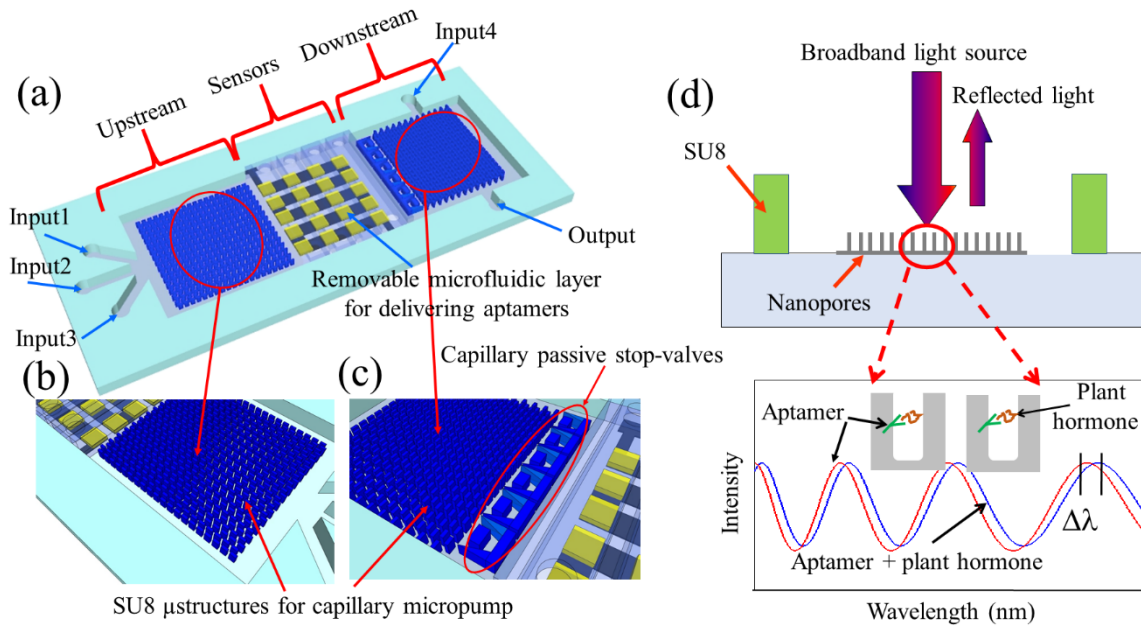


Figure 4. 1 (a) Schematic of the chip; (b) Close-up showing the SU8 microstructures of the capillary micropump in the upper stream; (c) Close-up showing the microstructures of the capillary micropump; (d) Optical sensor operational principle

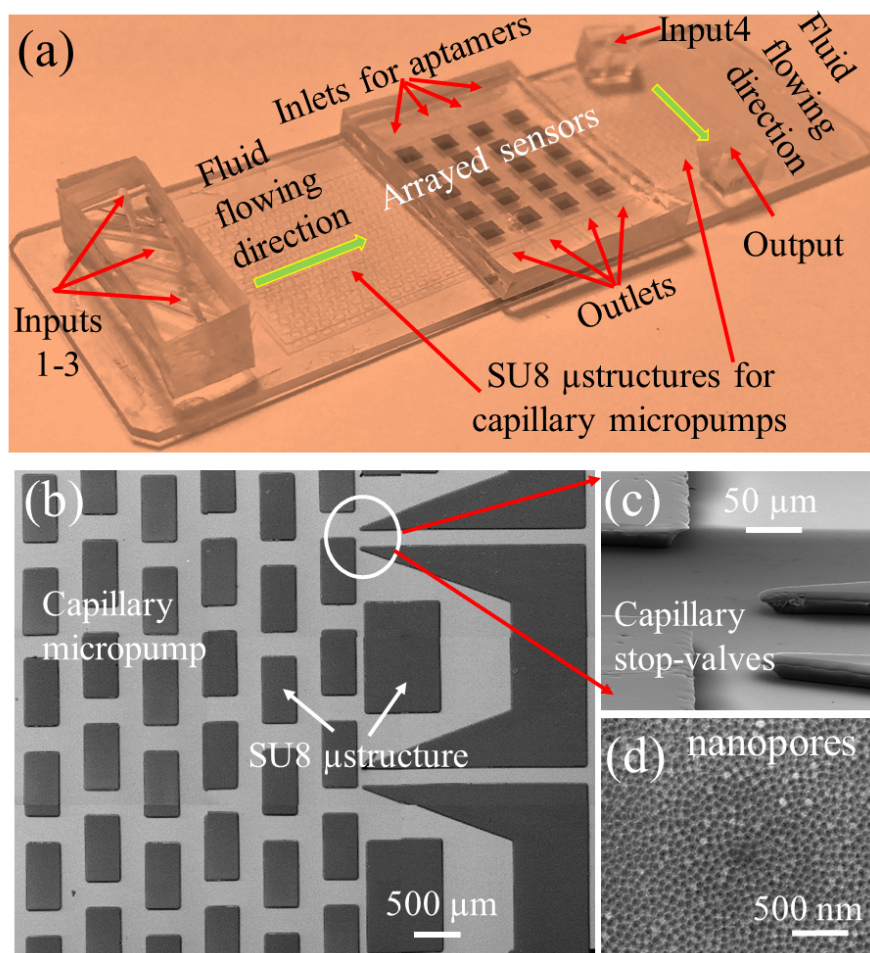


Figure 4. 2 (a) Photo of a fabricated chip bonded with PDMS slabs; SEM images of (b) the SU8 microstructures for capillary microfluidics; (c) the SU8 microfluidic passive valves, and (d) the nanopores on the nanoFPI sensors fabricated from anodic aluminum oxide

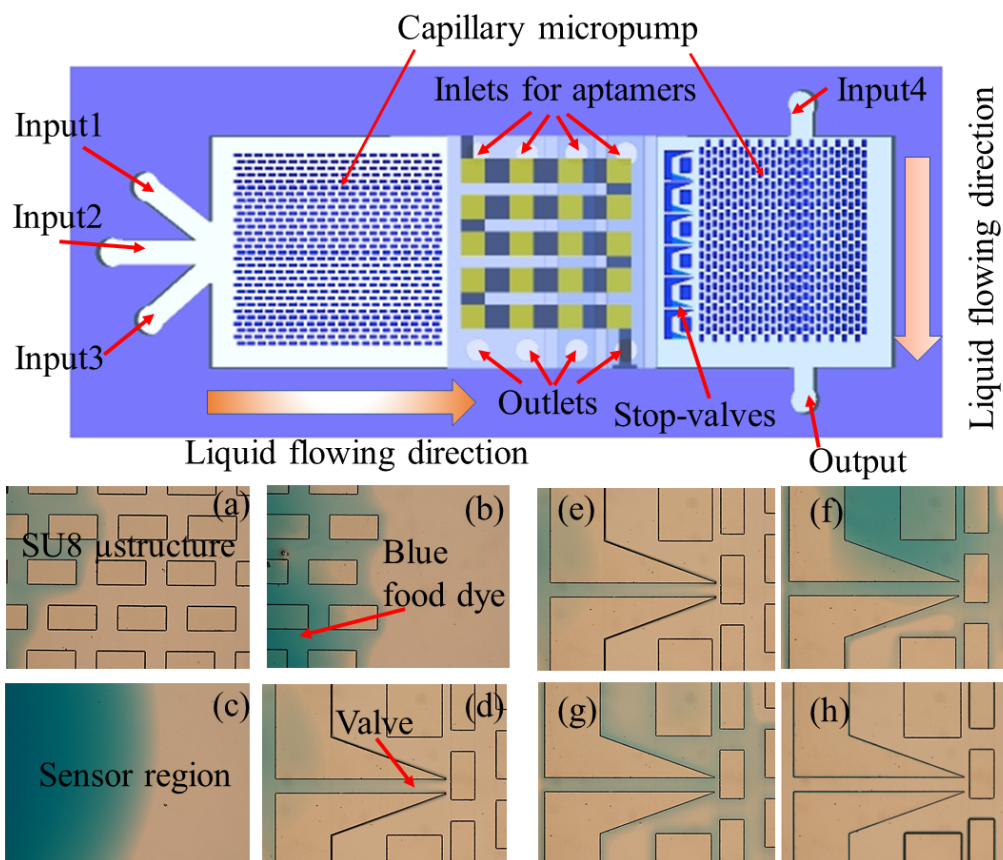


Figure 4.3 Demonstration of functions of the capillary microfluidics: (top) sketch of the chip; (a)-(b) food dye flows through the SU8 microstructures-enabled micropump due the capillary force from inputs 1, 2, 3; (c) food dye reaches the sensor region; (d) food dye reaches the capillary passive-stop valves; (e)-(f) water is flowed through the SU8 microstructures-enabled micropump to the passive-stop valves through input 4, the food dye is drained out of the sensor region; (h) food dye is washed out of the chip.

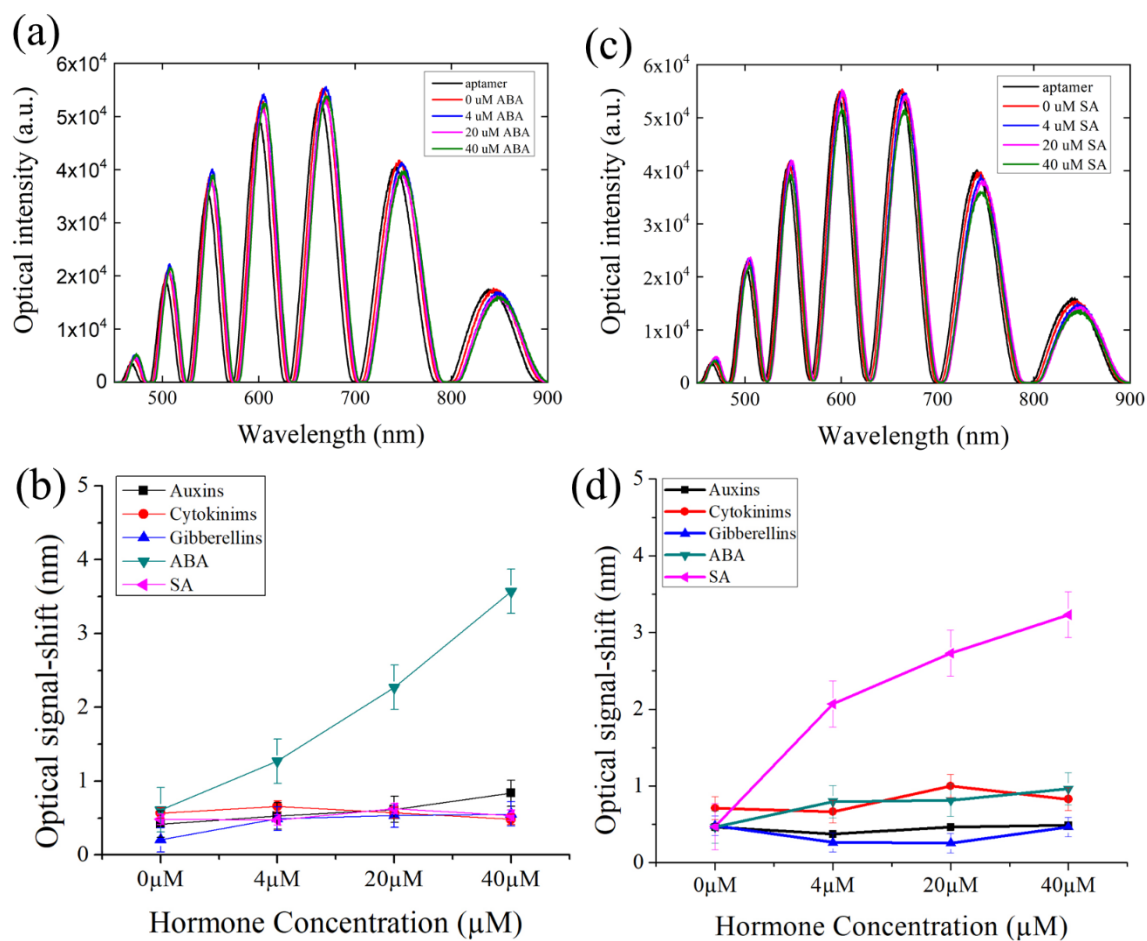


Figure 4. 4 Measured optical signals of five plant hormones in SELEX buffer: (a) optical interference fringes of ABA-sensors with different concentrations of ABA; (b) the optical signal shift for five plant hormones measured by ABA-sensors; (c) optical interference fringes of SA-sensors with different concentrations of SA; (b) the optical signal shift for five plant hormones measured by SA-sensors;

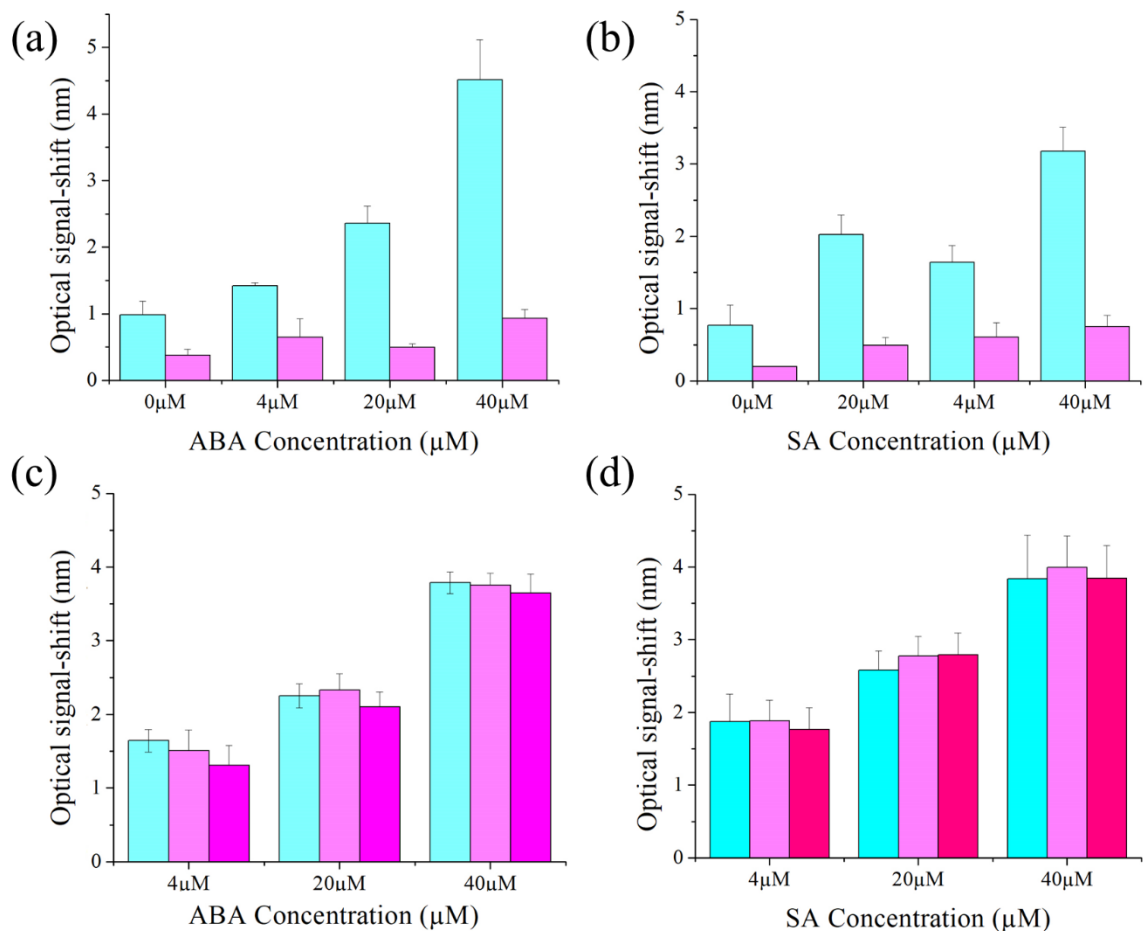


Figure 4. 5 Measured optical signals of ABA and SA in SELEX buffer on the regenerated sensor: (a) Measured optical signals of ABA in SELEX buffer on the same regenerated ABA-sensor and of the regenerated sensor after being rinsed by PBS buffer for each ABA concentration; (b) Measured optical signals of SA in SELEX buffer on the same regenerated SA-sensors and measured optical signals of the regenerated sensor after being rinsed by PBS buffer for each SA concentration; (c) Measured optical signals of ABA in SELEX buffer on the same ABA-sensor regenerated three times for each concentration; (b) Measured optical signals of SA in SELEX buffer on the same SA-sensor regenerated three times for each concentration.

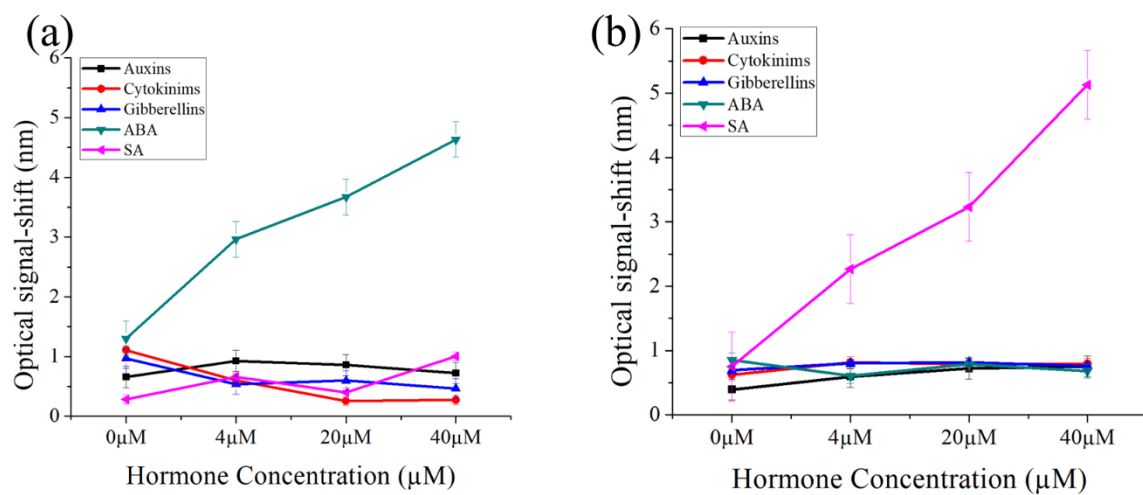


Figure 4. 6 Measured optical signals of five hormones spiked in plant extracts from (a) ABA-sensors and (b) SA-sensors on chip

CHAPTER 5. CONCLUSIONS AND FUTURE WORK

5.1 Conclusion

In this dissertation, it reports an aptamer-based nanopore thin film sensor for detecting plant chemicals. Based on the RIFS spectrum of AAO, two kinds of optical biosensor within microfluidic device have been developed.

In the second chapter, we assessed theophylline sensitivity and dynamic range, determined binding kinetics, tested ligand specificity, and, finally, tested influence of serum and plant extracts. It has been found that the aptamer-based sensor can detect theophylline at a concentration as low as $0.05\mu\text{M}$ and sensor can detect theophylline in a simple and fast manner with very good selectivity and specificity.

In the third chapter, we developed a structure-switching SELEX method for screening SA aptamer. The SA aptamer can distinguish SA from its natural metabolites which also harbor SA moiety, and shows high affinity and good specificity by using nanopore thin film sensor. We also compared the performance of our sensor with high performance liquid chromatography (HPLC). The result shows that our sensor had statistically indistinguishable performance as HPLC.

In the fourth chapter, we designed and fabricated a microfluidics capillary chip whose microfluidics capillary interface allowed samples to be automatically delivered to the sensor without external pumps, paving the way for point-of-use application in the field. The micropattern AAO can be potentially distinguish and screen different plant hormones in raw plant samples.

5.2 Future works

SELEX is widely used technique for selection of high affinity aptamers from an initial random ssDNA pool. Aptamers could be potentially and practically selected against any targets including small molecules, proteins, bacteria and viruses, cell lines and even whole cells (Noma,T et al., 2006; Pestourie.C et al., 2006; Blank, M et al., 2001; Ohuci, S et al., 2005; Harada, K et al., 1995; Huizenga, D.E. et al., 1995). Recently, researchers developed many different SELEX methods to suit their needs and make the selection process more efficient. SELEX process is usually time-consuming and labor-intensive due to multiple rounds of extraction and amplification. In addition, SELEX process also need large amounts of samples and reagents. Hence, we want to develop a new platform to perform the entire SELEX process by using microfluidics and micro-electromechanical-systems (MEMS) technology.

References

- Noma, T., Ikebukuro, K., Sode, K., Ohkubo, K., Sakasegawa, Y., Hachiya, N., Kaneko, K., 2006. A screening method for DNA aptamers that bind to specific, unidentified protein in tissue samples. *Biotechnol. Lett. Vol. 28*, pp.1377–1381.
- Pestourie, C., Cerchia, L., Gombert, K., Aissouni, Y., Boulay, J., De Franciscis, Y., Libri, D., Tavitian, B., Duconge, F., 2006. Comparison of different strategies to select aptamers against a transmembrane protein target. *Oligonucleotides. 16(4)*: 323–335.
- Blank, M., Weinschenk, T., Priemer, M., Schluesener, H., 2001. Systematic evolution of a DNA aptamer binding to rat brain tumor microvessels selective targeting of endothelial regulatory protein pigpen. *J. Biol. Chem. 276*, 16464–16468.
- Ohuci, S. P., Ohtsu, T., Nakamura, Y., 2005. Protein detection using oligonucleotide probes. *Nucleic Acids Sym. Ser. 49*, 351–352.
- Harada, K., Frankel, A. D., 1995. Identification of two novel arginine binding DNAs. *EMBO J. 14*, 5798–5811.
- Huizenga, D. E., Szostak, J. W., 1995. A DNA aptamer that binds adenosine and ATP. *Biochemistry, 34*, 656–65.